Precision Measurements of d(d,p)t and d(d,n)^{3}He Total Cross Sections at Big-Bang Nucleosynthesis Energies

by

Douglas Sidney Leonard

A dissertation submitted to the faculty of the University of North Carolina at Chapel Hill in partial fulfillment of the requirements for the degree of Doctor of Philosophy in the Department of Physics and Astronomy.

Chapel Hill

2004

Approved:

H. J. Karwowski, Advisor

T. B. Clegg, Reader

E. J. Ludwig, Reader

ABSTRACT

DOUGLAS SIDNEY LEONARD: Precision Measurements of d(d,p)t and d(d,n)^{3}He Total Cross Sections at Big-Bang Nucleosynthesis Energies
(Under the Direction of H. J. Karwowski)

Recent WMAP measurements have determined the baryon density of the Universe Ω_b with a precision of about 4%. With Ω_b as an input, comparisons of Big Bang Nucleosynthesis (BBN) network predictions to primordial abundance observations can be made and used to test BBN models and/or to further constrain abundances of isotopes with weak observational limits. To push the limits and improve constraints on BBN models, uncertainties in key nuclear reaction rates must be minimized. To this end, we used the TUNL Mini-Tandem and High-Voltage Target Chamber to make new precise measurements of the d(d,p)t and d(d,n)^{3}He total cross sections.

In order to use this new data to constrain Standard Big-Bang Nucleosynthesis, the uncertainties in the results, as well as the uncertainty correlations between the data for various energies and the two reactions, must be well understood. A complete fit was performed in energy and angle to both angular distribution and normalization data for both reactions simultaneously. By constructing a realistic fit with parameters for experimental variables such as target thicknesses and solid angles, error correlations between detectors, reactions, and reaction energies were accurately tabulated by computational methods.

Our new measurements significantly improve on the existing data set. The reaction rates calculated from our data are significantly higher than those in the widely used NACRE compilation. These data will thus lead not only to reduced uncertainties, but also to modifications in the BBN abundance predictions.

ACKNOWLEDGMENTS

Thank you to all who supported, inspired, and helped me in this work including all my friends, colleagues, professors, and especially my family. I am grateful to you all and to a blessed life in this great nation of people who supported and funded me in this work. It is the spirit and dreams of these great people, the will to go to the moon and explore the universe simply because we can, because rocks can simply exist, but people explore, it is this spirit which drove me as a child, and which drives the next generation to dream, to work hard, and to succeed in this wonderful land still filled with opportunity, where we have the freedom to take it all for granted while we are reminded so painfully by events like those on September 11, 2001 that indeed we cannot. I humbly dedicate this work to all who perpetuate and protect this spirit, to those who risked and gave their lives fighting overseas for my lifestyle while I wrote this, to the memories of childhood heroes who were lost while we watched from grade-school as the space shuttle Challenger flew for the last time, and to their successors who never returned from the heavens over a year ago on Columbia, may they be remembered for their desire to push the limits. Finally, I especially want to thank my advisor, instructor, colleague, and friend, Hugon Karwowski whose contributions to my success I cannot begin to summarize in this small space. Again, thank you all.

Douglas Sidney Leonard

February 2004

CONTENTS

LIST OF TABLES

LIST OF FIGURES

Chapter 1

Introduction

The Standard Big Bang model does a remarkable job of explaining many features of the Universe which are otherwise difficult to reconcile. Big-Bang Nucleosynthesis (BBN) is well described by a small number of reactions at energies easily obtained in the lab. The outcome of Standard BBN is determined almost entirely by the nuclear reaction rates and the baryon to photon ratio, η, of the universe. With knowledge of key cross sections, one can adjust η to reproduce the current measured values of primordial elemental abundances. In the past, quantitative understanding of BBN has been limited by uncertainties in the primordial abundances and knowledge of η, which until recently, was an essentially free parameter. As observations are improving, the uncertainties of the cross sections themselves are becoming a significant factor in precision tests of BBN predictions.

1.1 The Expanding Universe

Measurements of the cosmic microwave background radiation show that the Universe evolved from a hot dense state. Observations of all parts of the Universe seem to show similar elemental abundances. This is in agreement with the notion that all parts of the Universe evolved from a single homogeneous beginning. Finally, direct measurements of supernovae red-shifts indicate a clear, positive correlation between distance and radial velocity. These are among the most compelling justifications for

the idea that the universe has evolved via expansion from an initially high density, high temperature Big Bang.

1.2 Nucleosynthesis

For this story to be correct, it is expected that light elements were formed after the Universe had expanded and cooled enough for nucleosynthesis to dominate over photo-disintegration. Before a time of about one second the number of neutrons and protons was held in thermal equilibrium by weak interactions. As the Universe expanded and cooled, these processes halted and the ratio of neutrons to protons "froze out". For about the next three minutes only neutron beta decay, with a half life of about eight minutes, changed this ratio by converting neutrons into protons. At a time of about three minutes the universe had expanded and cooled until there were relatively few photons with enough energy to destroy deuterons. At that time the creation of deuterons via the $p + n \rightarrow d + \gamma$ started to take place at a faster rate than the photo-disintegration of deuterons. For the next several minutes nuclear reactions formed light elements. The primary reactions involved are shown in Figure 1.1. The resulting abundances of these elements depended almost entirely on the ratio of the numbers of neutrons to protons, n/p, and the nuclear reaction rates, which depend on temperature. The time between n/p freeze-out and the onset of nucleosynthesis was critical in determining n/p at the onset of BBN. If that time was long, then more neutrons would have decayed and the n/p ratio would have been low. Higher values of the ratio of baryons to photons would have resulted in nucleosynthesis overcoming photo-disintegration sooner and would have produced higher values of the n/p ratio. Thus the key factors in the outcome of primordial nucleosynthesis were the nuclear reaction rates and the baryon to photon ratio η.

With knowledge of these factors it is possible to calculate the primordial elemental/isotopic abundances after nucleosynthesis halted. The lack of stable nuclei with mases 5 and 8 is primarily responsible for limiting nucleosynthesis to producing nuclei

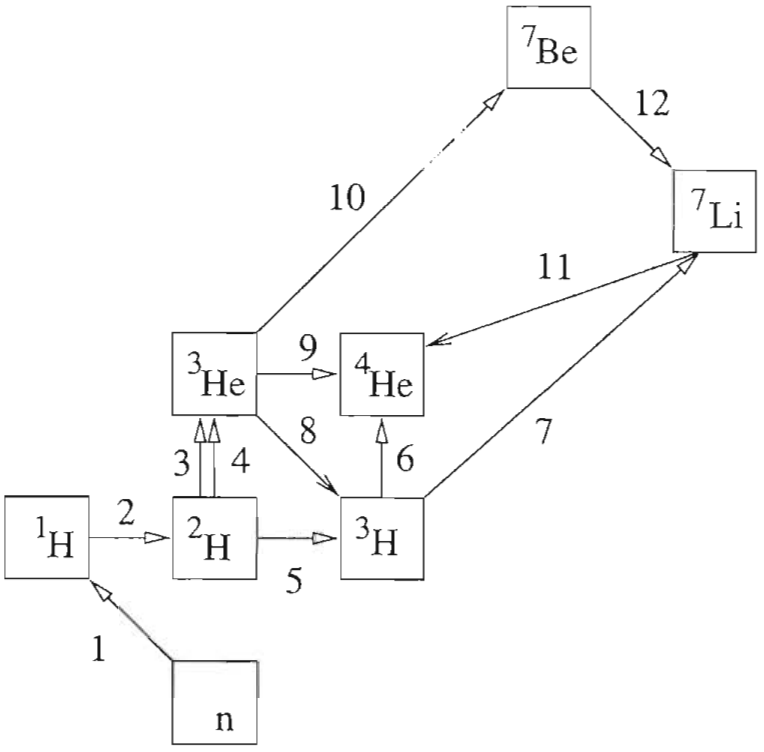

1. $p \longleftrightarrow n$
2. $p(n,\gamma)d$
3. $d(p,\gamma)^3\mathrm{He}$
4. $d(d,n)^3\mathrm{He}$
5. $d(d,p)t$
6. $t(d,n)^4\mathrm{He}$
7. $t(\alpha,\gamma)^7\mathrm{Li}$
8. $^3\mathrm{He}(n,p)t$
9. $^3\mathrm{He}(d,p)^4\mathrm{He}$
10. $^3\mathrm{He}(\alpha,\gamma)^7\mathrm{Be}$
11. $^7\mathrm{Li}(p,\alpha)^4\mathrm{He}$
12. $^7\mathrm{Be}(n,p)^7\mathrm{Li}$

Figure 1.1: Reactions in the Standard-BBN network as depicted by Nollet and Burles [Nol01]. The reactions studied in the present work are listed here as reactions 4 and 5.

of mass 7 and below. In fact one can obtain qualitatively good results by assuming that all neutrons are incorporated into ^{4}He. This gives qualitatively the correct dependence of the ^{4}He mass fraction, Y_p, on η and gives a reasonable approximation of Y_p itself. With detailed network calculations and knowledge of the cross-sections, all of the primordial abundances can be precisely calculated as a function of η. Knowledge of any one abundance or a separate determination of η, thus allows all other primordial abundances to be inferred from the Standard BBN model. Any two of these observables produce a check of the model itself. All of these analyses depend on having accurate and precise knowledge of the nuclear reaction rates.

1.3 Primordial Deuterium Observations

Recent measurements of absorption lines in high red-shift, metal poor, QSO-backlit gas clouds have constrained the primordial deuterium abundances to the impressive interval of $D/H = 2.78^{+.44}_{-.38} \times 10^{-5}$ [Kir03]. The measurement and analysis procedure is well described in the review article of Tytler *et al.* [Tyt00]. Deuterium absorption lines are visible in such clouds with high column densities of D and H. In these clouds, large H contamination is usually present in the D absorption lines. Absorption peaks measured with the HIRES spectrograph on the Keck telescope are fit to the column density, thermal broadening, turbulent velocities and red shift. Ambiguities between H column densities and turbulent velocities arise due to saturation and are distinguished by fitting several spectral lines. The high red-shift and low metalicity of the clouds indicate a high probability that these clouds are indeed unprocessed primordial samples. Currently systematic scatter limits the precision of the deuterium abundance observations [Kir03], but as more data arrive and the systematics become better understood this could quickly change.

Measurements of primordial deuterium abundances [Bur98a, Bur98b] along with recent measurements of η from WMAP data [Cyb03] have threatened to make the nuclear reaction rates the limiting factor in testing the consistency of the Standard BBN model.

1.4 BBN and CMBR

About 200,000 years after the Big Bang, the Universe cooled enough for electrons to "recombine" and form atoms. At that time the universe ceased to be opaque to light. Light emitted at this time of "last scattering" can still be seen today as a mostly-uniform Cosmic Microwave Background Radiation (CMBR). Small fluctuations in this radiation give details about the structure and evolution of the early Universe. In fact recent measurements of CMBR provide independent measures of η [Teg00, Kap01,

Ben03]. Specifically, the recent values derived by Bennet *et al.* from the WMAP data, constrain the baryon to photon ratio to a mere 4% uncertainty [Cyb03].

1.5 Cosmology Enters the Lab

The value of η determined from the WMAP results is in good agreement with primordial deuterium abundance measurements of Kirkman *et al.* However limited amounts of data and the systematic uncertainties in abundance measurements [Kir03] and in reaction rates have limited the level of precision at which the BBN models can be tested to around 10% for most observables.

With the uncertainties of previously existing data, the $d(d,p)t$ and $d(d,n)^3$He reaction cross-sections at energies in the range of a few hundred keV make large contributions to the uncertainties in deuterium abundances as predicted by network calculations of Nollett *et al.* [Nol01, Bur99b, Bur99a, Sch98]. Nollett *et al.* provide sensitivity functions showing contributions to the deuterium and ^{7}Li abundances of several reactions as a function of energy. The significant energy range of both the $d(d,n)^3$He and $d(d,p)t$ reactions extend from roughly E_d = 100 keV up to about E_d = 700 keV. Prior to our measurements, data for these reactions were very limited in this range. Figure 1.2 shows the most commonly used $d(d,n)^3$He reaction data in the relevant energy range. The $d(d,p)t$ reaction data is qualitatively very similar. From $E_d = 325\ keV$ to the top of this energy range, there were very few data and they had large uncertainties. Even at lower energies the uncertainties of previously existing data were around the 10% level or only slightly better. For the energy range above 325 keV, one of the more complete data sets was that of Ganeev *et al.* [Gan58]. Their measurements were performed with three different methods and the sizes of the systematic variations in the results were about 10% of the values. The Ganeev data are not included in the NACRE data compilation [Ang99], probably the most prominent collection of rates for reactions of astrophysical significance.

To improve this situation and tighten BBN constraints we have used the TUNL Low Energy Beam Facility to measure total cross sections for both of these reactions at lab energies ranging from about 112 keV to 646 keV. We have obtained uncertainties of about 2% and our χ^2 analysis techniques have allowed correlations in the uncertainties of the two reactions across the range of energies to be quantified. The new data represent a significant improvement of the inputs to the BBN calculations and facilitate improvements to an emerging high precision BBN era.

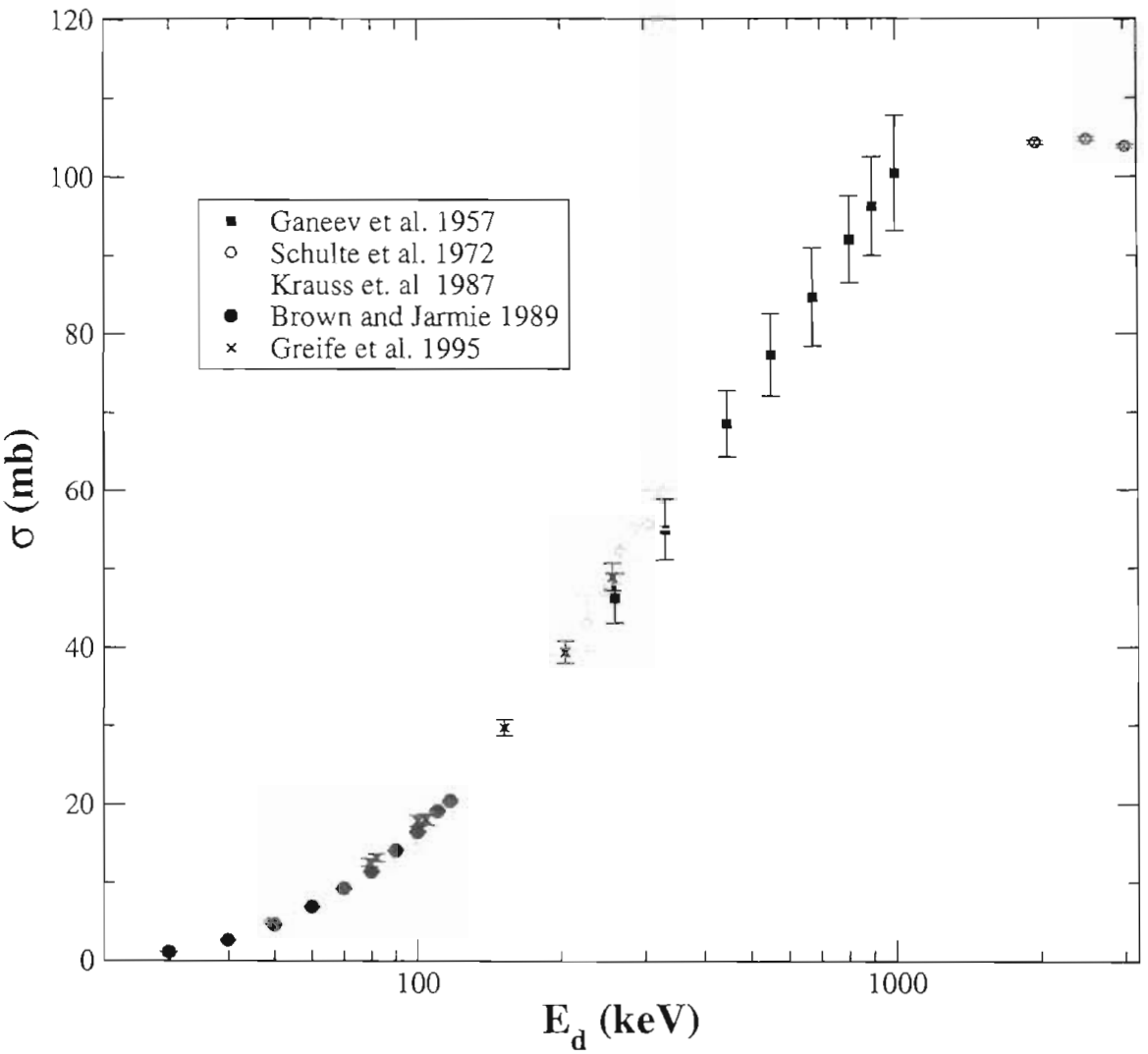

Figure 1.2: Most-commonly used data sets for d(d,n) cross-sections at BBN energies. The d(d,p) data sets are very similar.

Chapter 2

Experiments

To measure the integrated cross sections for the $d(d,p)t$ and $d(d,n)^3$He reactions, we first measured relative angular distributions of the differential cross sections $\frac{d\sigma}{d\Omega}$, henceforth denoted as simply $\sigma(\theta)$, or $\sigma(E,\theta)$, where, as usual, E and θ represent the energy and reaction angle respectively[1]. We then normalized these distributions by measuring absolute differential cross sections at fixed angles. This general procedure was performed for eight energies, E_d= 660 keV, 570 keV, 480 keV, 390 keV, 240 keV, 180 keV, and 120 keV. These are approximate nominal energies and are the values I will use to refer to the various data sets in the text. The determination of the exact energies will be discussed in Section 2.5. Generally data for both reactions were obtained simultaneously. I describe all parts of this process in the sections below. We have perfected many of the details of the techniques throughout many years and many generations of graduate students. Much of this information can be found in previous dissertations and I will reference them when appropriate. Here I will explain the overview of the experimental setup and methods and describe in detail all techniques and details which were peculiar to this experiment.

All data were taken using the TUNL Low-Energy Beam Facility (LEBF) and the High-Voltage Target Chamber [Lud97]. The LEBF is composed of the Atomic Beam

[1]For simplicity, since I am describing experimental measurements performed in an actual lab, all differential cross sections, angles, solid angles, and energies referred to will be in the lab reference frame unless otherwise noted.

Polarized Ion Source [Cle95] and Mini-Tandem accelerator [Bla93]. The combined acceleration potentials of the source, Mini-Tandem and HV chamber provide deuteron and proton beam energies up to approximately E = 680 keV. All targets used were thin, carbon-based, self-supporting transmission targets. Target properties were a crucial factor to consider for all experimental setups.

2.1 The Scattering Chamber

The High-Voltage Chamber which was used for these measurements is described in reference [Lud97]. I will describe the chamber's basic features which are all illustrated in Figure 2.1. A central target rod holds up to five ring-mounted target foils. Two rotating plates are present, one on the top of the chamber and one on the bottom, which can be used to mount detectors on the left and right side of the chamber respectively. A moveable track system allows multiple detectors to be attached to the plates and mounted in the horizontal reaction plane at adjustable combinations of angles and radial distances. Once mounted, the left and right detector sets can be rotated independently using control rods outside of the chamber. Mounting holes for fixed monitor detectors exist on the top and bottom of the chamber's stationary outer perimeter. The fixed monitors can be placed above and below the reaction plane such that their view of the target is not obstructed by the rotating detectors for any arrangement of detectors or any rotation of the detector plates. The beam enters the chamber through an acceleration tube allowing for an acceleration through a 200 kV potential. It then passes through vertical and horizontal entrance slits which define the beam position.

2.2 Cross-Section Normalization

The most difficult part of any cross-section measurement is determining the absolute normalization of the data. Indeed this is the primary area in which our experience

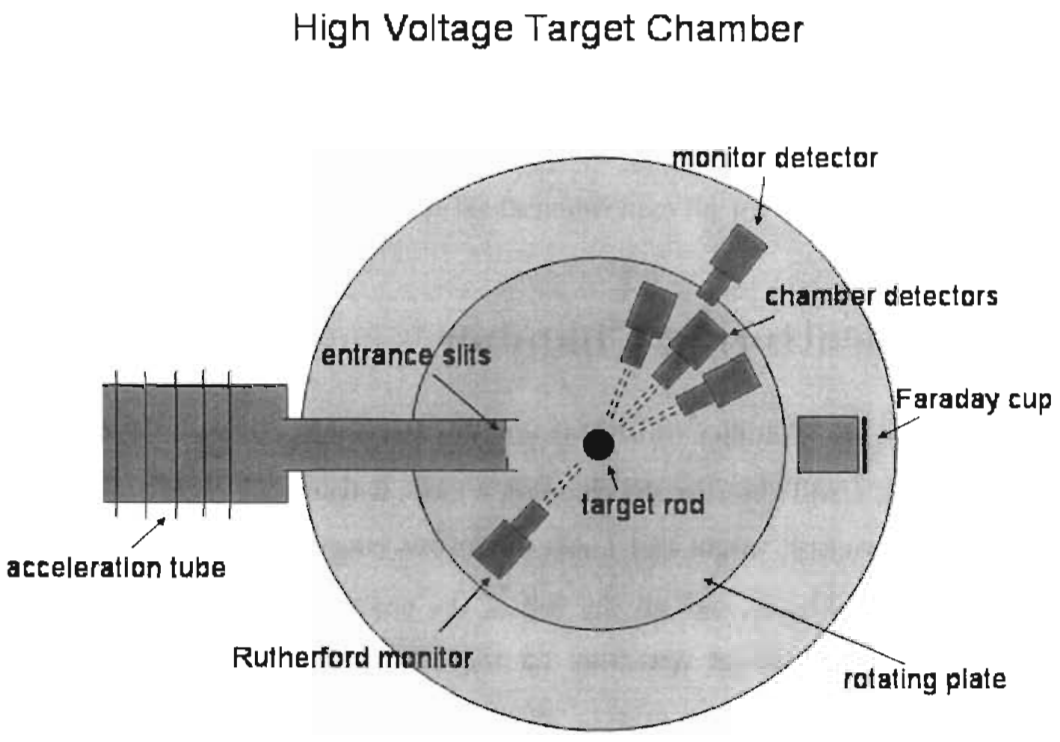

Figure 2.1: The High-Voltage Scattering Chamber: A target rod holds up to 5 self-supporting transmission targets. Left and right reaction detectors are arranged on rotating plates. A back-angle Rutherford-scattering monitor was inserted when needed for relative beam current monitoring. A conventional Faraday cup provides a simpler, less accurate beam current measurement. Out-of-plane detectors monitor target thickness. The entire chamber can be raised to a potential of $\pm$200 kV to accelerate or decelerate the beam.

in few body measurements and techniques has allowed us to improve greatly on previous measurements.

2.2.1 The Problems

When observing a reaction in a detector, there are several factors that contribute to the observed yield. The number of counts N obtained in a detector is in general given by

$$N = nt\Delta\Omega\epsilon\sigma(E,\theta)\,, \tag{2.1}$$

where n is the number of beam particles incident on the target, t is the areal density of target nuclei, $\Delta\Omega$ is the solid-angle of the detector and ϵ is the detector efficiency. For the algebraically challenged, this can be written to give an equation for $\sigma(E,\theta)$,

$$\boxed{\sigma(E,\theta) = \frac{N}{nt\Delta\Omega\epsilon}}\,, \tag{2.2}$$

which is the basic expression we will need to calculate cross sections. Unfortunately, aside from the detector efficiency, nothing else in this equation is easy to determine. Mostly time and work are required to determine the value of N, but the other factors are far more elusive.

For the $d(d,p)t$ and $d(d,n)^3$He reactions, cross sections have in the past been measured using gaseous deuterium targets [Gan58, Gre95, Kra87, Sch72, Bro89], and often by directly measuring all of the above mentioned parameters [Gan58]. Target arrangements include gas cells, gas filled chambers, and differentially pumped chambers. The target thickness can be measured by knowing the gas geometry, temperature, and pressure, but errors can arise especially in arrangements utilizing pressure gradients. The solid angle $\Delta\Omega$ is physically defined in most experiments by some form of metal collimator, or consecutive collimators for viewing extended targets, that select which particle trajectories will reach the detector. In order to keep a well-defined detector angle, such collimators are usually reasonably small with linear dimensions in the range of millimeters. Determining their sizes and their distances to the target with very high precision is difficult. The situation is complicated more when finite geometries are considered. Equation 2.1 assumes the interaction region is point-like. When the interaction region is finite and 3-dimensional, $\Delta\Omega$ is replaced by a G-factor [Sil59]. The G-factor is essentially an integral over all differential volume elements in the viewable target, each multiplied by the solid angles for viewing that element; the result is

normalized to total viewable volume. By viewable I mean any part of the target that is struck by the beam from which scattered particles can reach the detector. This factor depends on the intersection of the beam, the target, and all lines passing through the detector collimator arrangement. The G-factor generally depends on the detector angle. Determining this accurately requires high precision knowledge of the alignment of all equipment involved.

One of the biggest obstacles for a direct cross-section measurement at such low energies as those used in this experiment is measuring the number of beam-particles incident on the target, i.e. the integrated beam flux. This can be done in two ways. The simplest method is to electrically ground the beam stop through a current integrator and time-integrate the current collected from the beam stop. If current integration is used, one must account for charge exchange in the target. As the beam ions exchange charge with the target material, the charge state of some beam particles reaching the beam stop may be different from the charge state produced by the beam transport system, generally prepared as $\pm$e for deuteron beams. This means that the ratio between the charge measured in the beam stop to the number of beam particles incident on the target may be altered by the charge exchange process and thus not well known. The effect can be accounted for if the current can be measured from the target as well as the beam stop. Furthermore, as the beam energy decreases, the energy loss of the beam in the target increases until reaching a maximum at the Bragg peak. For a deuterium beam in a deuterium target, the stopping power is at its maximum when E_d is approximately 550 keV. Energy loss comes from forward Coulomb scattering. As the beam energies approach the Bragg peak, the cross section for forward scattering becomes significant at increasingly larger angles, thus causing beam straggling, a divergence of beam particle trajectories. Straggling can make it difficult to ensure that the beam stop actually collects the entire beam which passed through the target. This effect is clearly demonstrated at even higher energies in the Ph.D. dissertation of Fisher. [Fis03]

When the beam hits a material in the chamber, so-called "secondary" electrons escape from the surfaces of the material. This occurs in both the beam stop as well as in the target. When using current integrators, we have typically implemented a negatively biased suppression collar upstream from the beam stop to prevent these secondary electrons from escaping from the beam stop. We have seen differences in current readings well over 100% for values of suppression voltage ranging from 0 to -200 V for deuteron beams in the energy range of interest. Our experience shows that even if one collects charge from both the beam dump and the target rod, and even if sufficient voltage biases are used to suppress electron scattering, at the beam energies needed for our measurements the electron production effects are so large that significant error will still be present in determining the beam flux.

The problems of electron suppression and charge exchange can be avoided by using a calorimeter instead of a current integrator. A calorimeter measures the thermal energy deposited in the beam stop instead of the charge. The beam straggling problem must still be overcome. Calorimeters are notoriously tricky devices to use. The difficulties of working with calorimeters are described in [Kra87]. However, these very reactions, $d(d,p)t$ and $d(d,n)^3$He, were measured by Brown and Jarmie [Bro89] using such a calorimeter. Their measurement has the smallest quoted errors of any of the $d(d,n)^3$He and $d(d,p)t$ cross-section determinations near the Big-Bang energy range.

Finally, determining the target thickness is a very formidable task. Counting the number of target atoms one at a time is far beyond my expertise in microscopy and surely is too lengthy and menial of a task even for a lowly graduate student, not too mention vastly more difficult than counting ballots in Florida. Furthermore in most solid targets, deuterium atoms tend to be slowly depleted, possibly as a result of sputtering or evaporation when they are struck by ion beams. One would need to stop experiments after about every 10 to 20 minutes of taking data and count all the target atoms again. This is actually one advantage of gas targets. If the temperature and pressure of the gas and the depth of the interaction region are known, then the

areal target site density can be determined. However, beam heating effects as well as previously described geometric concerns still make this difficult.

2.2.2 A Solution

The solution to all of these problems is really quite simple, in principle anyway. All one must do is find a way to calculate the left side of Equation 2.2 using the right side, but without knowing any of the values in the right side other than the yield, N. That is exactly how we proceeded. The basic procedure has already been used by Mike Wood in his work on his UNC Ph.D. dissertation [Woo00] in order to measure cross sections of p-d elastic scattering.

The ideal situation would be to find a reference reaction to compare to the unknown cross section. The ideal reference reaction would be one for which the cross section is already known and one for which all other values in Equation 2.2 can be made identical to the values for the reactions of interest. If this can be done we are left with the following:

$$\frac{\sigma(E,\theta)}{\sigma^R(E,\theta)} = \frac{N}{N^R}, \tag{2.3}$$

where the superscript R represents the reference reaction. The unknown reaction cross sections can be determined by comparing the yields of those reactions to the yields of the reference reaction with a known cross section.

Unfortunately, for all other variables in the two yield equations to cancel exactly, the measurements must be performed simultaneously with the same beam. Otherwise the number of incident particles will not be exactly the same and even the areal target density may change slowly with time. Indeed there is no reaction in the Universe with a sufficiently well known cross section which can be observed with the same beam and target as the $d(d,n)^3$He and $d(d,p)t$ reactions in which we are interested. However, it is clear now that the other variables in the yield equation do not need to be known in

an absolute sense; only their ratios must be known. The most difficult part of the term "absolute normalization" is the word "absolute". By comparing yields, "absolute" is now synonymous with the word "relative", which is a far easier word to handle.

Before continuing it is best to be clear about what still must be measured. If the experimental variables are not the same for the two reactions, then Equation 2.3 generalizes to the following:

$$\frac{\sigma(E,\theta)}{\sigma^R(E,\theta)} = \frac{nt^R\Delta\Omega^R\epsilon^R}{nt\Delta\Omega\epsilon}\frac{N}{N^R}. \tag{2.4}$$

If the same chamber setup can be used, then it should be possible to keep the solid angles the same for the two reactions: $\Delta\Omega = \Delta\Omega^R$. So long as the same target is used for both reactions, the target thicknesses t and t^R can be kept essentially the same as well. I will discuss that in more detail later. The primary remaining difficulty is unfortunately a big one, measuring n, the integrated beam flux. I will return to this issue later in this section.

The technique employed by Wood *et al.* for measuring p-d elastic scattering was to use thin, self-supporting, hydrogenated carbon targets, and to alternate between deuteron beam and proton beam on a single target. The p-p elastic-scattering differential cross sections were all well known from the Nijmegen phase shifts [Ren97], and the above mentioned cancellations applied. The only quantities which needed to be measured were the yields and the integrated beam currents for the different beams. Wood *et al.* measured p-d elastic scattering at a deuteron energy of 2 MeV. At energies this high, electron suppression and beam straggling are not serious problems, so a simple Faraday cup and current integrator were used to collect and measure the integrated charges collected for the two beams[Woo00].

In practice there is one other issue. When beam is incident on the amorphous deuterium targets, deuterium is depleted from them, albeit slowly. As well, their thicknesses may not be perfectly uniform so two beams striking slightly different areas at different times may not interact with the same target thickness. To ameliorate

this problem the beam switching technique was employed several times over short intervals, and small entrance collimators were used to define precisely the incident beam trajectory.

2.2.3 The Procedure

We used essentially the same principle as that used by Wood *et al.* to measure p-d elastic-scattering cross sections, as described above in Section 2.2.2, with the main difference being that we used deuterated instead of hydrogenated targets. In fact the reference reaction we chose was p-d elastic scattering. The Wood measurements of p-d elastic-scattering differential cross sections at $E_{cm} = 667$ keV agree perfectly with theoretical few-body calculations with all parameters fixed from fits to p-p data [Kie95, Woo00]. The agreement is at the 1% level with χ^2 per datum of 1. Other data at lower energies also agree with calculations within the systematic and statistical errors of the experiments [Hut83, Bru01]. This agreement is strong evidence of both the reliability of Wood's and our methods, and of the reliability of the calculations.

Some significant modifications to the procedure were required to overcome complications arising from working with smaller cross sections and at lower energies. At lab energies of a few hundreds of keV, beam current integration becomes difficult for reasons described previously in Section 2.2.1. In order to determine the ratio of proton beam particles to deuteron beam particles, a thin layer of gold, approximately 10 or 20 Å thick (1Å of gold is equivalent to 1.7×10^{15} atoms/cm^2), was evaporated onto one surface of the target. The gold layer was then oriented on the upstream side of the target, facing the incident beam. A back-angle detector was used to monitor Rutherford elastic back-scattering from gold for both proton and deuteron beams. Our low-energy beams are clearly well below the classical Coulomb barriers, and at such back angles there should be no electron screening effects. By taking a ratio of yields for Rutherford scattering with both the proton and deuteron beams and normalizing this ratio to the respective cross sections, a ratio of the number of incident beam particles for the two beams is found,

$$\frac{n^p}{n^d} = \frac{N^p}{N^d}\frac{\sigma_d(E_d,\theta)}{\sigma_p(E_p,\theta)}, \tag{2.5}$$

where $\sigma_p(E_p,\theta)$ and $\sigma_d(E_d,\theta)$ are respectively the differential cross sections for proton and deuteron scattering from gold at the same lab angle, and again the N's are the observed yields. Referring again to Equation 2.4, this relative ratio of integrated beam flux is the only beam-flux information needed to determine the cross sections of interest.

A back-angle gold scattering spectrum is shown in Figure 2.2. As is typical of Rutherford backscattering, it is easy to resolve the gold-scattering peak from the carbon-scattering peak because of the large mass difference between these target nuclei. One can even see what appears to be contamination of something slightly heavier than carbon. It is most likely from $^{16}O(p,p)^{16}O$ elastic scattering attributed to water vapor in the target.

A second complication arises in our case because we are trying to measure reaction cross sections, not elastic-scattering cross sections. Since our reactions have cross sections on the order of mb/sr, as opposed to b/sr for elastic scattering, a much larger integrated beam flux must be used to acquire the data with sufficient statistical significance. Unfortunately, all deuterated solid targets with which we are familiar tend to lose deuterium as more beam is deposited on them. Our experience shows that the amorphous solid targets suffer much less deterioration than other types of targets, but they are not immune to the problem. This is undesirable since a constant or slowly varying target thickness must be maintained between proton and deuteron runs. High intensity beam currents tend also to produce macroscopic defects in targets such as rips and holes, especially at these energies where energy loss in the target is large. These defects often do not render a target useless, but they can cause unpredictable changes in target thicknesses. These effects seem to be more dependent on the beam current levels than on the total number of beam particles incident on the target. It is not just the number of particles which pass through the target that matters, but the

rate at which they pass through. We hypothesize that this is related to heat and/or charge buildup, but the problem is not well understood.

To avoid this problem we first normalized d-d elastic-scattering yields to the p-d yields using small beam currents, below 10 nA. At these currents target depletion was almost imperceptible, no more than 1% per hour, and many targets were structurally stable for several hours. We then took data later with higher beam currents, around 50 to 100 nA, and measured the ratio of d-d elastic-scattering yields to $d(d,p)t$ and to $d(d,n)^3$He reaction yields. Since the elastically scattered deuterons and the reaction products were measured simultaneously in this last step, they had exactly equal target

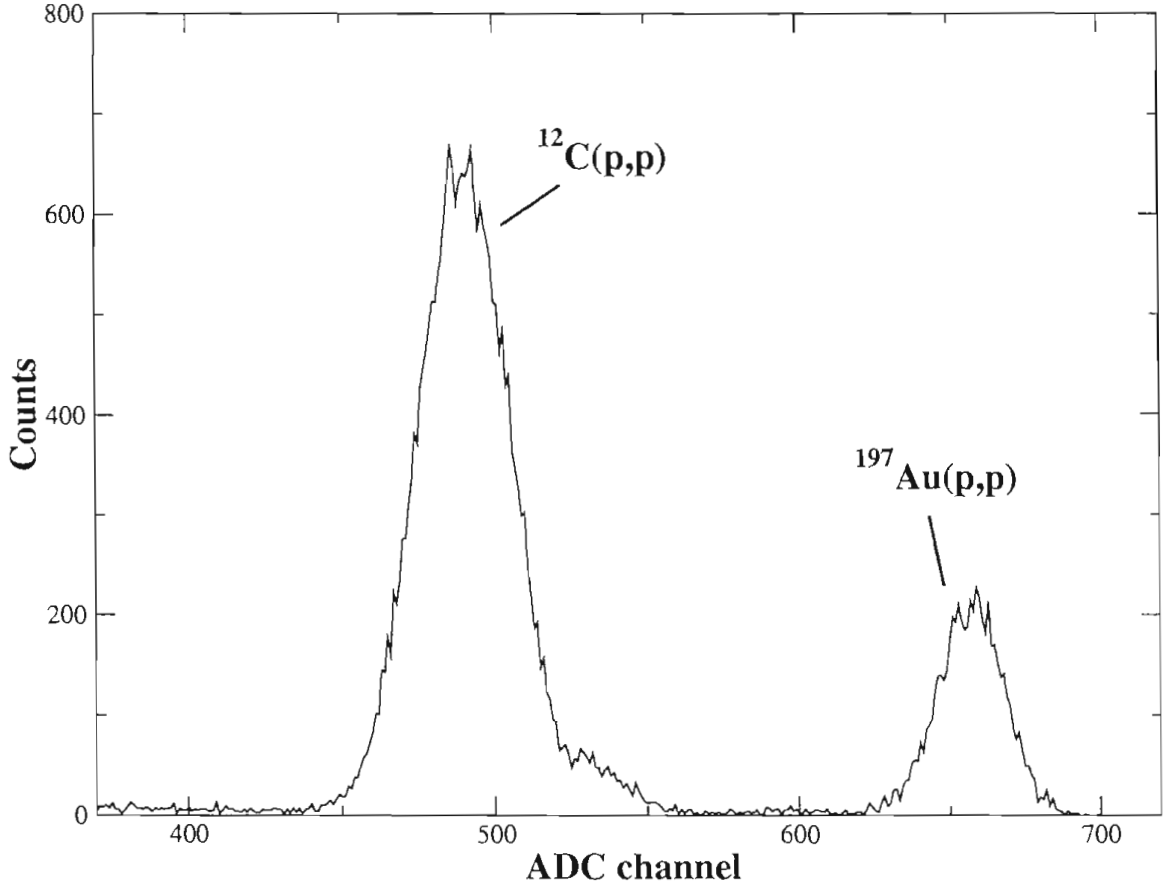

Figure 2.2: Spectrum of Rutherford back-scattering of protons off gold-backed target at $\theta_{lab} = 125°$, E_p =570 keV: The bulge on the high-energy(high channel number) side of the $^{12}C(p,p)$ peak is attributed to proton scattering from ^{16}O contamination in the target.

thicknesses even when target depletion or deformation occurred. For this reason the added step adds negligibly to the overall systematic error of the measurement.

The High-Voltage chamber can only have beams routed into it from one ion source, the Atomic Beam Polarized Ion source or ABPIS [Cle95]. For cross section measurements we did not need to use the polarizing elements of the source so we injected gas directly into the source's ECR ionizer and extracted the beam from there [Cle95]. Since we only had one source, we needed to be able to switch quickly from extracting a proton beam to extracting a deuteron beam. To accomplish this we prepared a small vessel with a mixture of hydrogen and deuterium gas in roughly 1 to 1 proportions by volume. The gas was fed into the ECR ionizer. The ionizer would then produce both deuteron and proton ions simultaneously. Several focusing elements exist in the source which are used to optimize beam extraction. As well, the voltage on the cesium oven determines the charge exchange velocity for producing negative beams which were needed for injection into the Mini-Tandem accelerator. Since all of these settings are optimized in different ways for proton and deuteron beams, it is clearly not possible to optimize them for both at once. However, with the help of John Dunham, our source technician, we were able to produce compromise source parameter settings referred to as "tunes" which supplied more than adequate amounts of both beams and were usually stable. By changing only the inflection-magnet current, we could switch between roughly 10 μA of either beam on the low-energy Faraday cup, the pneumatically actuated beam stop before the Mini-Tandem accelerator. With our compromised dual-beam focusing, the beam transmission through the LEBF was not as efficient as with a normal single-beam source tune. Still, we could easily tune over 100 nA of either beam on target. Such beam currents were higher than what we could use without breaking targets or incurring unacceptably large deadtimes in the data acquisition system.

To minimize effects of possible target non-uniformities, we attempted to tune the beam to strike the same point on the target every time with both beams. The beam entrance collimators which were about 15 cm from the target, allowed very little trans-

verse beam motion, but variations in the angle of the beam through the collimators could lead to very small changes in the location of the intersection of the beam and the target. To minimize this variation, we fixed to constant levels the currents on the last set of beam steerers. We then switched beams by changing the source inflection-magnet current. We optimized the tune for the desired energy using all other beam steering and focusing adjustments, and finally we temporarily perturbed the currents on the last (downstream) steerers to insure that the tune produced was optimally consistent with their fixed settings. Refer to reference [Bla93] for a complete description of the beam transport system. If a higher beam current could be obtained in the chamber by adjusting the final steerers, then the tune was not properly optimized. When this occurred these steerers were reset to their nominal current settings and the tune was re-optimized elsewhere. Once no more beam could be found by perturbing the final steerers, then they were placed back at their nominal currents and the tune was complete.

Rather than logging current settings on steerers and quadrupole magnets, we performed this optimization every time the beam was changed. This procedure allowed our results to sample the possible variations still allowed by this method as opposed to producing a fixed systematic error.

After a long time of passing an ion beam through a single target, a "beam spot" can usually be seen on the target. This is a dark region on the target through which the beam passed. The spot presumably comes from pump-oil vapors which deposit on the target and become cracked by beam-induced heating. The beam spots produced during the beam switching experiments were sharply defined and were the size and shape expected from the square entrance collimators. They were consistent with spots produced from single stationary tunes used for long periods of time. This is consistent with limited variation in the target interaction location.

The beam-tuning procedure generally took about two or three minutes. Beam switching was performed approximately once every 10 to 15 minutes. One complete data collection cycle with both beams would then take roughly 25 to 35 minutes.

About 6 to 10 cycles were performed per energy. Generally, with some repetition on different targets for redundancy or because of broken targets, an elastic-scattering normalization at one energy required approximately 8 hours of data collection and was performed during one overnight shift. Collecting reaction data then required approximately 10 to 12 hours and was completed during the daytime when chaotic discussions about where to find lunch might otherwise interfere with the arduous beam-switching process. Along with time required for changing targets and adjusting electronics for the different run types and energies, one complete and problem-free normalization required about one day of scheduled beam time.

2.2.4 The Setup

For the highest four beam energies, 390, 480, 570, and 660 keV, we used the procedure described in the previous section to normalize the differential cross sections. The amorphous deuterated carbon targets mentioned above were placed on the target rod in the High-Voltage chamber. Seven high-resolution, ion-implanted silicon detectors were positioned in the chamber to observe elastic scattering from deuterium. All detectors had either 300 or 500 μm depletion depths and were fully biased during operation. All had circular 1.50 cm^2 active areas. Four were placed on the rotating detector tracks and set at 35.0° and 48.0° on both the left and right sides. Two more were mounted as out-of-plane monitors at approximately 27.5°. One detector was placed on the top rotating plate at 125.0° left for the purpose of monitoring Rutherford backscattering from gold as explained in Section 2.2.3. The rotating detectors were placed approximately 18 cm from the target with collimators directly in front of them with openings 0.46 cm wide and 0.95 cm tall. The out-of-plane monitor detectors were mounted at their fixed distances of approximately 30 cm from the target and the back-angle monitor was placed at about a 10 cm radius. The out-of-plane monitors were given collimators 0.64 cm wide by 0.95 cm tall, and the back-angle monitors were equipped with circular collimators of 1.27 cm diameter. Cylindrical aluminum "snouts" or tubes were placed in front of all detector collimators to help reduce possible

background scattering from various sources such as the entrance slits. These snouts each had a 1.27 cm inner diameter and were typically 3.81 cm long. Small permanent magnets were placed around the snouts to reduce the effects of electrons released from the target. Precise measures of collimator sizes and radii were not necessary since all solid-angle values cancel out using the beam-switching normalization procedure. An aluminum plate serving as a Faraday cup, was placed at the back of the chamber to stop the beam. The plate was isolated from the chamber and connected to a beam current integrator.

The two pairs of detectors on the rotating plates were used to observe p-d elastic-scattering yields during proton beam runs. Spectra are shown in Figure 2.3. A small

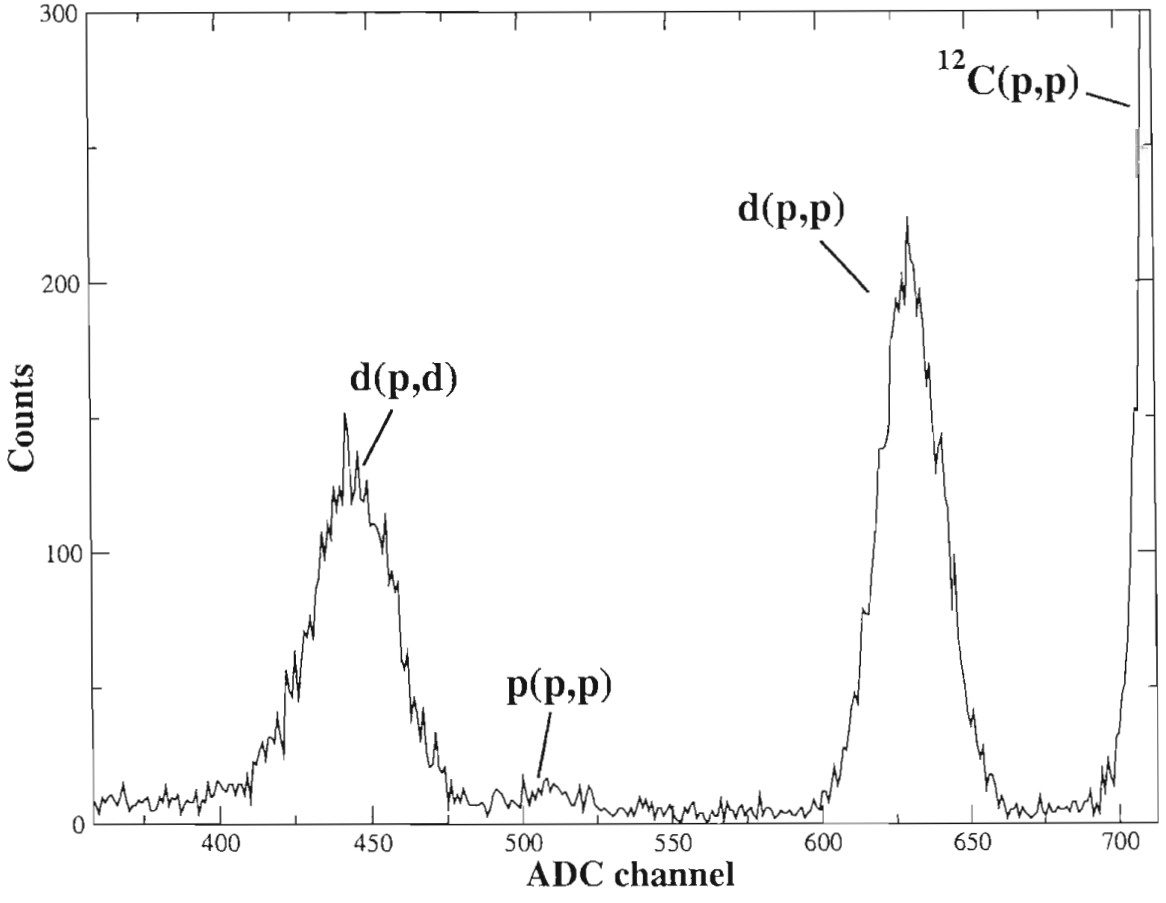

Figure 2.3: Spectrum of proton elastic scattering on a deuterated target at $\theta_{lab} = 27°$, E_p =570 keV

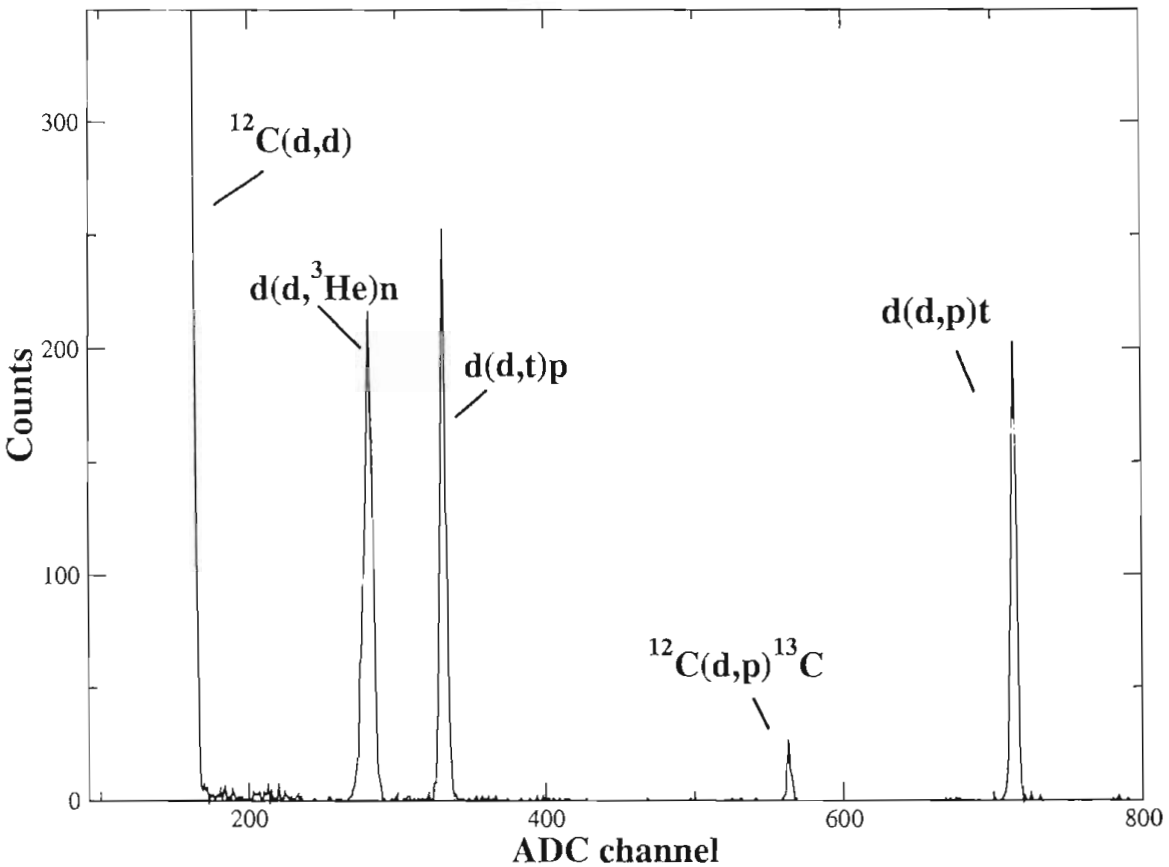

Figure 2.4: Spectrum of d+d reaction products at $\theta_{lab} = 35°$, $E_d = 480$ keV.

extra peak is visible from $p(p,p)$ due to hydrogen contamination in the target. The out-of-plane monitors were then used to measure d-d elastic-scattering yields during the interleaved deuteron runs and during reaction runs. The in-plane detectors were again used for observing reactions during the reaction runs; see Figure 2.4. The reason for using two detector sets stems from the need to measure d-d elastic scattering simultaneously with the reaction products as explained in Section 2.2.3. It is impractical to do this in the same detector because of the large energy discrepancy between the peaks. In order to see the reaction peaks, the gains on the amplifiers needed to be so low that the low-energy elastic-scattering peaks were not resolvable. Using different detectors for monitoring elastic scattering and reactions solved this problem and provided more flexibility for the choice of angles for the different measurements. The final

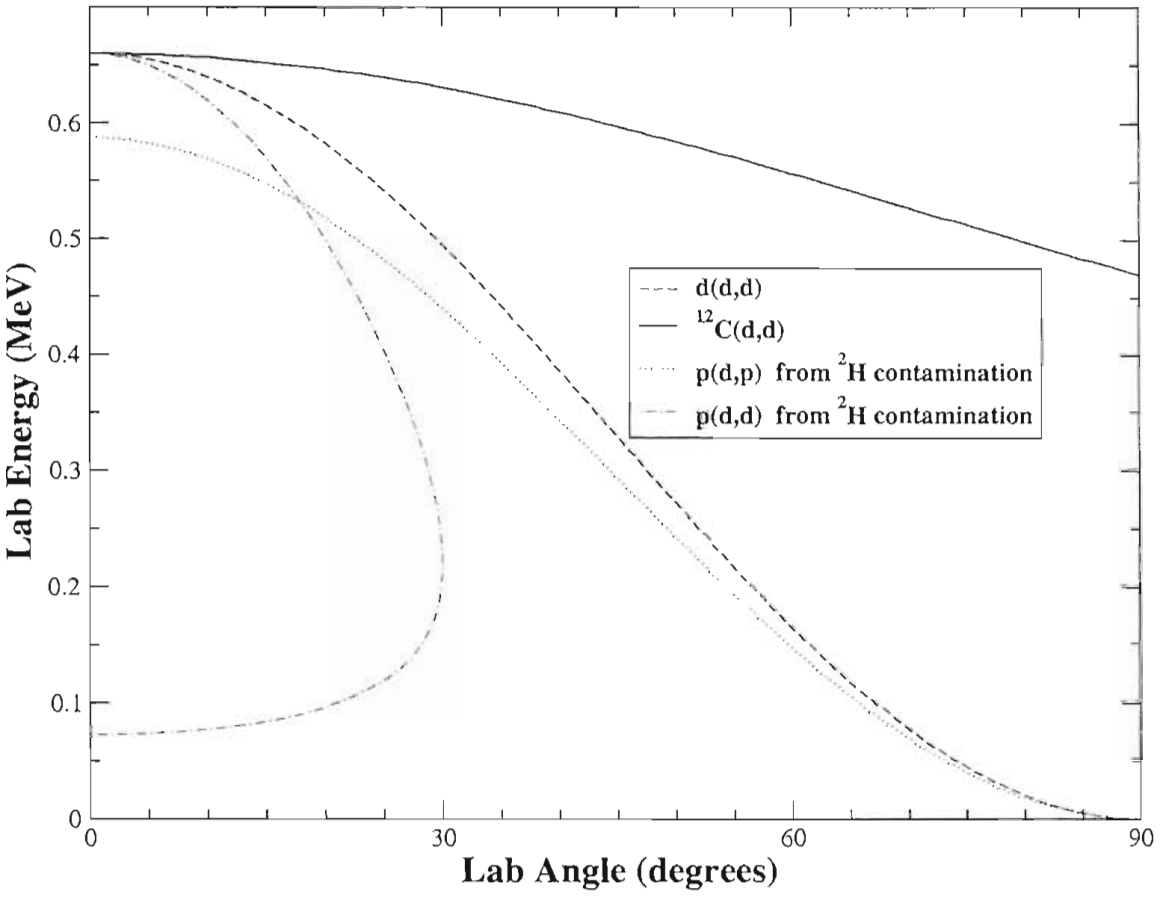

Figure 2.5: Kinematics for deuteron elastic scattering at $E_d = 660$ keV

reaction measurements had to be performed in the same detectors as for the proton elastic-scattering measurements so that they would have the same solid angle as the runs where the cross sections were known. Furthermore, the d-d elastic yields had to be measured in the same detectors for both the beam switching runs and the reaction runs, again so that the solid angle would not enter into the result. For these reasons a separate detector set was dedicated to monitoring d-d elastic-scattering yields.

Measurements of the d-d scattering yields were complicated by the presence of hydrogen contamination in the targets which mandated that the monitor detector angle be carefully chosen. The hydrogen in the targets is likely to come from moisture absorbed by them before they are placed in the chamber. The kinematics for a 660 keV deuteron beam scattering from carbon, deuterium, and hydrogen are shown

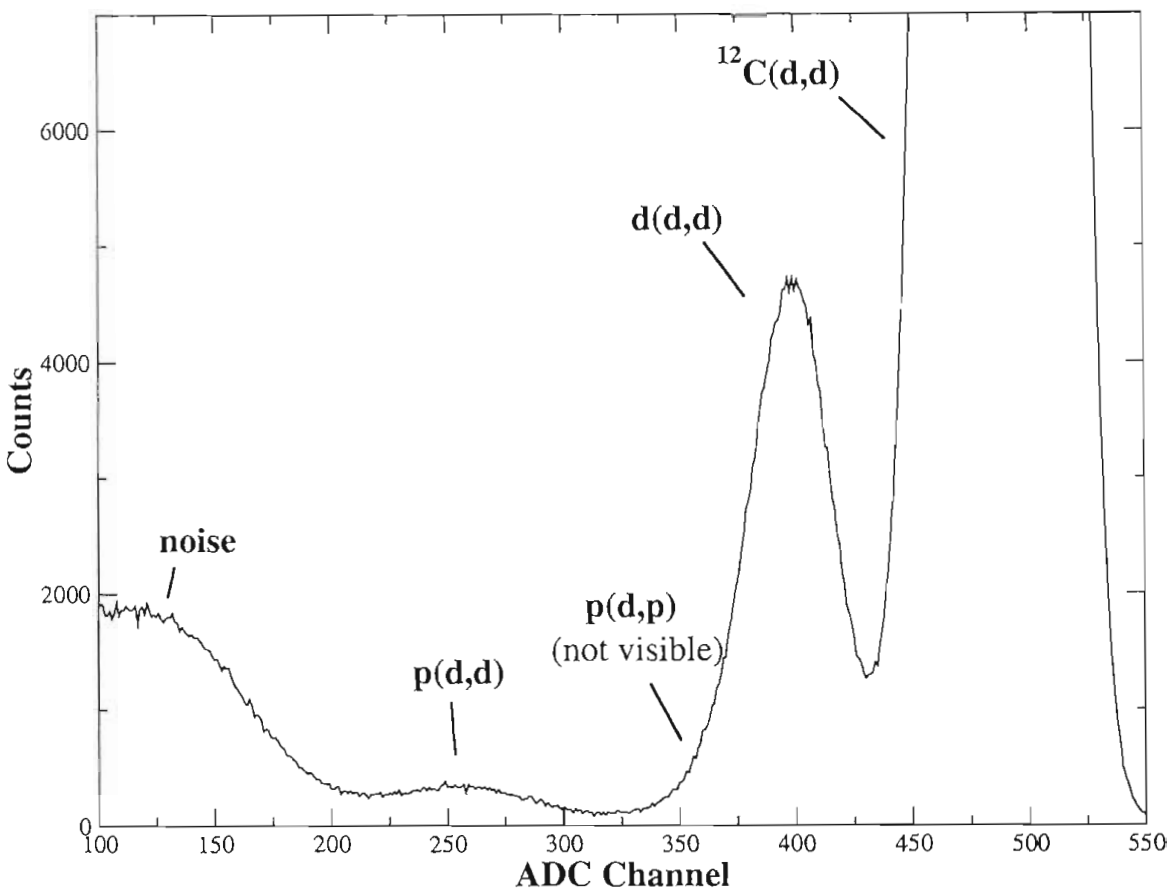

Figure 2.6: Monitor-detector spectrum for deuteron elastic scattering on deuterated target; $E_d = 390$ keV, $\theta = 27.5°$: The $p(d,d)$ scattering peak is clearly visible and can be used to determine the area of the $p(d,p)$ peak hidden under the $d(d,d)$ peak.

in Figure 2.5. The d-d scattered-particle energy is sandwiched between the scattered-particle energies for $^{12}C(d,d)$ and $p(d,p)$ scattering. From the kinematics plot alone it may appear that $p(d,p)$ is the bigger concern. However, due to its large yield, the $^{12}C(d,d)$ elastic-scattering peak can significantly encroach on the $d(p,p)$ peak for energy separations much larger than those needed to separate the $p(d,p)$ peak.

At the lowest energy where the beam-switching normalization was performed, 390 keV, it was not possible separate $d(d,d)$ scattering products from both $^{12}C(d,d)$ and $p(d,p)$ scattering products. Instead the $p(d,d)$ scattering peak was used to determine the yield in the $p(d,p)$ peak. The yield for $p(d,p)$ scattering could then be subtracted from the $d(d,d)$ scattering yield. It is important to note that we were

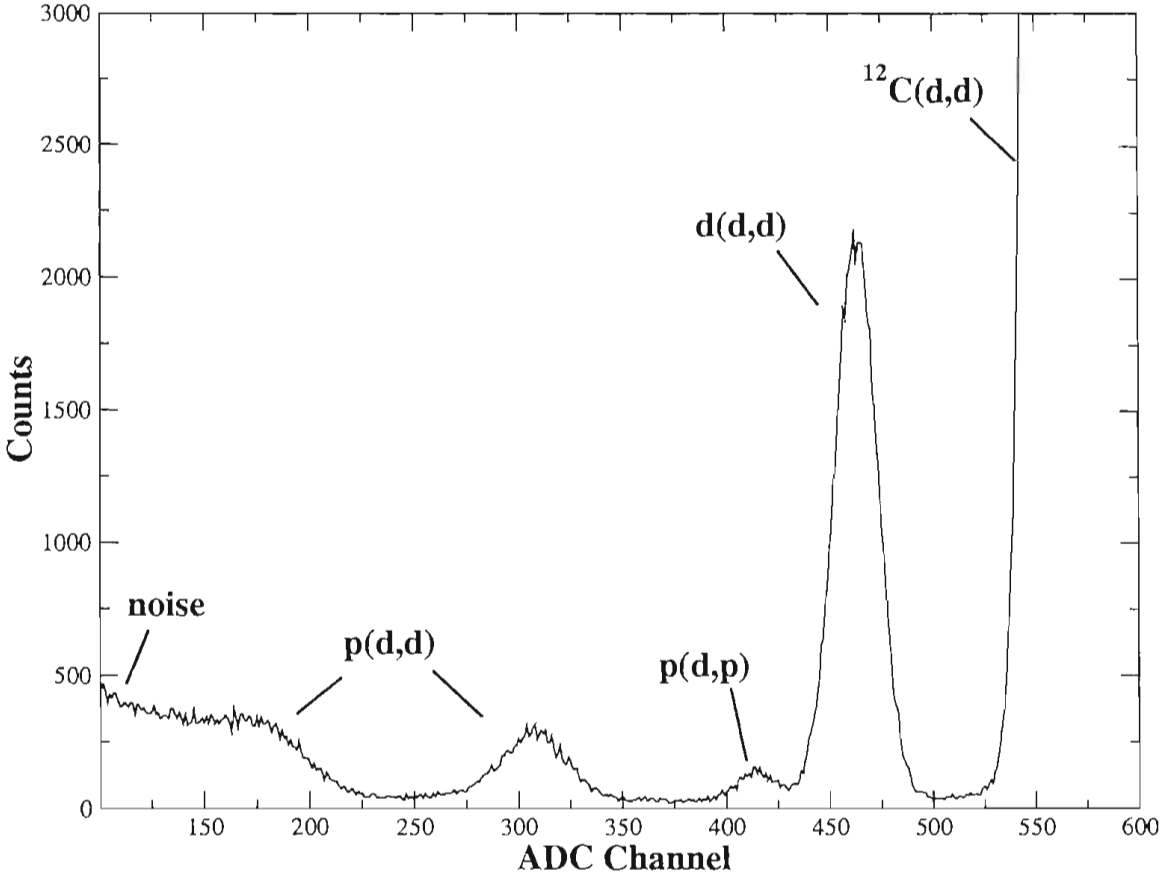

Figure 2.7: Monitor-detector spectrum for deuteron elastic scattering on deuterated target; $E_d = 660$ keV, $\theta = 27.5°$: All three peaks for scattering from hydrogen contamination are visible. At this energy the $d(d,d)$ peak is easily separable.

not trying to measure $d(d,d)$ scattering cross sections with high precision. We only needed a high precision, consistent, relative measure of the deuterium target thickness to relate the beam switching runs to the reaction normalization runs. If the ratio of hydrogen to deuterium were constant in every target, the $p(d,p)$ peak would introduce no error since it would still provide a consistent, proportional measure of the amount of deuterium in the target. Typically the $p(d,p)$ yield was less than 10% of the $d(d,d)$ yield. The ratio of the two varied by about 30% from target to target. This contamination should produce about a 3% error if no effort is made to correct for it. Thus only a rough correction was needed to reduce this to a negligible amount.

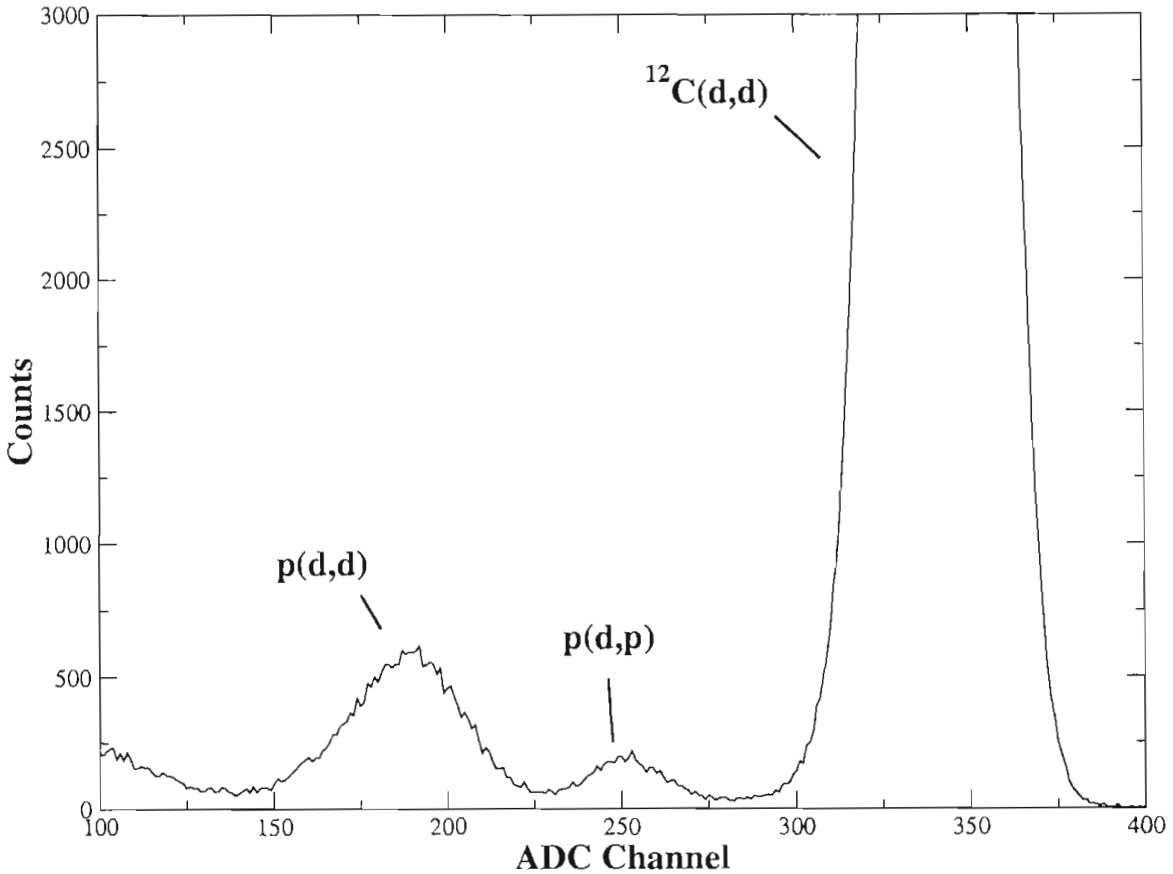

Figure 2.8: Monitor-detector spectrum for deuteron scattering on hydrogenated target; $E_d = 390$ keV, $\theta = 27.5°$

The $p(d,d)$ scattering is kinematically disallowed beyond 30° in the lab frame. Choosing angles much forward of 30° caused the $^{12}C(d,d)$ and $d(d,d)$ elastic-scattering peaks to be unresolvable at the lowest energies. The angle of 27.5° (only increments of 2.5° were available in the chamber for placement of the monitors) was experimentally determined to produce the best compromise, allowing $p(d,d)$ elastic scattering to be detected while maintaining some separation of d-d elastic scattering from carbon elastic scattering. At higher energies this angle allowed all three peaks to be cleanly separated by peak fitting alone. Spectra are shown for both 390 keV and 660 keV in Figures 2.6 and 2.7 respectively.

In order to use the $p(d,d)$ scattering peak to constrain the $p(d,p)$ scattering yield, monitor spectra were collected at several energies for deuteron scattering from a hy-

drogenated carbon target. These spectra allowed the ratio of the $p(d,d)$ yield to $p(d,p)$ yield to be directly measured. A spectrum taken at 390 keV deuteron energy is shown in Figure 2.8.

2.2.5 Bootstrap Mania: Low-energy normalizations

It was not possible to normalize the lowest energies, 120, 180, 240, and 320 keV using the method described in Sections 2.2.3 and 2.2.4. At these low energies the spectra of elastic peaks were too compressed compared to the peak resolutions and it was not possible to resolve all needed elastic peaks with sufficient precision. We instead normalized reactions at these energies directly to reactions at 480 keV using the differential cross sections already obtained for 480 keV from the previous method. This energy is the highest energy, and thus has the best spectral quality, obtainable without using a potential on the High-Voltage Chamber. In fact, at 480 keV the spectral quality is very good and there was nothing to be gained, other than headaches, by using higher energies.

To normalize these data at low energies, the chamber was set up with 8 detectors at forward angles on the rotating plates. Four detectors on each side were placed on the tracks at 60°, 44°, 28°, and 13°. As before, one back-angle detector was placed on the top rotating plate to monitor backscattering from an upstream gold target layer. This detector was placed at 164°. All detectors were placed approximately 11 cm from the target. All were collimated with 1.27 cm diameter circular collimators.

At these low bombarding energies, amorphous deuterated carbon targets usually become very fragile. In order to prevent targets from breaking, we used deuterated parapolyphenol (D.P.P.) targets [Iri] for these measurements. We constructed the targets by evaporating an approximately 5 μg/cm^2-thick layer of D.P.P. onto a 5 μg/cm^2 carbon foil. The D.P.P. layer was approximately thick as well. As in the high-energy normalizations, a roughly 15-Å-thick gold layer was evaporated onto the D.P.P. surface. Again the gold layer was faced upstream so that the beam first passed through the gold, then the D.P.P. and then the remaining carbon backing.

The actual normalization procedure was fairly straightforward. We tuned deuterium beam on target at 480 keV and observed ratios of reaction yields to gold backscattering yields. We then re-tuned to the energy of interest using the same target. The procedure was repeated several times. Taking the ratio of the two results and dividing out the two Rutherford cross sections provided the ratios of differential cross sections at 480 keV to the cross sections at each of the lower energies.

2.3 Angular Distributions

The normalization procedures described above are indeed collectively the most difficult part of our cross sections measurements. Alone however, they only determine the differential cross section at a few fixed angles. To measure the total cross sections, or more correctly, the integrated cross sections, one must, as the name implies, integrate the differential cross sections over all angles. To calculate this integral the differential cross section must in principle be known for all angles. Once we knew the differential cross section at a few points, all that was needed was to measure the relative angular distribution of cross sections at other angles. In other words, we need to know the ratio of differential cross sections between any two angles, but we did not need to measure the absolute values at any more angles.

To this end we set up the chamber again with four fixed, out-of-plane, monitor detectors. Six detectors were placed on the rotating tracks, three on each side, with 13° separation between each detector. Two pairs of out-of-plane monitor detectors were placed at approximately 10° and 40°. Detectors were approximately the same distances from the target as in the setup for the high-energy normalization measurement. All detectors used circular collimators approximately 1.27 cm in diameter. Beam currents of 50 to 100 nA were used. Amorphous carbon targets were used at the highest energies for their high deuterium content. At lower energies carbon backed D.P.P. targets were used for their superior durability.

By taking data with the rotating plates in several positions, many angles could be normalized to the fixed monitor detectors, thus dividing out all beam current and target thickness information and leaving only a relative angular distribution of $\sigma(\theta)$.

All six rotating detectors could have had slightly different solid angles arising from small differences in machining. In order to relate the angular distribution from the different detectors, it was necessary to know the ratios of the solid angles of the various detectors. To measure these ratios, we placed onto the target rod an ion-implanted ^{3}He target constructed by Dr. Geist [Gei98]. Each detector pair was then placed at 35° for one data collection run each to observe protons from the $^3\mathrm{He}(d,p)^4\mathrm{He}$ reaction. By comparing the ratio of detector yields to monitor yields for every detector for the same reaction and angle, the ratio of solid angles could be determined. The $^3\mathrm{He}(d,p)^4\mathrm{He}$ reaction was used for its high cross section and slow angular dependence.

The largest challenges in the angular distribution measurements came from the presence of carbon in the target. The elastic-scattering rate from carbon was much higher than the reaction rates. Generally, with the high Q-values of the reactions, 4.032 MeV and 3.269 MeV for $d(d,p)t$ and $d(d,n)^3\mathrm{He}$ respectively, it was possible to separate the reaction peaks from the lower-energy elastic-scattering peaks. However, at forward angles the energy of the scattered deuteron from $^{12}\mathrm{C}(d,d)$ approaches the beam energy. The cross section for elastic scattering also rises very rapidly at forward angles as it becomes dominated by the Rutherford cross section. To prevent the elastic-scattering rate from overloading the data acquisition system, we placed thin Mylar stopping foils in front of the detectors. Ring mounted foils were constructed in various thicknesses and could be easily inserted and removed from the detector holders as experimental conditions required. Depending on the beam energy and reaction angle, various thicknesses were used ranging from 1 μm at the lowest energies to 6 μm at the highest energy. The thicknesses were chosen to be slightly greater than the range of elastically scattered deuterons.

Figure 2.9 shows the kinematics for outgoing particles for all relevant reactions on a deuterated carbon target for an incident beam energy of 660 keV. At forward

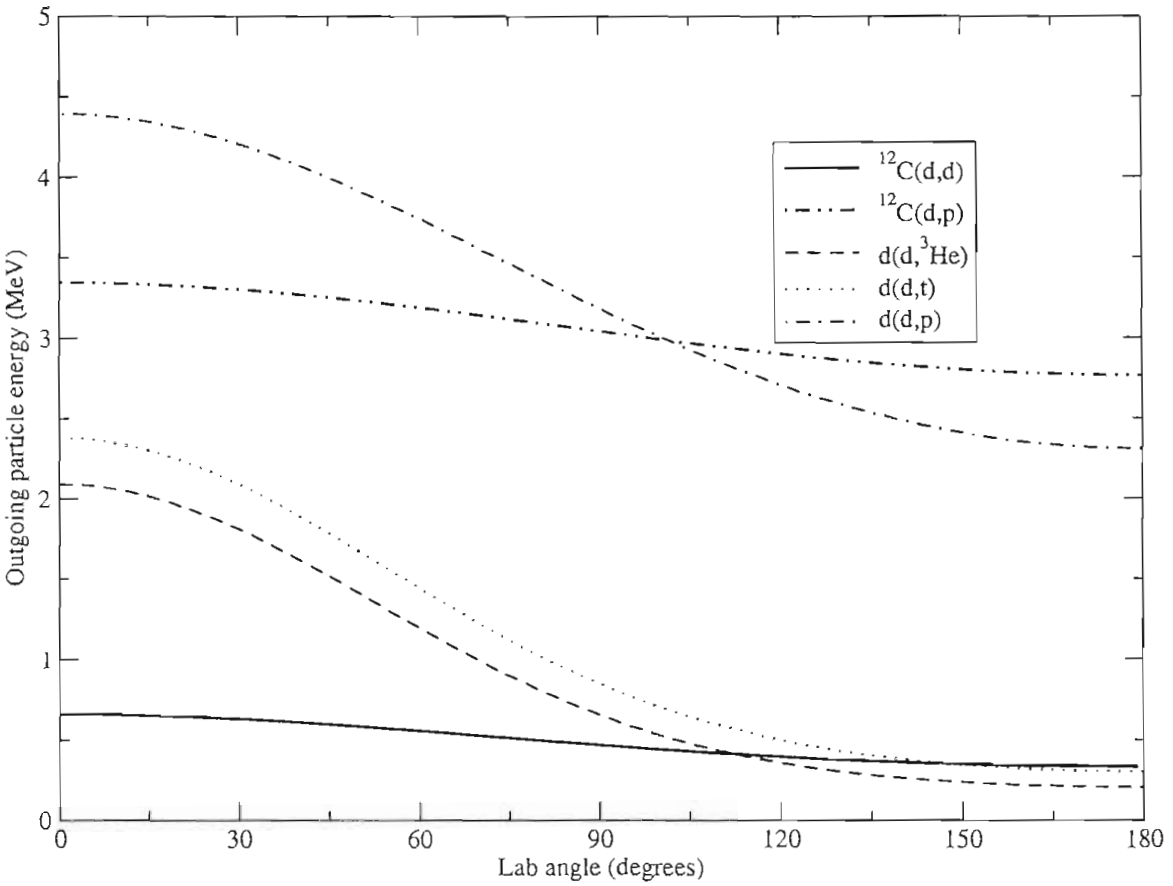

Figure 2.9: Kinematics for reactions from a deuteron beam on a deuterated carbon target at $E_d = 660$ keV.

angles the energy of the ^{3}He ions is significantly higher than the elastic-scattering energy and a foil thickness can be chosen to stop the $^{12}C(d,d)$ elastics and not stop the ^{3}He ions. It is not as easy as it seems though because the stopping power for ^{3}He ions is larger than for deuterons. As seen in Figure 2.9, when the detection angle increases, the reaction energies drop off much faster than the energy of elastically scattered deuterons, and eventually the two can be resolved. Due to limitation on energy resolutions and the differences in stopping powers, the data for our highest energy ^{3}He distribution were sparse. At lower beam energies, the $^{12}C(d,d)$ energy drops off proportionally to the beam energy. The reactions all have positive Q values and thus drop off more slowly. Hence the separation improves quickly as seen in

Figure 2.10, and at our lowest energies we were able to obtain data for all reaction peaks at all back angles without the use of foils. All monitor detectors had 6 μm-thick mylar foils in front of them for all energies. These stopped ^{3}He ions from entering the monitors, but since the monitors only measure relative beam current and target thickness it was not necessary to have all peaks in their spectra. A monitor spectrum from an angular distribution at $E_d = 480$ keV is shown in Figure 2.11.

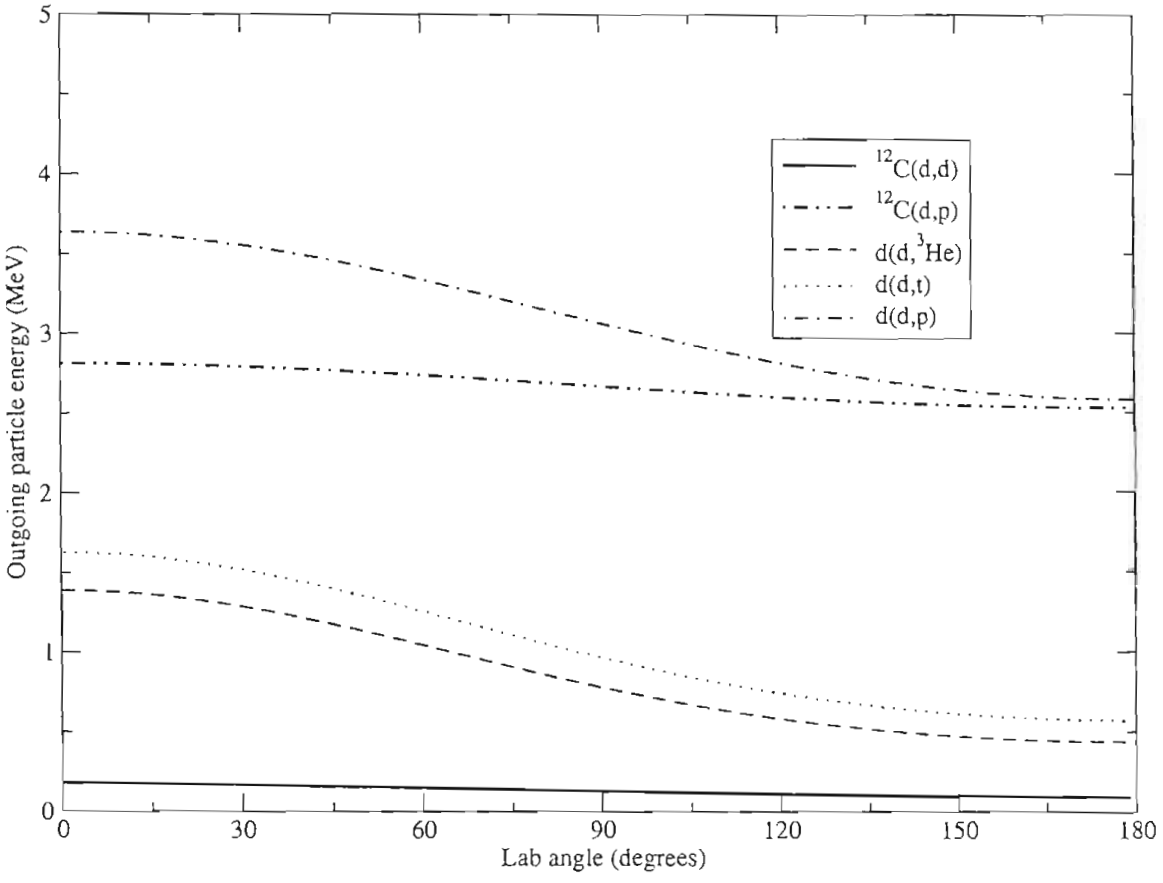

Figure 2.10: Kinematics for reactions from a deuteron beam on a deuterated carbon target at $E_d = 180$ keV. At this beam energy the $^{12}C(d,d)$ scattering energy is below the reaction energies at all angles.

The presence of carbon in the target produced one other minor issue. Again referring to Figure 2.9; the reaction energies of $^{12}C(d,p)$ and $d(d,p)t$ products cross. This produces a small range of angles where $d(d,p)t$ data cannot be taken. However,

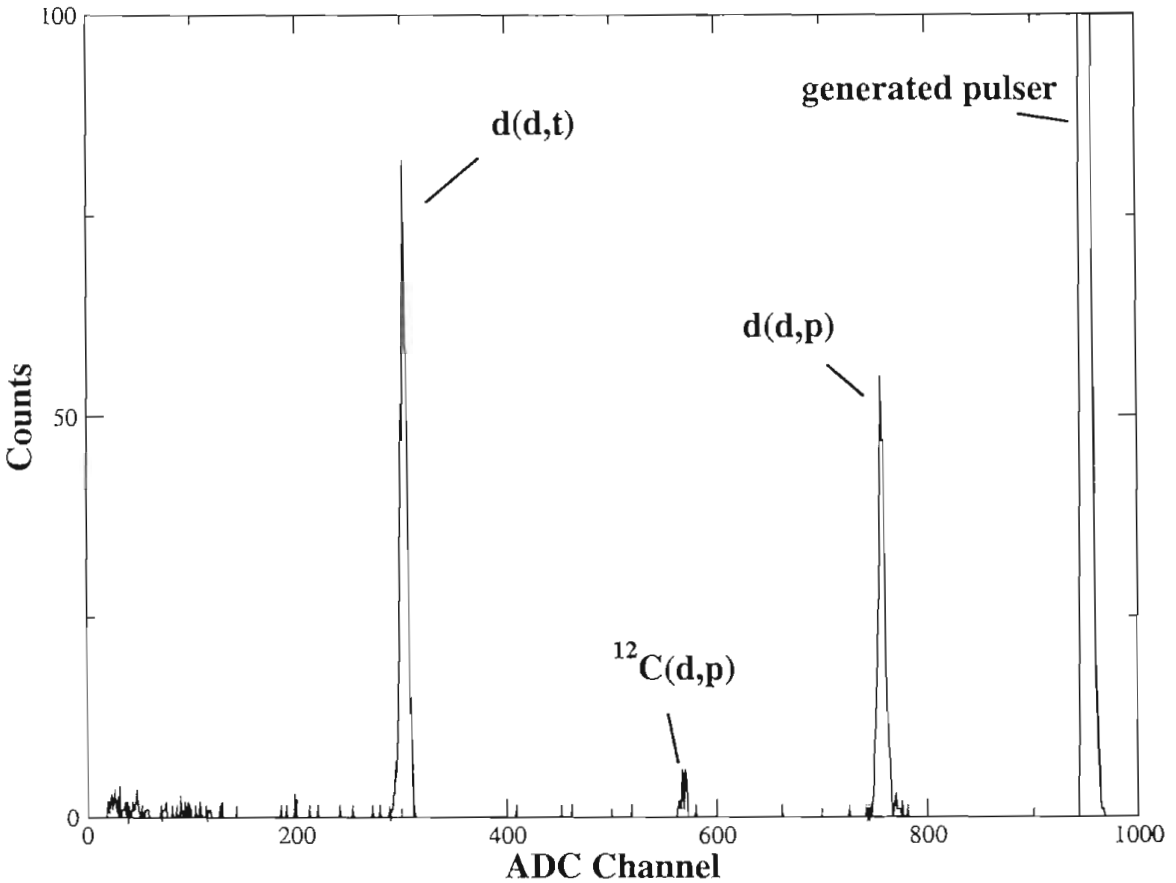

Figure 2.11: Reaction monitor spectrum from angular distribution at $E_d = 480$ keV, $\theta_{lab} = 40°$: 6 μm-thick mylar foils stopped elastic-scattering products and ^{3}He ions.

because of the high resolution of the reaction peaks, I spent more time worrying about not confusing the two peaks than worrying about the loss of data in a very small angular range. In fact, as stated before, we have generated normalized angular distribution data for the $^{12}C(d,p)$ reaction at many energies and angles. It can be analyzed should there ever be a compelling reason.

Angles near 90° in the lab posed difficulties for other reasons. Since the target is a 2-dimensional-like film supported on a ring, when the target is oriented perpendicular to the beam, reaction products near 90° are blocked by the target rod. To measure angles near 90° we rotated the rod approximately 35° to 40° to either side such that the beam still could pass through while allowing detectors to be placed at 90°. This

configuration often caused one or two of the four monitor detectors to be blocked by the target rod. We attempted to maintain at least one useable pair of symmetric monitors at all times and to keep rotating detectors at symmetric angles. Doing this allowed solid angles and cross-section changes caused by small deviations in beam position to cancel to first order in the sum of counts in the symmetric detectors. Detecting particles with detector angles near parallel to the target surface, whether the target was rotated or not, also caused increased energy loss for the outgoing ^{3}He ions, often making it more difficult to separate them from the elastically scattered deuterons and the electronic noise.

In spite of all of these difficulties, we were able to obtain very clean spectra at many angles for the entire desired range of energies. In fact I mislead the reader slightly by claiming $\sigma(\theta)$ must be known at all angles in order to find the integrated cross section. In our particular case the beam and target particles were identical. In the center of mass frame there is no way to tell the difference between 0° and 180° using information from the identical incoming particles, so it is impossible for the physics to distinguish the two. It then must be true that the proton has equal probability of going either forwards or backwards. This implies that in the center-of-mass frame the differential cross section is exactly symmetric around 90°. Thus if we have data for one side of 90°, it is not necessary to have data on the other side. Such symmetric data then serves as a check of systematics and chamber alignment or as supplementary statistics. To further improve the situation, both the proton and the triton were detected from the $d(d,p)t$ reaction. The triton corresponds to a back angle proton, but because of the mass difference, the center off mass conversion is not the same for the two and we detect two different center of mass angles at once. This is only true for the $d(d,p)t$ reaction since neutrons from the $d(d,n)^3$He reaction are not detected.

2.4 Detector Electronics

As described in ref. [Lud97], the High-Voltage Chamber can accommodate many silicon surface-barrier detectors in various moveable configurations. Such detectors were used for all parts of these measurements. All detectors used were high-resolution ion-implanted detectors made by ORTEC or Canberra. The basic electronic setup used is shown in Figure 2.12. A pulser signal is inserted into the preamp and is thus passed through all of the same electronics as the detector signal. The pulsers are then visible in the spectra. The pulsers are also sent directly to a Kinetic Systems NS-621 fast scaler counter. The number of counts registered in the pulser scaler is compared to the number of counts in the pulser peak in the spectrum. The ratio of the two gives the deadtime in the data acquisition system, a measure of the fraction of time when each ADC is busy and unable to accept new signals. We were limited to six Northern NS-621 ADC's so multiple detectors were often routed into one ADC. When this was done detectors with similar count rates were placed in the same ADC to insure that they would have similar deadtimes. These were usually left/right symmetric pairs. To avoid two pulsers reaching the ADC simultaneously, a pulser signal was only sent to one of the two preamps.

While on the subject of simultaneous pulses, reactions and scattering can and do produce coincident signals in left/right detector pairs for certain reactions and angle combinations. It cannot be stated in too many places that one should be very careful to avoid such coincidences between detectors routed into the same ADC. When these coincidences occur, either one signal will be lost entirely while the ADC is busy digitizing the other, or the amplitudes of the two signals will be summed, digitized, and then stored in only one of the two corresponding spectra. Usually the center of mass angles for the two particles will not be complimentary over the entire solid angle of the detectors, so not all particles in a particular peak will have this problem. This only means that an unobservant experimenter is likely not to notice the problem until some months later, or worse the effect will be small enough only to cause error and

not to be noticed at all. One should always check the kinematics twice for problematic coincidences.

In particular, for this experiment, protons and tritons from the $d(d,p)t$ reaction were coincident at an angle which varied with energy. Care was taken simply to avoid this angle for detector pairs sharing an ADC. We also used separate ADC's for all elastic-scattering monitor detectors in order to avoid any possible coincidence problems in those detectors.

For many parts of the experiment, the chamber was electrically isolated from ground and brought to a high negative potential of as much as 200 kV. This required that all detector signals be sent from the chamber via fiber-optic connections as described in [Lud97]. Because of the number of detectors needed for these experiments and in order to improve signal resolutions, a new fiber optic link was developed [Mck01]. These transmitters and receivers feature an input and output voltage range respectively of +/- 12 V and an improved signal-to-noise ratio compared with the previous design which allowed only 0 to 3V dynamic range. The noise levels of the fiber-optic links were completely negligible compared to other sources of noise from the detectors and electronics. The design was optimized for fast A.C. signals thus producing minimal D.C. offset with high event rates. The High-Voltage Chamber has a limited amount of space available for electronics under the dome. With this in mind the fiber-optic transmitters were mounted in two-slot-wide NIM modules with 8 transmitters in each module.

Since the fiber links are more stable with AC signals, we sent the bipolar output of the amplifiers to the fiber transmitters. A timing single-channel analyzer (TSCA) was connected to the output of the receiver and triggered a gate on the signal pulses. The gate was triggered on the zero crossing of the bipolar signal. In order to digitize the positive signal, the receiver output was split and delayed so that the positive pulse would arrive after the gate was triggered. Both the gate and the delayed signal were then sent into an ORTEC 542 Linear Gate and Stretcher. The gate signal was also

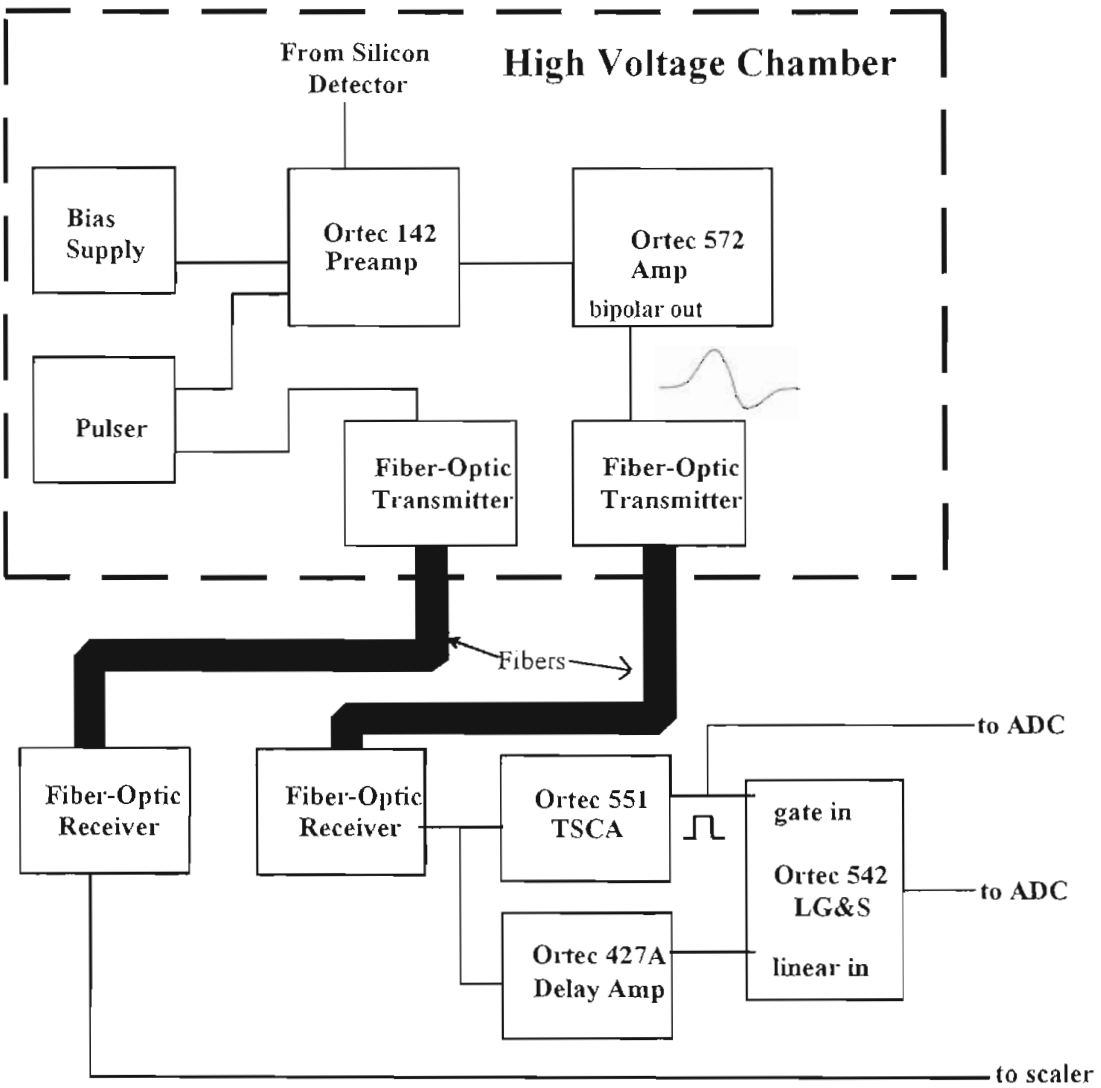

Figure 2.12: Detector Electronics: Fiber optic transmission links are used to send the amplified detector signals from the High-Voltage Chamber to the ground potential electronics. This scheme was repeated for each detector.

split and sent directly to the ADC gate input. The output of the 542 was sent to an ADC input for digitization.

2.5 Energetics

To achieve the desired uncertainties in the cross sections, reaction and scattering energies must be known very well. The reaction cross sections themselves have significant energy dependences at the lowest energies. All elastic-scattering yields are very sensitive to energy, but again are most sensitive at the lowest energies. Precise knowledge of the reaction energies requires knowing the incident beam energy as well as understanding energy losses in the targets.

2.5.1 Incident Beam Energy

The most important variable in determining a reaction or scattering energy is of course the incident beam energy. The beam energy is mostly determined by the potentials on the ion source, on the Mini Tandem, and on the High-Voltage Chamber. All potentials are read directly from digital voltmeters whose calibrations were previously determined by a procedure described elsewhere [Lud97]. Small corrections must be made for energy losses in the Mini Tandem carbon stripping foil and for the potential on the cesium in the charge exchange canal in the ion source. This cesium vapor facilitates a charge exchange reaction in order to produce the negative beams needed for the Mini Tandem. As a side effect, it acts like a very low-energy tandem accelerator. One should take care to keep track of the values of the cesium potential and the stripping foil thickness or make sure that they stay within acceptable known ranges if beam energies need to be known very precisely. Carl Brune wrote a small FORTRAN program called "emini.for"[Bru98] which uses these parameters to determine the energy of the beam exiting the Mini Tandem. The energy gained in the High-Voltage Chamber's acceleration tube must then be added when applicable.

2.5.2 Energy Losses

Energy losses in the targets must also be well known in order to determine precisely the reaction and scattering energies. Since the angular dependences of the differential cross sections vary slowly with energy, it is however, not critical to know the energies of the angular distribution data very precisely. The energy losses in the targets can be neglected for that part of the experiment. On the other hand, the overall magnitude of the reaction cross sections change more rapidly with energy, and in particular the elastic-scattering cross sections used to determine the normalization are very sensitive to energy. Thus care was taken to measure these energy losses for the normalization data. In particular, it was most critical to know these energy losses for the low-energy cross-normalization experiments. At these low energies all cross sections involved, reaction and elastic, have an increased sensitivity to energy.

For the low-energy normalizations a three-layer target was used. The deuteron beam first passed through a thin layer of ^{197}Au followed by a layer of D.P.P. and finally passed through a carbon backing. As explained in previous sections, elastic-scattering yields were measured from the gold and the carbon, and reactions were measured from the deuterium in the D.P.P. layer. Since energy is lost continuously throughout the thickness of the target, the reaction energy is less than the gold scattering energy which is less than the incident beam energy. Both interaction energies need to be known.

In order to determine the energy losses in the different target layers, we observed peak positions of backscattering data in the 164° monitor detector as shown in Figure 2.13. To accomplish this, data were taken at 480 keV with the targets in the usual orientation with gold facing upstream, and then again after rotating the targets 180° as shown in Figure 2.14(b). By rotating the target, incoming and outgoing particles for a particular interaction passed through different target layers. This caused the spectral positions of the peaks to move by an amount determined by differences in energy losses for the two orientations. Using this information all energy losses could be derived, some more directly than others.

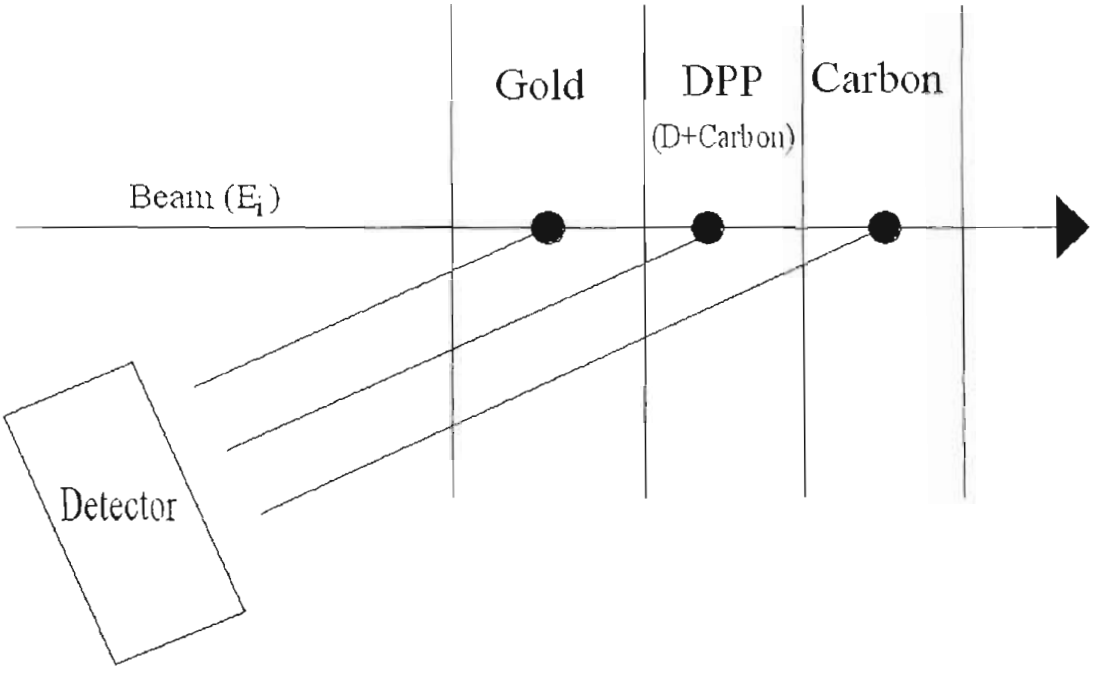

Figure 2.13: A schematic diagram of a target used for cross-section normalizations: The target consists of a D.P.P. deuteron target region, a carbon backing, and a gold layer for beam current normalization via Rutherford backscattering. It can be seen that several distinct trajectory regions must be considered in determining energies of backscattered particles for a single scattering peak.

Elastic scattering from carbon in the D.P.P. and in the carbon layers cannot be experimentally distinguished. Thus for now the carbon must be thought of as one layer, and the task is to determine energy losses in the carbon and the gold layers separately; see Figure 2.14(a). This distinction between the two carbon layers is handled separately via another method and is described later. Since the energy losses are only a few keV, the change in stopping powers throughout the carbon layer can be neglected. Also, since deuterium is light and has Z=1, it contributes very little to the stopping powers of the material and is neglected.

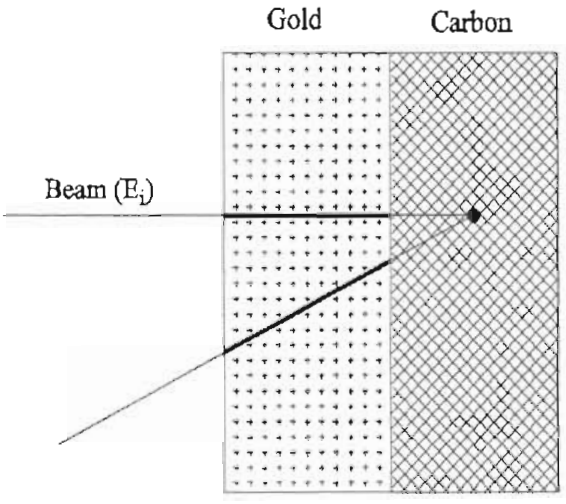

(a) Backscattering from carbon in a gold covered target in the standard orientation: The darker lines serve only to highlight the trajectories in the gold layer.

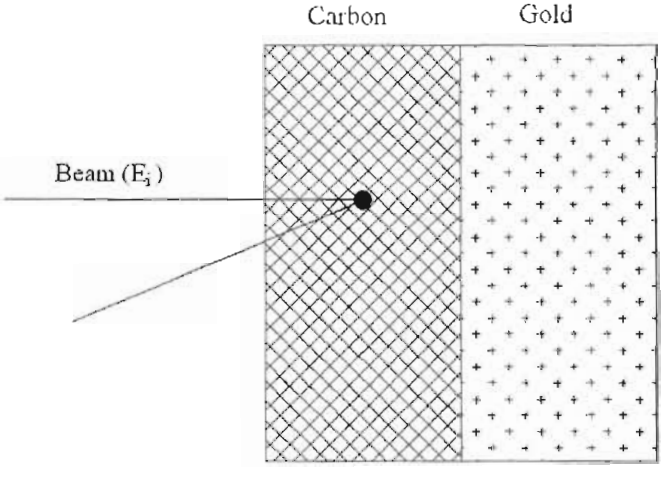

(b) Backscattering from carbon in a gold covered target in the reversed orientation

Figure 2.14: Diagram of backscattering from carbon in 2-layered carbon and gold targets: The energy losses due to carbon are approximately the same for the reversed and standard target orientations. The differences in observed energies for the two configurations are thus sensitive to energy losses in gold alone. Likewise, observations of scattering from gold are sensitive to energy losses in carbon.

Consider the $^{12}C(d,d)$ scattering peak position. Again since the stopping power is treated as constant over the range of beam energies in the target, the energy loss in the carbon layer itself is the same for both configurations as seen by examining the paths through carbon in 2.14(a) and 2.14(b). The detected energy for scattering from carbon then changes by an amount which depends only on the energy losses in the gold layer alone; again compare Figure 2.14(a) and Figure 2.14(b). Therefore comparison of the carbon peak positions detected in the standard and reversed target orientation give a direct measure of the sum of the energy lost by both the incoming and exiting particles as they pass through the gold layer.

It is not possible to measure directly the energy loss of the beam in the gold layer independently from the energy loss of the outgoing particle in the gold layer. This complicates the situation significantly. In a direct energy loss measurement we would like not to rely on previous knowledge of stopping powers. Here stopping power data must be used because there are two stopping powers, one for the incoming beam, and one for the outgoing particle, and only one observable change in energy. However, only the ratio of the stopping powers at the incident and scattered energies is needed; the values are not. This ratio varies even more slowly with energy than the stopping power itself and is less likely to be affected by systematic errors in the stopping power data. The needed stopping power data were obtained from the program SR.EXE in the well known TRIM92 software package written by Ziegler and since updated in the form of SRIM [Zie03].

Some algebra is needed to deconvolve the information regarding the two different energy losses in the gold layer. I will derive all the needed expressions for this as well as for the energy losses involved in scattering from gold. The channel positions J and J^B of the peaks with gold upstream and downstream (B for Backwards) respectively are given by

$$mJ_c^B + b = (E_i - \frac{1}{2}\Delta_c)K_c(\theta) - \frac{1}{2}sec(\theta)R_c^c\Delta_c \quad (2.6)$$

$$mJ_g^B + b = (E_i - \Delta_c - \frac{1}{2}\Delta_g)K_g(\theta) - sec(\theta)(\frac{1}{2}R_g^g\Delta_g + R_c^g\Delta_c) \quad (2.7)$$

$$mJ_g + b = (E_i - \frac{1}{2}\Delta_g)K_g(\theta) - \frac{1}{2}sec(\theta)R_g^g\Delta_g \quad (2.8)$$

$$mJ_c + b = (E_i - \Delta_g - \frac{1}{2}\Delta_c)K_c(\theta) - sec(\theta)(\frac{1}{2}R_c^c\Delta_g + R_g^c\Delta_g)\,, \quad (2.9)$$

where the subscripts and superscripts g and c represent gold and carbon respectively; J_l indicates scattering from layer l; E_i is the incident beam energy; Δ_l is the total energy loss of the incident beam in layer l; $K_l(\theta)$ is the ratio of scattered-particle energy to beam energy for scattering from layer l into the detector angle, $\theta = 164°$; the R_l^j is the ratio of stopping powers of scattered to incident beam in layer l for scattering from layer j; m and b are channel calibration constants such that $E_l = mJ_l + b$, and thus m has units of keV/channel and b has units of energy. The right hand sides of the above equations are written to suggest the proper physical order of events when read from left to right.

Subtracting Equation 2.7 from Equation 2.8 and Equation 2.9 from Equation 2.6 yields

$$\Delta_c = \frac{m(J_g - J_g^B)}{sec(\theta)R_c^g + K_g(\theta)} \quad (2.10)$$

$$\Delta_g = \frac{m(J_c^B - J_c)}{sec(\theta)R_g^c + K_c(\theta)}, \quad (2.11)$$

which is not altogether unintuitive from the figures. In principle Equations 2.6 through 2.9 can be solved in multiple ways to find the spectrum's linear calibration factor m, but in practice it was not necessary. It is immediately evident from the data that the energy loss in the gold layers is less than 1 keV. This along with the fact that the stopping powers in gold change by no more than 30% in the energy range of interest

implies that a calibration can be made by directly looking at gold peak positions in the normal orientation at different beam energies. That is what was done. There is very little energy loss in this configuration and since the stopping powers vary slowly, the energy loss that does exist should be nearly constant as a function of beam energy, affecting only the offset of the channel calibration, not the linear coefficient, m.

We are not done quite yet. Recall that the carbon layer is actually made up of a D.P.P. layer and a pure carbon layer, and for measurement of the reaction cross sections we are interested in knowing the central energy in the D.P.P. layer. Determining this energy requires knowledge the relative percentages of the carbon belonging to the pure carbon layer and to the D.P.P. layer so that we can attribute the appropriate amount of energy loss to each layer. Since the carbon in the two layers cannot be directly distinguished, information about the deuterium concentration must be used for this task.

From the chemical formula of D.P.P., C_6D_4, we know the ratio of deuterons to carbon atoms in the D.P.P. layer is 2 to 3, at least initially. Comparing the ratio of deuterium to carbon in the target to the known ratio for the D.P.P. layer will provide the needed information about the amount of remaining carbon in the pure carbon layer. The task then is to determine the ratio of deuterium to carbon in the target.

At 164° the scattered energy of deuterons from deuterium is too low to detect, so it is not possible to compare directly the elastic yields of carbon and deuterium. Instead I used the reaction yields from the forward-reaction detectors. All of the d-d reactions as well as $^{12}C(d,p)$ are clearly visible in the forward detectors. The ratio of the $^{12}C(d,p)$ reaction yield to the $d(d,p)t$ reaction yield, for instance, gives the ratio of carbon to deuterium in the target with a minor caveat: the differential cross sections for both must be known. I know the cross sections for the d-d reactions because that is what we have measured. Of course this is slightly circular since the energy loss measurements are for the purpose of making corrections to these reaction cross sections. However, the uncorrected values are sufficiently accurate to be used in this way, producing an error of the second order in the energy loss correction. The

^{12}C(d,p) reaction cross sections are not known from the literature and leave us yet again one step away from solving this problem which seemed so simple just a few paragraphs back. The ^{12}C(d,p) reaction cross sections can be obtained from the same data which were used to measure the reaction cross sections. Again, a negligible error of the second order in energy loss will be introduced in the same way as for the d-d reaction cross sections.

The ^{12}C(d,p) reaction cross section at 48° can be determined directly from the beam-switching normalization experiments. This can be done in a way very similar to how the $d(d,p)t$ and $d(d,n)^3$He reaction cross sections are determined. In fact ^{12}C(d,p) reaction cross sections can be derived at essentially all of the same energies and angles as the $d(d,p)t$ reaction. A detailed derivation of the analysis process as it applies to the $d(d,p)t$ and $d(d,n)^3$He reactions can be found in Section 3.2.1, but here I will give the needed equation for the current purpose with significantly less explanation for now.

The outgoing deuterons from carbon elastic scattering have more energy than those for d-d elastic scattering. Thus, unlike for the d-d elastic peaks, it was possible in many of the normalization reaction runs to see the ^{12}C(d,d) scattering peaks in the same detector as the ^{12}C(d,p) reaction. The ^{12}C(d,d) elastic-scattering cross section can then be measured from known ^{12}C(p,p) scattering cross sections [Mey76] using data from the beam-switching runs. Again Rutherford scattering from gold is used to determine the relative number of incident beam particles for the proton and deuterium beams. The differential cross section is determined from

$$\sigma_{C(d,p)}(E_p,\theta) = \frac{N^r_{C(d,p)}}{N^r_{C(d,d)}} \frac{N^d_{C(d,d)}}{N^p_{C(p,p)}} \frac{N^p_{Au(p,p)}}{N^d_{Au(d,d)}} \frac{\sigma_{Au(d,d)}(E_d,\theta)}{\sigma_{Au(p,p)}(E_p,\theta)} \sigma_{C(p,p)}(E_p,\theta)\,, \tag{2.12}$$

where the superscripts represent the data set type, r representing reaction data runs with deuteron beams, d for deuterium elastic-scattering runs, and p for proton elastic-scattering runs. As usual the deuteron and proton elastic-scattering runs were performed on the same target. The deuteron-beam elastic and reaction data are taken

from runs at the same energy of 480 keV used to determine the target composition in question. After determining the differential cross section of $^{12}C(d,p)$ reactions at 48°, angular distribution data are used to interpolate to 44° where a value is needed to determine the energy losses in the low-energy cross-normalization runs.

Working back toward the solution of our original problem, the ratio of deuterium atoms n_D to carbon atoms n_C in the target in question is then determined using data from the 48° detector from a run taken at 480 keV in the low-energy normalization experiments. The expression for this ratio is

$$\frac{n_D}{n_C} = \frac{N_d(d,p)}{N_C(d,p)} \frac{\sigma_{C(d,p)}(\theta)}{\sigma_{d(d,p)}(\theta)}, \tag{2.13}$$

where the yields indicated are now from the data sets from the targets for which we want to know the energy losses. The amount of carbon in the D.P.P. layer as a fraction of the total amount of carbon is then just the above ratio times the ratio of carbon to deuterium in the D.P.P. layer, which is again just 3/2 as given by the chemical formula for D.P.P.

We now have all information needed to determine reaction energies at the center of any target layer by using Equations 2.10 and 2.11 and the information about how to subdivide the energy losses in the carbon layer. Since Δs are energy losses for full target layers at 480 keV, the appropriate energy losses needed to determine the central energy for each reaction were determined by multiplying the Δs by the appropriate ratio of stopping powers for all beam energies of interest. I use the term reaction loosely here to refer to scattering as well. For reactions in the deuterium layer, the result is then multiplied by the fraction of carbon in the D.P.P. layer to the total amount of carbon. For a given reaction, I use 1/2 of the total the energy loss of the beam in the reaction layer plus the energy loss of all upstream layers to determine the central reaction energy for that layer. The fusion reaction cross sections are reasonably linear and the gold layer is sufficiently thin to easily justify neglecting any more complicated cross-section weighting effects. Energy losses were measured this way for all low-energy

Nominal Energy (keV)	Incident Deuteron Energy (keV)	Total Loss in Gold (keV)	Total Loss in D.P.P. (keV)	Central Deuterium-Layer Energy (keV)
480	477.0	0.5	7.1	473.0
320	317.3	0.2	5.1	314.5
240	237.2	0.5	7.9	232.7
180	177.3	0.5	8.1	172.7
120	116.8	0.4	8.5	112.2

Table 2.1: Energy corrections for low energy normalizations: The final interaction energy is calculated using the total energy loss in gold and half of the D.P.P. energy loss. The values are associated with the particular targets used to normalize cross sections at each of the lowest four energies to those at 480 keV. The values for 480 keV vary slightly for each of these targets. The ones shown are for the target used for the 120 keV normalization.

normalization targets and for a sample of high-energy normalization targets for which energy losses were less critical. Final values of incident beam energies and total energy losses in the gold and deuterated layers are given in Table 2.1.

The high energy normalizations were performed on two-layer targets, a gold layer and a deuterated amorphous carbon layer. For these normalizations, Equations 2.10 and 2.11 alone could be used to determine the energy losses in the targets. In practice, rotated target data were taken for only one of these targets and were taken using a deuteron beam. A relative thickness measure was then derived by taking the ratio of counts in the elastic-scattering peak to the number of pulses generated by the beam-current integrator. This relative measure was calibrated with the rotated target data and then used to measure the thickness of the other targets. The results are shown in Table 2.2.

Because some of the high energy normalizations were performed consecutively without changing the amplifier gains, direct comparison of peak positions from the different targets could also be used as a cross check. This method is not as reliable because the gains in the fiber-links sometimes shifted slightly when the fibers were jostled during target changes. Still, where this method was used as a check, the central energies derived for scattering of deuterons from the carbon layer agree with the beam integrator technique to within 1 keV. Deuteron beams were used because the deuteron stopping powers are larger than the proton stopping powers making the $^{12}\mathrm{C}(d,d)$ scattering peak position more sensitive to the target thickness than the $^{12}\mathrm{C}(p,p)$ scattering peak. For protons, since stopping powers are lower, agreement of the results for proton energies derived from the deuteron data is enhanced to roughly 0.5 keV. The energy losses in gold were measured to be about 0.1 keV, below the uncertainty in the peak positions for the given statistical and fitting uncertainties. They were neglected.

Nominal Deuteron Energy (keV)	Incident Deuteron Beam Energy (keV)	Central Deuteron Beam Energy (keV)	Incident Proton Beam Energy (keV)	Central Proton Beam Energy (keV)
660	653.2	646.1	653.6	649.0
570	564.4	557.3	653.6	649.4
570			564.8	560.2
480	477.0	470.2	564.8	560.8
390	387.4	379.3	564.8	560.4

Table 2.2: Energy corrections for high-energy normalizations: Each row depicts data for the deuteron energy being normalized and the proton energy used to normalize it. Two proton energies were used on the same target to normalize the 570 keV deuteron data. Variations in energy losses between rows come from varying stopping powers and variations in target thicknesses.

2.6 Zero Crossing

Small corrections to the angle settings were also needed. The angles of rotatable detectors in the High-Voltage Chamber are selected by rotating the detector plates from outside the chamber and reading the angle setting on a vernier scale with a relative accuracy of roughly 0.1°. I use the word "relative" because the exact true angle setting depends on the alignment of the chamber with the beam line. The chamber was aligned using a surveillance scope, but it is difficult to obtain a sufficiently accurate alignment. For this reason the offset of the angle settings is measured experimentally. The basic procedure has been described several times before; see reference [Fis03]. We took angular distributions of $^{12}C(p,p)$ scattering at $E_p = 477.3$ keV at forward angles for left and right detectors for positive and negative angles. By "negative" I mean moving a right detector to the left side(or left to right), hence the term "zero crossing". This was done for the four rotating detectors used for normalization to $d(p,p)$ and was performed immediately before the normalization experiments. This zero-crossing determination was not performed for the third detector set used for the angular distribution experiments. In fact it is the $d(p,p)$ yields alone that are sensitive to very small changes in detector angle so it was not necessary to measure the zero crossing for this third detector set.

A χ^2 fit was made to the angular distribution data with the normalization and 0° offsets as free parameters. The function used for the fit was an R-matrix parameterization routine for $^{12}C(p,p)$ programmed by Brune [Bru98] which used the R-matrix parameterization of Meyer [Mey76].

Usually zero-crossing fits do not produce reduced χ^2 equal to 1, but often something closer to 5 or 10. This is because of inaccurate cross-section functions, and because the extreme sensitivities to angle combined with small variations in the relative angle settings produce variations which are usually larger than the statistical uncertainties. An extra uncertainty which corresponded to the uncertainty in the human ability to set the angles was added to the data in the fit. This uncertainty was added in quadrature

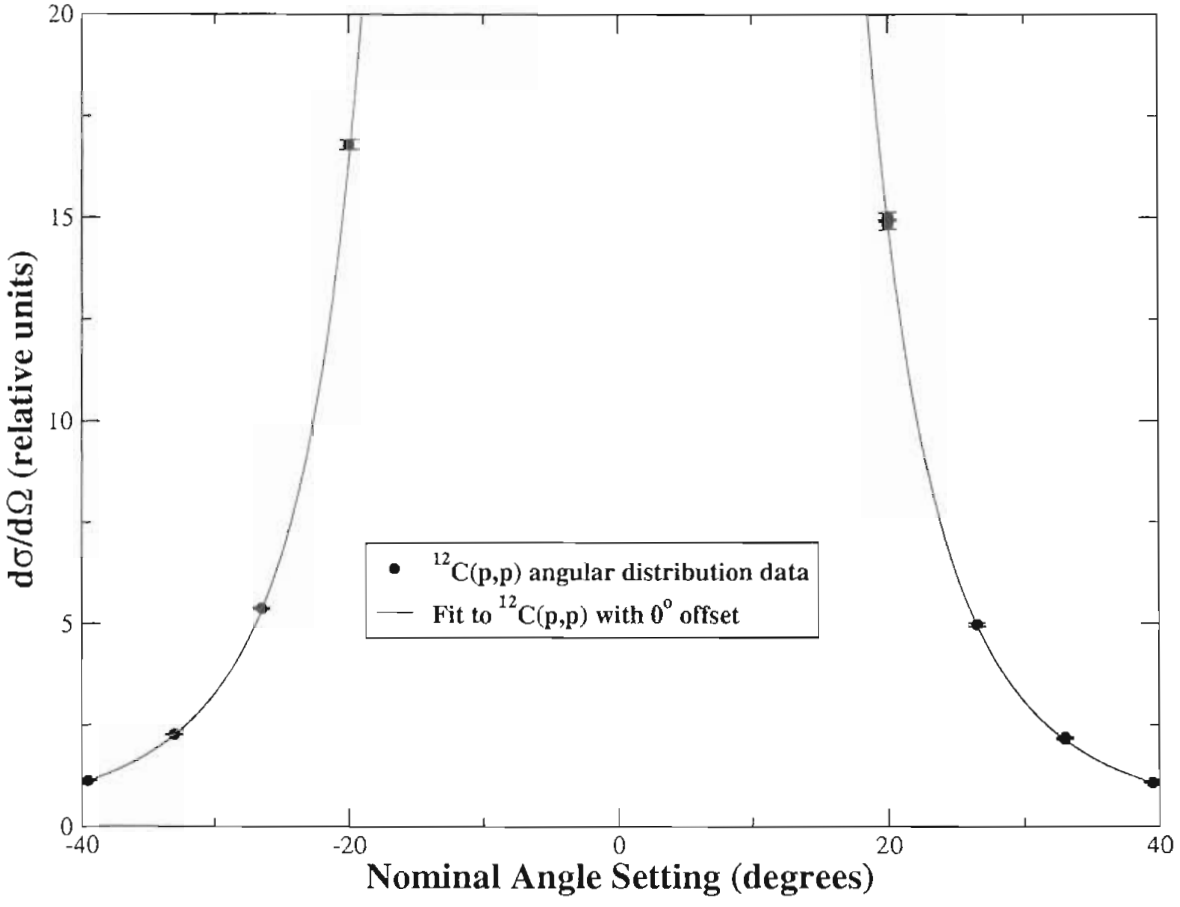

Figure 2.15: Fit to $^{12}C(p,p)$ zero-crossing data: The data are from an angular distribution for the back-right detector. The curve is a fit to an R matrix parameterization of $^{12}C(p,p)$ scattering with the angle offset and overall normalization as free parameters. The uncertainties shown are from counting-statistics only.

iteratively in all fit passes. This was done by making the uncertainty always equal to the error in the angle setting, by default 0.1°, multiplied by the current value of the slope of the fit function at the angle of each individual data point.

With this combination of realistic uncertainties and an accurate cross-section function, reduced χ^2 for the zero-crossing fits of the present work were usually significantly less than 1. This indicates that the variation in the angle settings were less than 0.1°. This variation, not the error in the offset parameter, is the uncertainty associated with the setting of any single angle and is thus the relevant uncertainty for many situations.

An upper limit of 0.1° is usually assumed for this error when using the rotating plates on the High-Voltage Chamber.

The results for the best fit values of the zero-offset parameters for each detector are shown in Table 2.3. In addition to the results shown in this table, corrections were

Detector	θ_{offset} (degrees)
front-right	-0.30
back-right	-0.60
front-left	0.58
back-left	0.25

Table 2.3: Lab angle corrections for four p-d normalization detectors which were also used as the front four rotating detectors for the angular distribution measurements: In the table "front"("back") refers to the pair of detectors positioned at a more forward(backward) angle when the detectors are on their proper side of the chamber. $\theta_{true} = \theta_{nominal} + \theta_{offset}$

deduced for all detectors which were not present during the zero crossing experiment and which were later mounted on the rotating plates. As stated above these detectors were only used for experiments with very low sensitivities to angle settings. To deduce angle corrections for these detectors, the assumption was made that most of the zero crossing correction was due to a systematic misalignment of the rotating plates and less was attributable to variations in the placement of particular detectors. The values were found by estimating this mean plate offset. For the left side a correction of 0.40° was used, and for the right side a value of -0.45° was used.

Uncertainties in the cross section arising from uncertainties in detector angles are discussed in Section 3.5.3.

Chapter 3

Data Analysis

Analyzing the large volume of data from these experiments was a complex and multi-layered task. My goal in the analysis was to make use of all the interconnected data constraining various physical and experimental parameters without double counting any statistics and to understand the correlations in the uncertainties on the final results. By using a chi-squared analysis to fit all the data to a model constructed from the relevant parameters it was possible to maximize the amount of information used while appropriately handling and quantifying correlated information and uncertainties. The outcome is more thorough use of statistics and a better understanding of the correlations in the resulting uncertainties as given by the parameter error matrix. In this chapter I will first discuss the fundamental spectral analysis and data preparation and proceed to a description of the fit used for the final analysis. Finally I will discuss contributions to, and the analysis of, uncertainties in cross-section results.

3.1 Spectral Analysis

Depending on how it is counted, this experiment used about a dozen types of peaks of significant interest in 5 types of measurements with an average of about 9 detectors at any one time, and that does not include minor systematic measurements. Multiplied over the numerous repeated runs, there were literally a few thousand peaks to analyze. The first and most tediously arduous task required in order to analyze all

of the data was simply to determine the number of counts in all of these peaks. This was done with a combination of simple peak summing, background subtraction, and peak fitting depending on the situation.

The first step was simply to identify and mark the location and type of all peaks of interest in all data runs. I accomplished this using XSYS, an old and simple data analysis package. I used a version of XSYS which has been ported to operate in a Linux environment. XSYS has a particularly simple interface for marking and saving peak locations with "gates" (two channel values marking a region of interest) and associating them with a particular gate number which can be used to identify the peaks. I went through every reaction and elastic peak of every run in every detector and set gates by hand. One may find this archaic; surely there must be some hi-tech software to automate such a process. It may be possible to automate some parts of the process, but in the end the wide variety of data, coupled with a need to visually verify the contents and integrity of the data, dictated that this was the best method.

After marking peak locations and types, some analysis was needed to determine the number of counts in the peaks. For many of the reaction peaks the spectra were clean enough simply to sum the number of counts in the gate location. A built-in XSYS function was used for these cases. More difficult situations arose when peaks were contaminated with significant background. During the angular distributions measurements for some energies and angles the ^{3}He peaks and sometimes the triton peaks would have backgrounds coming from electronic noise and/or pile-up of multiple low energy events in the detector or electronics. In these cases a second gate was set wider than the peak gate. These gate endpoints were used as locations for sampling the background around the peak. An XSYS routine was used to fit a background for the peak by sampling the background value at 10 points around each of these two gate endpoints. The form of the background was usually chosen to be linear. This background was then subtracted from the spectrum before taking the sum inside the peak gate. See Appendix A for a derivation of the formula used for determining the statistical uncertainty associated with the background subtraction, Equation A.8.

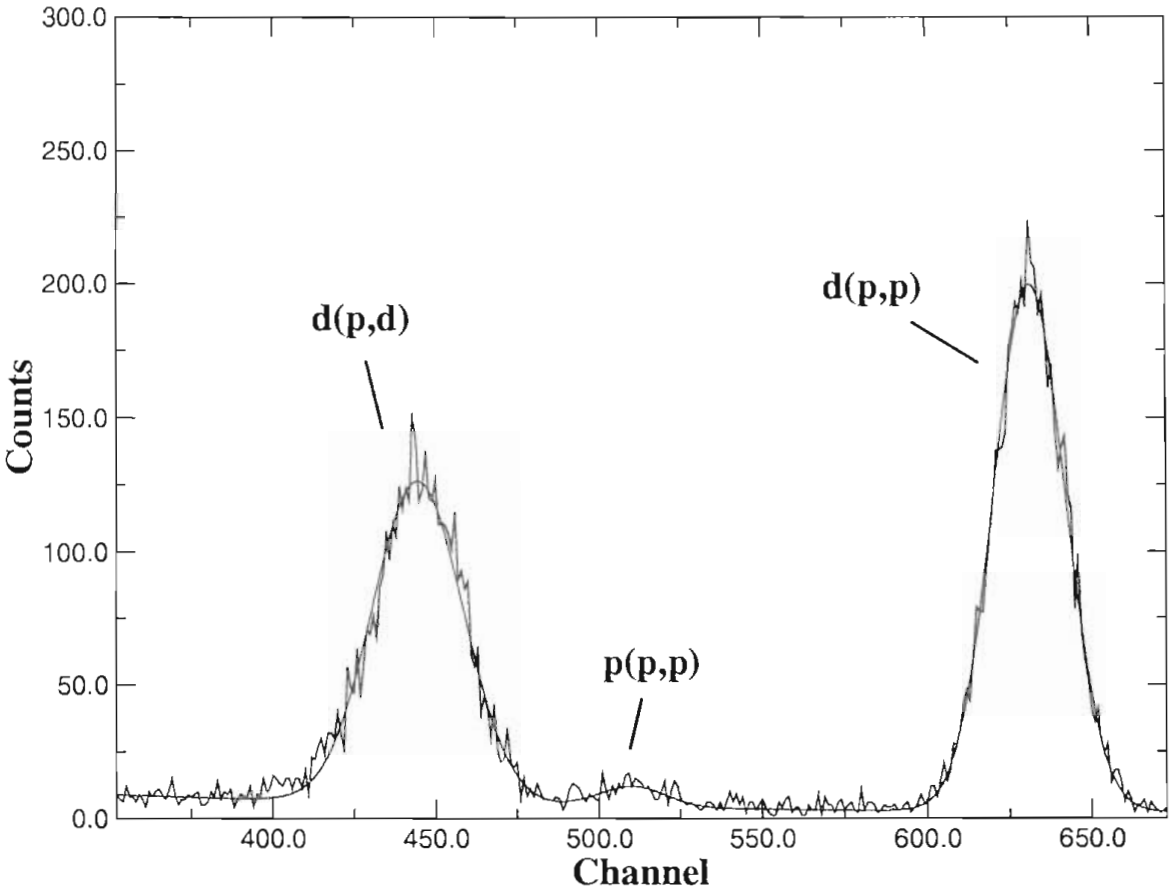

Figure 3.1: Fit to spectrum obtained from proton-beam elastic scattering from a deuterated target at $E_p = 480$ keV. The smooth fitted curve is composed of three Gaussian peaks and a quadratic background.

Direct background subtraction is often the best solution for separating a peak from the background. It does not depend on a good understanding of the peak shape so it is preferred when the background subtraction is a small correction, when the background shape is simple, and especially when peak shapes are complicated. However, for larger or more complicated backgrounds or when multiple peaks are partially merged, peak fitting must be performed. I used peak fitting to find the area under many of the elastic-scattering peaks. One of the most common methods of peak fitting is χ^2 minimization. The principle is described in any introductory data analysis text book [Tay97, Bev92]. The idea is to construct a function with several parameters that can be adjusted to fit the peak. The parameter space is then searched to minimize

χ^2, a value characterizing the quality of the fit. I used simple Gaussian peaks and low-order polynomial backgrounds, usually quadratic. An example of a curve fit to an elastic-scattering spectrum is shown in figures 3.1.

A Gaussian function $g(x)$ can be parameterized by the standard deviation σ , centroid c, and area A. The following gives the expression for $g(x)$:

$$g(x) = \frac{A}{\sigma\sqrt{2\pi}} e^{-\frac{1}{2}(\frac{x-c}{\sigma})^2} \tag{3.1}$$

By parameterizing the Gaussian function in this way, the area is directly determined by one of the three fitting parameters. This allows the error determined for the fit parameter to be used directly as the error in our peak area without the need to propagate errors from multiple parameters. I used the MINUIT FORTRAN libraries [Jam94] to minimize χ^2. MINUIT itself does not calculate χ^2; it only minimizes a user defined function by varying the input parameters. I used the covariant error calculated by MINUIT for the error in the area parameter. The covariant error matrix includes information about all parameter uncertainties and all correlations between parameters. It is the inverse of the second derivative matrix T, where T is defined with respect to the parameters p_i as follows:

$$T_{ij} = \frac{\partial^2 \chi^2}{\partial p_i \partial p_j} \tag{3.2}$$

The diagonal elements of T have information regarding the effect of one parameter on χ^2 with all other parameters fixed. The diagonal elements of its inverse, the error matrix, give the total uncertainties in the parameters including effects from parameter correlations. The statistical uncertainty, or error, in a parameter is the amount the parameter must be changed to increase χ^2 by 1. However, to find the full error if there are parameter correlations, it is not sufficient simply to vary the single parameter until this occurs. Instead, after varying the parameter all other parameters

must be re-optimized. Moving the first parameter may cause other parameters to have new best fit values. This re-optimization may thus cause χ^2 to be reduced, partially canceling the effect of moving the original parameter. This allows the parameter of interest to be moved further from its original minimum before increasing χ^2 by 1. One can imagine an iterative procedure that would converge on the largest possible adjustment of the parameter of interest while still maintaining a change in χ^2 of no more than 1. It should be clear that this procedure will never produce errors smaller than the original uncorrelated calculation. Parameter correlations in a χ^2 fit never decrease uncertainties [Jam94]. To leading order the diagonal elements of the error matrix represent the results of the process just described. See Appendix B for tips on obtaining the error matrix elements from MINUIT.

Considering parameter correlations in fit uncertainties is very important and often overlooked. If a parameterization is not orthogonal, the correlations may greatly increase the resulting uncertainties. Consider a simple model where an observable c is related to two parameters a and b by the equation $c = a + b$. Now, if there is one measurement of c with a one standard deviation uncertainty ς_c, a fit of the parameters a and b can be found to reproduce the data. After finding such a solution, if a is held fixed and b is varied, the error in b will be found to be exactly ς_c because varying it more than this will cause $a + b$ to be outside the uncertainty in c. However, if both parameters were allowed to vary, then b could be varied without limit and still produce a fit equally as good as the original fit. Indeed, ignoring error correlations leads one to fail to notice that the uncertainty in b is in fact infinite! Unfortunately, most correlation problems are much more subtle than this and should be handled with some care.

Returning to the immediate issue, fitting the d-d scattering peaks added a minor extra step. As mentioned in Section 2.2.4, For 390 keV and 480 keV the $p(d,p)$ scattering peak could not be separated from the $d(d,d)$ scattering peak in the d-d elastic monitor spectra. The peak was extracted by constraining its area to be proportional to the area of the $p(d,d)$ scattering peak. The three peaks were fit

simultaneously with a single quadratic background. Instead of using three parameters for each peak, only two, centroid and standard deviation, were used for the $p(d,p)$ peak. The area was set proportional to the area parameter used to simultaneously fit the $p(d,d)$ peak. The proportionality constant was obtained using data from elastic scattering of a deuteron beam on a hydrogenated target. This constant had a very flat energy dependence from 390 keV to 660 keV.

In summary, I wrote configuration files to describe which peaks to sum and which peaks to fit for a group of data runs. I then wrote a small code to automate the process of summing and fitting which thus interfaced the XSYS spectra and gates with the MINUIT libraries when needed. The results for all runs in a series were then stored for further analysis.

3.2 Crunching Numbers

The complete analysis procedure involved a simultaneous fit of all data collected to energy dependent differential cross-section functions as well as some experimental parameters. However, before performing this fit, all data were adjusted for deadtime corrections, monitor normalizations, and cross-section normalizations as needed. In this way a more conventional analysis could be performed first, and all run-dependent parameters could be removed. For example, the total amount of beam on target for each run, or any relative measure of it, cannot reasonably be parameterized in a fit. I have analyzed literally hundreds of data runs so this would require several hundred parameters. Such a parameterization is unnecessary anyway since any statistical errors from these run-dependent parameters, by definition cause no correlations between different runs, only minor correlations between different data for a single run. Hence, before constructing a global fit to all of the data, preliminary data normalizations were needed. I will first describe the basic normalizations performed on each data type and some analysis results from the individual data types before giving a complete description of the global fitting procedure.

As explained already in Section 2.4, data of all types were first corrected to account for counts which were lost when the data acquisition system was busy. Statistical errors in the deadtime corrections were calculated using the square root of the counts missing from the pulser peak. The generation of counts in the pulser peak itself is not a random process. It is the removal of counts which is random, hence the use of the missing counts to derive errors. I explain this here mostly as a pedagogical note because it can be important under certain conditions. Given our low deadtimes, always kept below a few percent, and ample pulser statistics, the error from the deadtime correction was a small fraction of a percent at worst. Under these conditions statistical deadtime uncertainties had essentially no effect on the overall errors in the measurements.

3.2.1 High-Energy Normalizations

As explained in Section 2.2.3 the highest-energy differential cross sections were normalized to the known p-d elastic-scattering cross sections. In this section I will explain the procedure needed to obtain absolute reaction cross section from the p-d cross sections. First recall the general yield equation first introduced as Equation 2.1. Here I will ignore the detector efficiency since it is essentially unity for silicon detectors, and even if it were not, it could be folded into the solid angle with no change in the result for these purposes. The yield equation is then

$$N = nt\Delta\Omega\sigma(E,\theta)\,, \tag{3.3}$$

where again N is the number of counts collected in the detector, or the unnormalized yield, n is the number of beam particles incident on the target, and t is the target areal density or "thickness".

I will construct the specific yield equations for all reactions and runs needed in order to calculate the cross section for $d(d,p)t$ reactions. For simplicity I will assume that each yield was observed in only one detector and one data run. I will refer to the

detector used to measure p-d elastic-scattering yields as detector A. The d-d elastic-scattering yield was observed in detector B in a beam switching run. These two runs used the same target, which I will call target 1, having a deuterium target thickness t_{d1} and a gold target thickness t_{g1}. Finally d-d elastic scattering was measured in detector B simultaneously to measuring the d-d reactions in detector A. These measurements were made using a different target, target 2. For all three measurements gold scattering was measured in detector C. I will use the convention introduced in Section 2.5.2 and use the superscript p for proton runs, d for deuteron beam-switching runs, and r for reaction runs with deuteron beam. These will label the yields, the beam energies, and the integrated beam flux on target. Subscripts will indicate reactions where needed. The yields of interest are as follows:

$$N^p_{d(p,p)} = n^p t_{d1} \Delta\Omega_A d\sigma_{d(p,p)}(E^p, \theta_A) \tag{3.4}$$

$$N^p_{Au(p,p)} = n^p t_{g1} \Delta\Omega_C d\sigma_{Au(p,p)}(E^p, \theta_C) \tag{3.5}$$

$$N^d_{d(d,d)} = n^d t_{d1} \Delta\Omega_B d\sigma_{d(d,d)}(E^d, \theta_B) \tag{3.6}$$

$$N^d_{Au(d,d)} = n^d t_{g1} \Delta\Omega_C d\sigma_{Au(d,d)}(E^d, \theta_C) \tag{3.7}$$

$$N^r_{d(d,p)} = n^r t_{d2} \Delta\Omega_A d\sigma_{d(d,p)}(E^r, \theta_A) \tag{3.8}$$

$$N^r_{d(d,d)} = n^r t_{g2} \Delta\Omega_B d\sigma_{d(d,d)}(E^r, \theta_B) \tag{3.9}$$

It can "clearly" be seen then that the solution for the $\sigma_{d(d,p)}(E, \theta)$ cross section is given by the following:

$$\sigma_{d(d,p)}(E^r, \theta_A) = \frac{N^r_{d(d,p)}}{N^r_{d(d,d)}} \frac{N^d_{d(d,d)}}{N^d_{Au(d,d)}} \frac{N^p_{Au(p,p)}}{N^p_{d(p,p)}} \frac{\sigma_{Au(d,d)}(E^d, \theta_C)}{\sigma_{Au(p,p)}(E^p, \theta_C)} \sigma_{d(p,p)}(E^p, \theta) \tag{3.10}$$

In order to analyze the data one run at a time, I broke this solution into the factors

corresponding to the three different run types. This also breaks the process down into more meaningful chunks and will lead to a backwards derivation of Equation 3.10. The factors α are

$$\alpha^p = \frac{N^p_{d(p,p)}}{N^p_{Au(p,p)}} \frac{\sigma_{Au(p,p)}(E^p, \theta_C)}{\sigma^p_{d(p,p)}(E^p, \theta_A)} \tag{3.11}$$

$$\alpha^d = \frac{N^d_{d(d,d)}}{N^d_{Au(d,d)}} \sigma_{Au(d,d)}(E^d, \theta_C) \tag{3.12}$$

$$\alpha^r = \frac{N^r_{d(d,p)}}{N^r_{d(d,d)}} \tag{3.13}$$

and now we have simply

$$\boxed{\sigma(\theta)_{d(d,p)}(E^r, \theta_A) = \frac{\alpha^r \alpha^d}{\alpha^p}}. \tag{3.14}$$

Ignoring solid angles, which cancel only when all three factors are considered, the value α^p is a measure of deuteron target thickness divided by gold target thickness. This follows simply from expanding out the two yields in Equation 3.11. The cross-section dependence of the $d(p,p)$ scattering yield is directly divided out, leaving only a dependence on the integrated beam flux and the deuterium thickness. The situation is analogous for the ^{197}Au(d,d) scattering yield appearing in the denominator, so the integrated beam flux dependence is canceled leaving only the two target thicknesses as claimed. The value α^d then produces the same result but with the $d(d,d)$ scattering cross section left in place. Hence the ratio of α^d to α^p leaves only the $d(d,d)$ cross section. And finally α^r directly relates this $d(d,d)$ scattering cross section to the reaction cross sections. Summarizing now, with the solid angles thrown in, we can rewrite the α's in terms of the unknown experimental parameters instead of in terms of the knowns and observables:

$$\alpha^p = \frac{\Delta\Omega_A}{\Delta\Omega_C}\frac{t_{d1}}{t_{g1}} \tag{3.15}$$

$$\alpha^d = \frac{\Delta\Omega_B}{\Delta\Omega_C}\frac{t_{d1}}{t_{g1}}\sigma_{d(d,d)}(E^r,\theta_B) \tag{3.16}$$

$$\alpha^r = \frac{\Delta\Omega_A}{\Delta\Omega_B}\frac{\sigma_{d(d,p)}(E^r,\theta_A)}{\sigma_{d(d,d)}(E^r,\theta_B)} \tag{3.17}$$

Focusing on the solid angles, it is now evident that Equation 3.14 cancels all solid angles which completes the somewhat backwards demonstration of the validity of Equation 3.10.

To calculate α^p, differential cross-section values were needed for p-d elastic scattering. Theoretical calculations were provided by Kievsky [Kie01] [Kie95] for several selected energies in the range of interest for the present work. Data were provided in one degree steps in the center of mass. I used two-dimensional polynomial interpolations to obtain values for the precise angles and energies needed. The error associated with the interpolation is negligible.

It may seem impossible to obtain a total uncertainty on the scale of a couple of percent with an observation depending on so many direct observables. However, the only place where significant systematic error is involved is in possible target thickness variations between proton and deuteron beams. As explained, the only terms which do not vanish exactly in the α^p and α^d factors are the target thickness terms. The α^r factor introduces no significant systematic error. Understanding the errors primarily requires inclusion of the usual statistical errors associated with all yields involved and a measure of the scatter in target thicknesses observed during a series of proton and deuteron beam switching runs. The statistical uncertainties are dominated by the reaction yields alone. Roughly 15,000 or more reaction counts were obtained in the reaction detectors for each detector angle and for each reaction, producing approximately a 1% statistical error. Other systematics uncertainties such as angle settings and background subtractions are discussed later in Section 3.5.

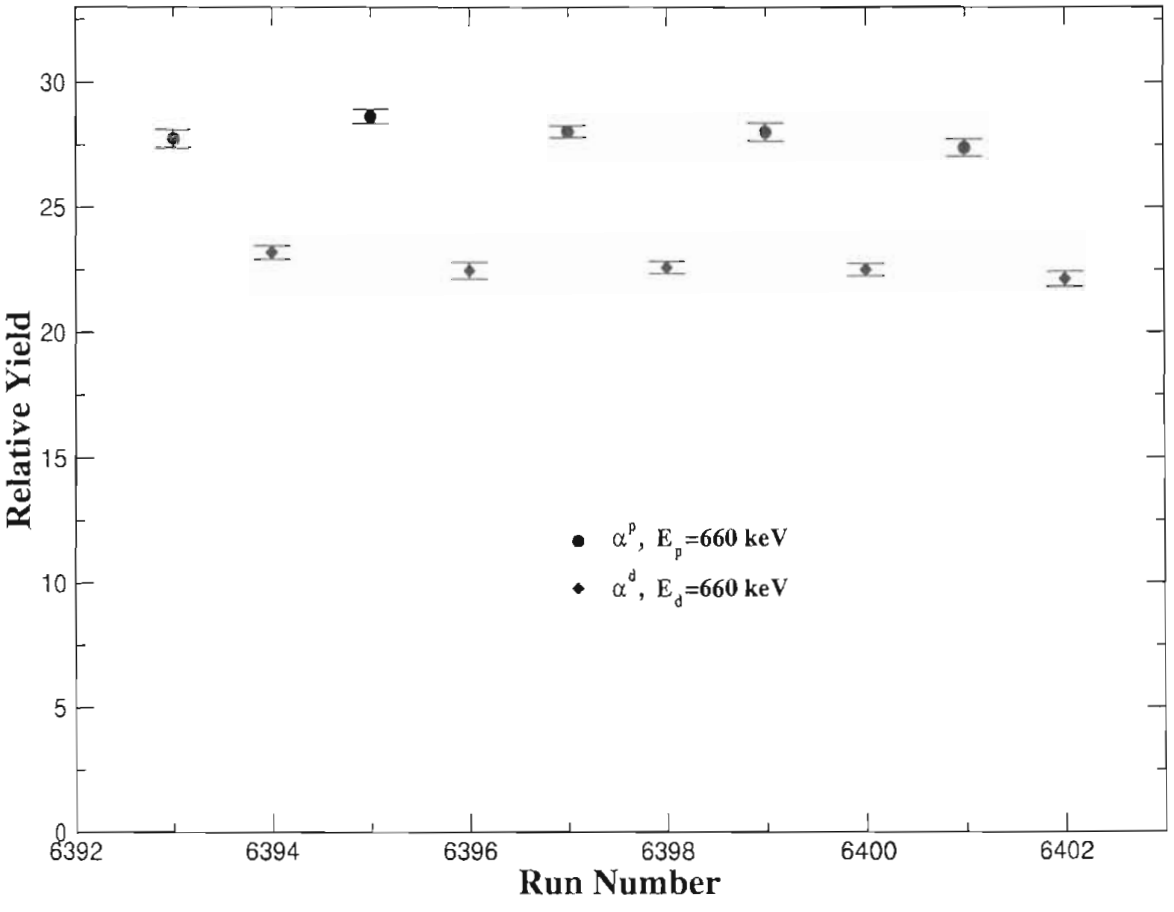

Figure 3.2: Relative yields measured in beam-switching normalization runs: α^d and α^p are the normalized $d(d,d)$ and $d(p,p)$ yields as defined in Equations 3.12 and 3.11.

The error due to target thickness variation can be seen by plotting the values of α^p and α^d as a function of run number. Run numbers were incremented consecutively as beams were switched between proton and deuteron beams. Because of the differences in the physical meanings of the two factors it is not possible to plot these together on any absolute scale, at least not in a very quantitatively meaningful way. The goal here is to obtain a consistent ratio between the two, so we are only interested in relative variations in each factor which could indicate variations in the target thickness. The results for the 660 keV normalization are shown in Figure 3.2. The two factors are shown in relative units. These results were obtained by treating the 35° detector pair as a single detector. Inclusion of both detector pairs will be discussed further in Section 3.4.

3.2.2 Angular Distributions

The most difficult aspect of analyzing the angular distributions has already been discussed, this being peak selection and background subtraction for a large data set. Once deadtime corrected yields exist for all rotating and monitor detectors, the only task is to normalize the rotating detectors properly so that they can be plotted on the same relative scale. This primarily involves dividing them all by the same monitor detector yields. As always, it was a little more complicated in practice. As a result of the problems discussed in Section 2.3 not all peaks were always useable in all detectors. Rotating detectors were placed with the left and right detectors at the same angle. Assuming for now that they have the same solid angle then all that is necessary to obtain a consistent result for a peak in a given rotating detector pair is to sum the peaks from the useable detectors in the pair and divide by the number of detectors included, either one or two. Since there are only two detectors in a pair, the only automated process for detecting partially blocked detectors is to compare the two yields and look for a consistent ratio. If the yields are inconsistent, it is impossible to tell how many of the two yields are incorrect using this procedure. Thus data from both detectors would need to be discarded. For this reason, the decisions were made manually using the consistency of the two detectors along with information about the particular chamber arrangement which could usually conclusively determine which detectors were in danger of blockage. If the left and right results were inconsistent and there was any doubt that the problem was isolated to one detector then both detectors were excluded for that setting. The probability that both detectors would be partially blocked by the same amount is very small and was generally checked experimentally by perturbing the settings in the chamber setup.

Monitor detectors as well as rotating detectors were sometimes partially blocked by a rotated target rod. Because the target region is not point-like, it was even possible for both monitor detectors on the same side to be partially blocked. Since there were four monitor detectors, automated outlier detection could be performed without throwing out excessive data. This was done simultaneously with monitor-detector solid angle

normalizations in an iterative process. In order to use any combination of monitor detectors, as for the rotating detectors, it was necessary to normalize the monitor detectors to their relative solid angles. The sum of the useable detectors could then be divided by the number of detectors and the result used as a single monitor-detector effective yield.

I will explain the algorithm used to accomplish the outlier detection and normalization. The counts in the triton and proton peaks in the monitor detectors were summed together before performing this normalization algorithm. The goal here was to compare an appropriate division of a particular monitor yield by the sum of other monitor detectors in that run to the average of the same ratio for all runs and use this comparison to remove outliers. First an entire set of runs for an angular distribution was analyzed, and for each run number i and monitor detector j, the following ratio $q_{ij,\{s\}}$ was calculated normalizing the monitor to the sum of the set of all monitor detectors $\{s\}$:

$$q_{ij,\{s\}} = \frac{M_{ij}}{\sum_{l\epsilon\{s\}} M_{il}}, \tag{3.18}$$

where M_{ij} is the deadtime corrected yield in the j'th monitor detector for the i'th run. The sum is over all elements l of the set s. The mean value $\bar{q}_{j,\{s\}}$ of the $q_{ij,\{s\}}$'s was then calculated for each detector j averaged over all runs. The quantities q and $\bar{q}$ were also calculated for each possible subset of monitor detectors $\{m\}$ to be summed, again for every i'th run and j'th detector.

The comparison value C_{ij} is defined as

$$C_{ij} = abs(\frac{q_{ij,\{m_i\}}}{\bar{q}_{j,\{m_i\}}} - 1), \tag{3.19}$$

where $\{m_i\}$ here is the set of all monitor detectors which have not yet been removed from the run i. The C's were calculated for all detectors and all runs and the uncertainty in the C, ς_C (ς is used instead of the conventional σ to avoid confusion with

the notation for cross sections), was calculated as well. A quality factor Q was then determined:

$$Q = \frac{C}{\varsigma_C} \tag{3.20}$$

The run and monitor detector with the largest value of Q over a threshold level of 2 was then marked as removed and the process was repeated, recalculating all q's, $\bar{q}$'s, C's and Q's and removing monitor detectors until no Q's greater than 2 were found. In consecutive passes the $\bar{q}_{j,\{m\}}$'s were calculated by averaging $q_{ij,\{m\}}$ only over runs where the entire set $\{m\}$ was still valid. If there were only 2 remaining monitor detectors in a run and one was selected for removal, then the entire run was removed from the data set since there was no way to confirm the validity of the one remaining monitor and since it would seem that something was drastically wrong with that run. This was very rare.

Once all outliers were tossed, then the final values of the $\bar{q}_{j,\{s\}}$'s, which then only reflected runs where no detectors were removed, were used as the normalization values for the M_{ij}'s for all runs. The final single value $\bar{M}_i$ obtained as the monitor yield for the i'th run is finally given as follows:

$$\bar{M}_i = \frac{1}{n_s} \sum_{j \in \{s\}} \frac{M_{ij}}{\bar{q}_{j,\{s\}}}, \tag{3.21}$$

where $n_s = 4$.

Once the normalized monitor yields were constructed, they were used to divide the yields from the rotating detectors. This divides out all beam current and target thickness dependence and leaves only a dependence on the differential cross sections of the reactions and an overall normalization attributable to solid angles and to the constant cross sections at the monitor angle. All data are converted to the center-of-mass frame. The triton angles are then converted to their corresponding proton

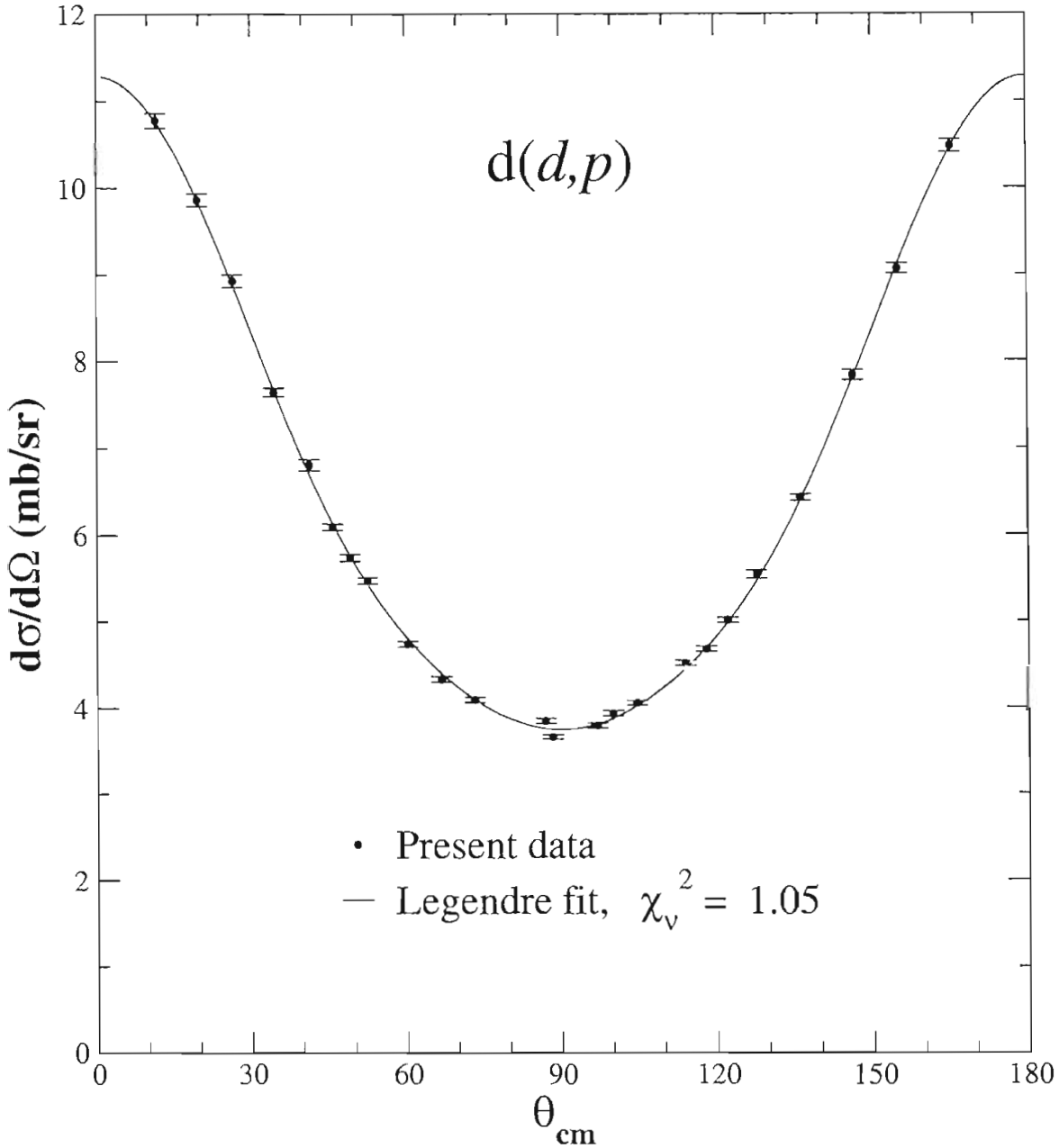

Figure 3.3: Angular distribution of $d(d,p)t$ differential cross section at $E_d = 660$ keV: The data points shown are the weighted means of all data runs at the same angle. The curve is a fit of even order Legendre polynomials up to P_4.

angle so that they can be shown on the same plot as the protons. Because of the symmetry around 90° in the center of mass, leaving the triton data at its original angle would produce identical angular distribution fits and total cross sections. Still, for conceptual accuracy, the proton angles are used. Figure 3.3 shows the results from the angular distribution measurement of $d(d,p)t$ at $E_d = 660$ keV with a fit to even-order Legendre polynomials in center-of-mass angle. The results were normalized using the data shown in Figure 3.2 along with the appropriate reaction data as explained previously in Section 3.2.1. I intentionally neglected to mention above how rotating detectors were normalized to each other to correct for solid-angle variations. For Figure 3.3 the results of the relative solid-angle measurements described previously in Section 2.3 were used. The normalization was handled differently for the final analysis as will be described in Section 3.4.

3.3 Low Energy Normalizations

Once normalized angular distributions were derived at the E_d=480 keV, the energy cross-normalization data could be used to normalize the low energy angular distributions at fixed points. For this process several detectors were used. However all of the reaction detectors served the same purpose but at different angles, so again for simplicity I will consider just one reaction detector R. Only the $d(d,p)t$ and $d(d,n)^3$He reaction peaks were useable for the cross-normalizations. The same center-of-mass conversion issues existed as those discussed in Section 3.2.2 for the angular distribution data. The reaction yields in R were normalized only to the gold elastic-scattering yields in the Rutherford monitor, again labeled detector C, and to the appropriate Rutherford cross section. The normalized yield α^x is defined as

$$\alpha^x = \frac{N^d_{d(d,p)t}}{N^d_{Au(d,d)}} \sigma_{Au(d,d)}(E^d, \theta_C) \,. \tag{3.22}$$

Physically, from Equation 3.3, this ratio corresponds to the following:

$$\alpha^x = \frac{\Delta\Omega_R}{\Delta\Omega_C}\frac{t_d}{t_g}\sigma_{d(d,p)t}(E^d, \theta_B)\,, \tag{3.23}$$

using the same notation as in previous sections.

If this ratio is calculated for data taken at two deuteron energies, 480 keV, and for example, 120 keV, using the same target, then we find

$$\frac{\alpha^x(\mathrm{E_d} = 120\ \mathrm{keV})}{\alpha^x(\mathrm{E_d} = 480\ \mathrm{keV})} = \frac{\sigma_{ddp}(\mathrm{E_d} = 120\ \mathrm{keV}, \theta)}{\sigma_{ddp}(\mathrm{E_d} = 480\ \mathrm{keV}, \theta)}\,, \tag{3.24}$$

and the solution for the differential cross section at 120 keV is then trivial. To measure the $d(d,{}^3\mathrm{He})n$ reaction cross sections at the low energies, I only needed to use the enormous number of counts in the angular distribution data at angles where ^{3}He yields are directly compared to the proton and triton yields in the same detector. Because of the very large body of data existing for this purpose, this adds no significant uncertainty. To put the issue in a more straightforward perspective, really the $d(d,n)^3$He and $d(d,p)t$ angular distribution data have the same normalization in the lab frame since they are acquired with the same conditions. There is truly only one normalization to determine and it can be found using either of the reactions or both. For the low energy data we did not have the luxury of using both.

3.4 The Whole Enchilada: Integrated cross-section analysis

For the final analysis I chose a method using more fitting and less algebra than the methods discussed above. Solutions were found for both the $d(d,p)t$ and $d(d,n)^3$He cross sections at all energies simultaneously using all available data. Before describing this process I will discuss the issue of data correlations, one of the main motivations for using such a procedure.

3.4.1 Correlations

With the procedures of Section 3.2 alone, it becomes very difficult to include data from all detectors in the normalization process and account for the correlations involved. In describing the normalization analysis in Section 3.2.1, I ignored the fact that p-d elastic data and the reaction data exist for two detector sets at two different angles. In order for solid angles to vanish, the same detector set must be used for the reaction data as for the proton elastic-scattering data. This essentially produces two separate measurements. This alone complicates things. The fit to the angular distribution data does not produce values as a function of angle; it produces Legendre coefficients and errors in those Legendre coefficients. These errors should be largely uncorrelated since Legendre polynomials are orthogonal. These can then be used to produce values at certain angles and those values can be normalized to the normalization data. However, the values derived for those certain angles are no longer orthogonal parameters and their uncertainties are highly correlated. Thus the two normalizations at different angles cannot simply be applied independently and their errors added in quadrature in the usual way as the for uncorrelated data. Instead a correlation term would have to be added. This can be done but is certainly a nuisance.

The situation is actually a little more complicated than described above. The two normalization points do not represent entirely independent measurements even before applying them to the angular distributions. Some of the uncertainty in each is contributed from the uncertainties in the d-d elastic beam-switching data. Since there was only one detector for these data, normalizations from both detector sets used the same data for this part of the measurement. The different normalization points are partially but not completely correlated. The d-d elastic-scattering yields measured during the reaction runs in the normalization procedure do not not contribute significantly to the overall statistical uncertainties because of the large number of counts obtained for these peaks. For this reason these data do not introduce a significant correlation. This fact will be important later in this section.

The correlations described above are correlations in the inputs ultimately used to calculate a single result and thus make it difficult to calculate the error in that result. We are also interested in calculating multiple related results, specifically cross-sections for different reactions and different energies. Some types of correlations will cause the results themselves to have uncertainties which are correlated to each other. This type of correlation does not make it more difficult to determine the error in any one result by itself, but it does make it more difficult to use the results in future calculations if these results enter as inputs to calculate a single value.

For example, if these cross sections are used in a Big-Bang network calculation to determine the primordial abundance of deuterium, then if the uncertainties in the cross-sections for the different reactions and/or the different energies are correlated, and if data for multiple energies and reactions are required in the calculation, then the error correlation terms must somehow be propagated into the calculation of the error in the deuterium abundance. This can be quite significant and cannot be accomplished if we do not have a way to quantify the correlations in these uncertainties. In our case, strong correlations in energy exist because the low energy data were normalized directly to high energy data. Correlations between cross sections for the two different reactions occur because these different reactions were normalized to the same data. The low energy $d(d,n)^3$He results are actually almost completely correlated to high energy $d(d,p)t$ results. These types of correlations, especially those between the different reactions, are indeed particularly important for applications in Big-Bang Nucleosynthesis. Thus information regarding the correlations is desired [Bur03].

Keeping track of all of these correlations in a traditional algebraic solution would be quite an ugly and tedious exercise in first-order error propagation. Algebraic results also suffer from the fact that for a given set of data there may be more than one algebraic way to solve for particular result using different combinations of data. Probably no one would be intrepid enough actually to incorporate multiple algebraic methods except possibly as a demonstration of cross checks. Using multiple methods for the purpose of reducing the error bars only adds large numbers of correlations that

I am disinclined to tackle directly. These multiple routes to the same answer often use some of the same information but also some different information. Added information always improves statistics if it is handled properly. Algebraic approaches cannot easily take advantage of this extra information.

3.4.2 The Fit

All of these problems and shortcomings can be addressed in one step. Take all unknowns, including cross sections for both reactions at all energies as well as experimental parameters, such as integrated beam flux, target thicknesses, etc., and fit them to the raw yields. This will determine uncertainties for all parameters using all data directly or indirectly relevant to a particular yield and will allow the correlations in the uncertainties of the results all to be found as explained in Section 3.1.

The basic idea of the fit, as with any fit, is to produce a model of how all data are produced and to vary the parameters of the model to reproduce the results. Most data are in some way related to one of the cross sections or we would not be measuring them. Thus the core of the fit, and the part in which we are ultimately interested, must be a parameterization of the differential cross sections for the $d(d,p)t$ and $d(d,n)^3$He reactions as a function of angle and energy. I will discuss the details shortly, but for right now it is enough to know that this part of the overall parameterization exists and that constraining it is our ultimate goal.

Data of various types can be described by this core parameterization along with various physical parameters specific to a given data type. These parameters primarily represent combinations of target thicknesses and solid angles. Some data constrain only these intermediate parameters and are not directly related to the central cross-section parameterization. As discussed at the beginning of the chapter, it is not reasonable, or helpful to include some parameters such as integrated beam flux in the fit and thus some compromise between algebra and fitting was used.

After some preparation to remove algebraically the parameters that I did not want to fit, the different data types for both reactions and all energies were rolled up in

one big master data file to be used as an input to the fit. The data entries had fields for energy, angle, value, and uncertainty. They also had various tags to indicate what type of data they represented. Based on those tags, an appropriate comparison was made to the parameterization, producing one term in the χ^2 sum for every data point. The value of χ^2 was calculated in the usual way:

$$\chi^2 = \sum_t \sum_i \left(\frac{y_{ti} - f_t(\{p\})}{\varsigma_{y_{ti}}} \right)^2 , \tag{3.25}$$

where y_{ti} is the value of the i'th data point of data type t. The value $\varsigma_{y_{ti}}$ is the one-σ uncertainty in y_{ti}, and $f_t(\{p\}, \theta_{ti}, E_{ti})$ is a function required to describe data of type t, and is in general a function of the set of all fit parameters $\{p\}$ and of an angle θ_{ti} and energy E_{ti} associated with the i'th data point via the data tags described above. However, for a particular t, $f_t(\{p\}, \theta_{ti}, E_{ti})$ depends on an appropriate subset of these function arguments. An appropriate function f_t was constructed to describe every data type. Values for the function parameters were then found which minimized the value of χ^2. In this way the parameters were constrained to their physical values, the values most consistent with the observables.

I will go through each data type and explain the preparation of the data set and the function $f_t(\{p\}, \theta_{ti}, E_{ti})$ used to compare each data type to the parameterization. I will introduce all the fit parameters as needed to do this. The details of the parameterization should not obscure the simplicity of the overall process which is ultimately just the minimization of the χ^2 sum.

Starting with the angular distribution data, the yields in the data file were the monitor-normalized yields discussed in Section 3.2.2. The only difference here was that the rotating detector yields were not normalized for relative solid angle. Instead a detector normalization parameter D was included in the fit. This slightly reduced the statistical power of the data but avoided systematic problems arising from inconsistent peak shapes during the solid angle normalization measurements. It is a worthy trade-off to gain systematic certainty at the expense of statistical certainty. The data

were compared to the fit simply by multiplying this solid angle parameter by the value returned from the cross-section parameterization for the angle and energy of the given data point. The function $f_{jk}(\{p\}, \theta_i, E_i)$ for angular distribution data for the j'th detector and k'th reaction was then

$$f_{jk}(\{p\}, E, \theta) = \sigma_k(E, \theta) D_j \,. \tag{3.26}$$

As well as having absolute normalization data for both the $d(d,p)$ and $d(d,{}^3\mathrm{He})$ reactions, the ratio of the normalizations for the two reactions are constrained by the angular distribution data. Since both reactions were measured simultaneously for many energies and lab angles, there are a very large number of counts directly relating the normalizations of the two distributions. This is an example of having multiple ways to constrain the same information, an ideal situation for using fits.

Although I have not mentioned it, this constraint between the normalizations of the two reactions has already been automatically accounted for in the fit without the need to address the issue explicitly. The same solid angle normalizations were used to parameterize both reactions since they were collected in the same detectors. If we calculate the ratio of Equation 3.26 for the two reactions, call them $k = 1$ and $k = 2$, the following is obtained:

$$\frac{f_{j1}(\{p\}, E, \theta)}{f_{j2}(\{p\}, E, \theta)} = \frac{\sigma_1(E, \theta)}{\sigma_2(E, \theta)} \,, \tag{3.27}$$

and there are no auxiliary parameters connecting the ratios of the two cross-section parameterizations to the ratios of the functions f. The individual terms in χ^2 corresponding to the angular distribution data will favor a minimization solution in which the functions f are constrained to be within the uncertainties in the yields for the corresponding reactions. Thus Equation 3.27 dictates that these terms favor ratios of the solid angle parameterizations which are equal to the ratios of the yields for

the two reactions within the uncertainties given by the data. Again I want to point out that this constraint came as an automatic result of a physically accurate parameterization. Many such interconnections in the data are addressed in similar fashion. Using algebraic techniques, these connections would need to be explicitly checked or incorporated, or just ignored. When fits use realistic physical parameters, much of the burden of understanding and accounting for details of the relationships in the data is relieved, seemingly magically.

By dividing the data by the monitor yields before fitting, the dependence on integrated beam flux times target thickness, parameters which change with every run, has been removed. As computers have become faster, it may now be possible to include these parameters in a desktop analysis. This would produce a parameterization with many hundreds of parameters, which sounds impossible even for a top-of-the-line computer; however, all of these extra parameters would be fit to the monitor detectors for a particular data run and would be very uncorrelated, possibly yielding only slightly more than a linear increase in the computer time needed. It is, however, also this lack of correlation that allows these parameters to be safely left out of the fit.

The actual details of the solid angle normalization parameterization were rather complicated. In order to incorporate data that came from only one of the two detectors in a pair, a tag in the data file labeled the side that each data point came from: either left, right, or sum. Furthermore, the normalization is not only attributable to the solid angles (or to be technically correct, the ratio of the solid angles to the renormalized monitor solid angles), but also to the cross sections for the reactions in the monitor detectors. Since these cross sections change with energy, the detector normalizations also had to change with energy. This change does not affect the relative normalizations of the left and right sides though, only the overall normalization of the two. For this reason, and to improve the behavior of the minimization, the parameterization actually included an overall normalization parameter and relative normalization parameters for the sides. The two parameters were multiplied together to obtain the total normalization D for a particular detector. The parameter for one side was fixed

and set to a value of 1 to prevent over-parameterizing the normalizations. A data tag distinguished new energies so that a new overall normalization parameter would be used, but allowing the information about the relative normalization to be kept. In this way, all statistics available helped to determine the relative solid angle normalizations.

Further complicating the situation, not all data were taken with exactly the same experimental setup. For various reasons, between some experiments the detector arrangement was reconfigured and later restored. It was not possible to guarantee the solid angles would be exactly the same when returning to the standard angular distribution setup. Yet another data tag was introduced to label the different setups. Data for different setups were compared to the core parameterization using completely different sets of detector normalization parameters, both overall and relative.

Up to this point the cross-section parameterization has been fit to the angular distribution data via detector normalization parameters. This constrains the shape of the cross sections given by the parameterization to match the shape of the cross sections given by the data. The normalization data are of course still needed to constrain the normalization parameters. The normalization data in the data file were exactly the values for α^p, α^d, and α^r as defined by equations 3.11 through 3.13. For α^p and α^r, labels were set to distinguish which detector was used to collect the data. The three α's together define the cross section at a single angle and energy as shown by Equation 3.14. Since there is already a parameterization of the cross section itself, only two more parameters are needed to describe these α data. The two parameters which I will call u and v physically correspond to the following:

$$u = \alpha^d \tag{3.28}$$

$$v = \frac{\alpha^p}{\alpha^d} \tag{3.29}$$

The choice to write v as a ratio of α^p to α^d instead of simply as α^p was largely arbitrary but should improve the behavior of the χ^2 minimization somewhat by removing parameter correlations. Parameter v was actually split into two parameters, v_j, where

j designates which of the two normalization detector pairs will be related to the parameter. Recall that the proton scattering and the reactions must be measured in the same detector pair, but that two separate pairs existed for this task. For every target and energy, a separate set of the parameters v_j and u were generated. As always, tags were included with each data point to label all necessary properties of the data for determining how to compare them to these parameters and which parameters to use. I will explain the comparisons ignoring the different targets and energies which only add complication. Although these parameters were designed to represent the physical expressions above, all parameters are ultimately defined only by how they are used in the fit functions f.

Data points of type α^d were compared directly to the parameter u by defining

$$f_{\alpha^d} = u\,. \tag{3.30}$$

For data points of type α^p_j, where j again represents the detector pair, the following fit function was used:

$$f_{\alpha^p_j} = v_j u\,, \tag{3.31}$$

which is a trivial solution to the physical definitions in Equations 3.28 and 3.29. Finally data points of type α^r_{jk}, where k corresponds to one of the two reactions, were compared to the parameterization using

$$f_{\alpha^r_{jk}}(E,\theta) = \sigma_k(E,\theta_j)v_j\,, \tag{3.32}$$

as dictated by substituting Equation 3.29 into 3.14 and solving for α^r.

The only things now left out of the explicit parameterization of the high energy data are the d-d elastic-scattering yields in the reaction normalization data runs, the α^r runs. These yields are accounted for in the re-parameterization of the α^r since

they were included in the value α^r itself, but since these yields are not explicitly parameterized, the fit cannot explore the error correlations arising from the sharing of d-d elastic-scattering data between multiple reaction detectors and normalizations of multiple reactions. This problem only relates to d-d elastic scattering for the reaction data runs and not to the d-d elastic-scattering beam-switching runs. This is acceptable because, as a result of the large number of counts obtained in this peak during several hours of collecting reaction data, this yield introduces very little uncertainty, and thus very little uncertainty correlation.

The last remaining type of experimental data is the set of data normalizing the high energy differential cross sections to the low energy differential cross sections. For this, the data sent to the input file were just the α^x's introduced in Section 3.3. I will call the parameter needed to connect the data to the cross-section parameterization simply w. From Equation 3.23, it is seen that for a particular target, α^x is proportional to the differential cross section. The needed parameter w is then just the proportionality constant:

$$w = \frac{\Delta\Omega_R}{\Delta\Omega_C}\frac{t_d}{t_g} \tag{3.33}$$

The ratio of solid angles is different for every detector and the ratio of target thicknesses is different for every target. Thus data from each j'th detector and k'th target is flagged and associated with a different w_{jk}. Since multiple targets were used over the course of normalizing the different energies, it would be possible to break the parameter w into two separate parameters, one for the solid angles and one for the target thicknesses. Somewhat similarly to the situation for the angular distribution solid angle normalizations, this would provide a separated overall normalization parameter which was target dependent, and a set of relative parameters which would remain fixed for all targets. For simplicity, the two were combined into the single parameter w with some, but not too significant, loss of statistical power. Combining parameters in this way adds no parameter correlations; it actually removes them because the data

used to constrain solid angles are now isolated to individual experiments on individual targets. The values for the relative solid angle parameters for different targets are of course related; they should be the same within the statistical uncertainties, but those uncertainties come from different data sets and are not correlated.

The proper parameter function with which to compare the α^x's is then just $f = \sigma(E,\theta)w$. The value of w is constrained by terms in the χ^2 sum comparing this function to data at an energy where the cross section is already constrained, 480 keV in particular. Further comparison of data from the same target and detector at a different energy, where the cross section was unknown, will constrain the cross section at that energy via the now-determined value of w. As mentioned before, the cross-normalization procedure was only performed for $d(d,p)t$. The $d(d,{}^3\mathrm{He})n$ cross sections at the low energies were constrained by the angular distribution data which relate the two cross sections as explained previously.

I have now explained how all data types are related either directly or indirectly to the cross-section parameterization. All that is left is to describe this core parameterization. As mentioned in Chapter 2, the $d(d,n)^3\mathrm{He}$ and $d(d,p)t$ differential cross sections can be described in the center-of-mass frame in terms of functions symmetric around 90°. The differential cross sections are generally described well by expansions in even Legendre polynomials $P_n(\theta)$ up to P_6 or less. Probably the simplest parameterization for the differential cross section as a function of energy is then to use Legendre polynomials with coefficients $a_{n,ik}$ for the n'th Legendre polynomial, the i'th energy and the k'th reaction. To improve the minimization behavior I will define the parameters $b_{n,ik}$ such that

$$b_{n,ik} = \frac{a_{n,ik}}{a_{0,ik}}\,. \tag{3.34}$$

The differential cross sections are then parameterized as

$$\boxed{\sigma_k(E_i, \theta_{cm}) = a_{0,ik} P_0(\theta_c m) + \sum_{m=1}^{M} b_{2m,ik} a_{0,ik} P_{2m}(\theta_{cm})} \,, \tag{3.35}$$

where $2M$ is the highest order of Legendre polynomial used. The integrated cross sections are then given by

$$\sigma_k(E_i) = 4\pi a_{0,ik} \,. \tag{3.36}$$

A parameterization of a cross-section function continuous in energy can be constructed instead by parameterizing each of the Legendre polynomials by a polynomial function of energy. The parameters are the coefficients of the n'th Legendre polynomial multiplied by the j'th power of energy for the k'th reaction . The coefficients for $n = 0$ are $c_{0,jk}$ and the coefficients for $n > 0$ are $c_{0,j} \times d_{n,jk}$. The resulting function for the differential cross section is

$$\sigma_k(E_{cm}, \theta_{cm}) = \sum_{j=0}^{J} c_{0,jk} E_{cm}^j + \sum_{j=0}^{J} \sum_{m=1}^{M} c_{0,jk} d_{2m,jk} E_{cm}^j P_{2m}(\theta_{cm}) \,, \tag{3.37}$$

where J is the maximum power of E in the energy expansion. The subscript cm denotes values in the center-of-mass reference frame. Note that $P_0 = 1$ for all angles and has thus been omitted from the above equation. It is also worth pointing out again that here j in E^j is an exponent, not a superscript label. I will refer to the first approach as the discrete parameterization and the latter as the continuous parameterization.

The continuous approach has many advantages over the discrete approach and even has advantages over a continuous fit in energy to the results of the discrete approach. Not only does the continuous parameterization directly smooth scatter in the total cross section over energy, but it also smooths scatter in the shape of the

differential cross sections over energy. Since these shapes determine how the angular distributions are normalized, this shape smoothing alone can improve the results in the total cross sections. Even if the coefficients of P_0 were parameterized using the discrete method and the coefficients of all other Legendre polynomials parameterized using the continuous method, some improvement in the total cross section results would still be made over the discrete method alone.

All cross sections at energies below 350 keV were normalized to the data at 480 keV. This makes it very important to use the best possible knowledge of the cross sections at 480 keV. If the results from the 480 keV data alone are used for this purpose then the error in all of the low energy normalizations would be systematically increased by the single point scatter in the 480 keV data. By simultaneously fitting all data, the best-fit value at 480 keV is effectively used instead. The best-fit value of the 480 keV data not only represents a reduction in the scatter of the high energy normalizations, but is also constrained by the requirement that the low energy data, normalized to 480 keV, form a smooth curve joining with the 390 keV data which was obtained using the high-energy normalization procedure. These data at 390 keV thus create somewhat of an overlap between the high energy points and the low energy points.

Possibly the most important advantage of the continuous fit, which is also related to the low energy normalizations, is the fact that corrections for small variations in energy in the data sets are handled naturally. This is primarily a concern with regard to the high energy data in the low-energy cross-normalization runs. Due to the differences in target thickness, the nominally 480 keV data used for energy cross normalizations were actually taken at a deuteron energy a few keV higher than the deuteron energy used to initially measure the nominally 480 keV cross sections. Refer to Section 2.5.1 and specifically Tables 2.1 and 2.2 for the exact details. In the discrete approach, no correction is made for these energy variations. However, in the continuous approach the precise energies of all data are used and no special treatment is needed to compare the parameterization to the data.

In an attempt to reduce the complexity of the energy dependence I actually parameterized a generalized form of the astrophysical S-factor, not the cross section, with the right hand side of Equation 3.37. If energy is given in units of keV, then the astrophysical S-factor $S(E)$ in units of keV·barns is related to the integrated cross section by

$$\sigma(E_{cm}) = \frac{1}{E_{cm}} e^{-31.29 Z_1 Z_2 (\frac{\mu}{E_{cm}})^{\frac{1}{2}}} S(E_{cm}) , \tag{3.38}$$

where Z_1 and Z_2 are the charges of the projectile and target, and μ is the reduced mass in amu. The value $\sigma(E_{cm})$ is just proportional to the 0'th Legendre term of the differential cross section. By applying the same energy dependent factor as in Equation 3.38, it is possible, although possibly unprecedented, to define a generalized S factor for all the higher order Legendre terms in the differential cross section. For d-d reactions my continuous parameterization for the differential cross section is then

$$\sigma_k(E_{cm}, \theta_{cm}) = \frac{1}{E_{cm}} e^{-31.29(\frac{1.00678}{E_{cm}})^{\frac{1}{2}}} \left(\sum_{j=0}^{J} c_{0,jk} E_{cm}^j + \sum_{j=0}^{J} \sum_{m=1}^{M} c_{0,jk} d_{2m,jk} E_{cm}^j P_{2m}(\theta_{cm}) \right) . \tag{3.39}$$

The θ-independent term in the right hand side of this equation is proportional to the conventional S-factor. The integrated cross sections as a function of energy are then given by

$$\sigma_k(E) = \frac{4\pi}{E_{cm}} e^{-31.29(\frac{1.00678}{E_{cm}})^{\frac{1}{2}}} \sum_{j=0}^{J} c_{0,jk} E_{cm}^j . \tag{3.40}$$

In practice this generalized S-factor parameterization did little to smooth the resulting cross-section functions. This indicates that the Coulomb barrier is not entirely responsible for the shape of $\sigma(E)$.

In Chapter 4, I will discuss results using both the discrete and continuous parameterizations.

3.5 Error Analysis

For the most part, the analysis of uncertainties in the results was straight-forward. The uncertainties for the normalized data input into the fits were calculated from basic first-order propagation of the uncertainties in the peak sums. Correlations arising from shared monitor normalization counts are not taken into account, but the monitor yields generally contribute a relatively small amount to the overall statistical uncertainties. The final uncertainties and correlations in the cross-section results were derived from the final fit using the error matrix elements corresponding to the cross-section parameters. I will explain this here in more detail and will discuss procedures taken to quantify data scatter and certain systematic errors.

3.5.1 The Matrix

For the discrete parameterization, the total cross section at each energy corresponds directly to one of the parameters to within a factor 4π. The 1σ uncertainty ς in the cross section is then simply the uncertainty in the corresponding parameter multiplied by the factor of 4π:

$$\varsigma(\sigma_k(E_i)) = 4\pi\varsigma(a_{0,ik})\,, \tag{3.41}$$

where $\varsigma(a_{0,ik})$ is given by the square root of the diagonal element of the covariant error matrix corresponding to the parameter $a_{0,ik}$. As in the end of the previous section, i represents one of the discrete energies where data were taken, and k represents either of the two reactions, $d(d,p)t$, or $d(d,n)^3\mathrm{He}$.

For the continuous case it is slightly more difficult to obtain the uncertainty at a given energy because multiple parameters are involved in the calculation of the cross

section as seen in Equation 3.40. Uncertainties in parameter values can be propagated in the same way as uncertainties in any data. For any function $g(\{p\})$ of the set of parameters $\{p\}$, the error in $g(\{p\})$ is

$$\varsigma(\, g(\{p\})\,)^2 = \sum_m \left(\varsigma(p_m)\frac{\partial g}{\partial p_m}\right)^2 + 2\sum_m \sum_n \left(\nu(p_m, p_n)\frac{\partial g}{\partial p_m}\frac{\partial g}{\partial p_n}\right) , \tag{3.42}$$

where $\nu(p_m, p_n)$ is the covariance of the parameters p_m and p_n and is exactly the off-diagonal element C_{mn} of the covariance matrix, or error matrix, C which is given by MINUIT. Likewise $\varsigma(p_m)^2$ is the variance of parameter p_m and is exactly the diagonal element C_{mm} of the error matrix. Since the matrix C is symmetric, Equation 3.42 can simply be written as

$$\varsigma(\, g(\{p\})\,)^2 = \sum_m \sum_n C_{mn}\frac{\partial g}{\partial p_m}\frac{\partial g}{\partial p_n} . \tag{3.43}$$

For the case of our cross-section parameterizations, all of the parameters are simply coefficients of terms in a sum, so the needed derivatives are just the respective terms with the coefficients set to 1. The uncertainty in the left-hand side of Equation 3.40 is given by

$$\varsigma(\sigma(E))^2 = \left(\frac{4\pi}{E_{cm}}\right)^2 e^{-62.58(\frac{1.00678}{E_{cm}})^{\frac{1}{2}}} \sum_{m=0}^{J}\sum_{n=0}^{J} C_{mn} E_{cm}^{m} E_{cm}^{n} . \tag{3.44}$$

Again the superscripts on E are exponents. For simplicity the reaction subscript has been omitted but this equation still applies to either reaction. Here, the matrix C is a sub-matrix of the full error matrix and only includes elements for the parameters representing coefficients of P_0. One may thus wonder how the uncertainties arising from correlations with other parameters are incorporated. However, as stated previously, the diagonals are already the full variances of a given parameter and already include effects from all parameter correlations. It is only when those effects must individually

and explicitly be accounted for that the off-diagonal terms are needed. In this case, this is fully governed, to first order, by Equation 3.42. Equation 3.44 was used with the continuous parameterization to calculate the uncertainties in the values of the integrated cross sections as a function of energy.

3.5.2 Quantifying Scatter

Unfortunately if χ^2 per degree of freedom, χ^2_ν, is not 1, then error matrix has little meaning and this whole issue is rather moot. Some amount of unaccounted-for scatter is expected in the data for various reasons. The normalizations are expected to have scatter representing the variations in target thicknesses observed. The ^{3}He angular distribution data have some scatter due to varying background conditions which are difficult to subtract out consistently, and possibly due to inconclusively blocked detectors which were not removed from the data set. Some minor but possibly non-zero underestimate in the uncertainties is expected because of neglecting the monitor correlations. The largest source of scatter in the data comes from fluctuations in the target thicknesses during beam-switching procedure. In the end χ^2_ν for the entire fit is just over 2 for the discrete fit and closer to 3 for the more restrictive continuous fit. It is then not sensible to trust the errors from the error matrix on face value.

I have implemented a procedure to address this issue by quantifying the scatter in the data and adding an appropriate amount of error. Effectively this is done by adding enough error to make χ^2 per datum equal to 1. This may seem like a rather brute-force fix to a problem and to some extent it is, but it is not without merit or precedence. For a simple fit, the easy way to fix χ^2_ν is to take the original value of the square root of χ^2_ν(I suppose I can just call that χ_ν), and divide all of the data uncertainties by it. This will make the new χ^2_ν exactly equal to one. This method has always seemed quite lacking to me. If there is indeed an unknown error that we are trying to account for, it is very unlikely that the unknown error is proportional to the known error(a bit of an oxymoron but a useful concept here). It is much more likely that it is constant and added in quadrature to the known error. Indeed it may not

be constant, but since we do not know, there is certainly no reason to suspect it is proportional to the known error. One can even take the philosophy that uncertainties are about what we know (or don't know). Then for every point we equally do not know how much error should be added to it, so the needed uncertainty is in fact equal in some sense for every point. There is no doubt that some will find this an amusing philosophy, but if ever we knew what the uncertainties were, they would not be called uncertainties. There is always some probability that they are wrong.

Adding a constant error has a great advantage. If the original uncertainties of the data points are not equal, then the data points with small uncertainties will be weighted more heavily in the original fit than ones with larger uncertainties. Effectively many points can become almost irrelevant in the fit. If the uncertainties which are accounted for are negligible compared to the missing uncertainty then it makes no sense to give any data more weight than any other data. This effectively just throws away data that are perfectly good within the true uncertainties of the experiment. By multiplying all the error bars by a constant, the weighting will remain exactly the same. The errors will be made large enough so that the variances become large enough on average to make χ^2_ν equal to one. The smaller variances might thus still be smaller than they should be and still incorrectly influence the error matrix, and the points with larger uncertainties will still have little affect on the fit and remain largely useless. By adding the unknown error in quadrature, all points are weighted based on this quadrature addition of the known error and the unknown error. If the unknown error is negligible, the original weightings will be maintained, but if the known errors are negligible compared to the added unknown error, then all points will be weighted the same.

The difficulty of this addition procedure is that there is no very simple algebraic way to calculate the extra uncertainty as there was for the multiplication procedure. I have constructed an iterative algorithm to handle this. The procedure is to first minimize the fit with the original error bars. Then the fit is left unchanged and some small amount of error is added in quadrature to all points. The value χ^2 per datum is

then recalculated. In further iterations the amount of added error is changed to obtain χ^2 per datum of 1. To do this, the change in χ^2 between iterations is compared to the change in the added error. A first order Taylor expansion of χ^2 per datum is used to guess the next value for the added error until the process is sufficiently converged.

In practice it does not make sense to add the same error to all data types so the data are broken up into individual data types, essentially any particular angular distribution, separated by reactions, and the separate normalization data types separated only by sequence. The value of χ^2 is calculated using the current fit but only for the data of interest and separate added error is associated with every group of data. After performing this whole process the weightings will have changed, so the best fit may change to reflect the new weightings. In practice one re-minimization is needed to find the new best fit and no further iterations of the procedure are needed to find sufficient convergence. The uncertainties added by the procedures are in agreement with the known sources of scatter outlined at the beginning of the section. I use χ^2 per datum for this procedure as opposed to χ^2_ν because it would be very unclear how to distribute the degrees of freedom to the different data sets and because the difference in the two is negligible. This results in a final overall value of χ^2_ν which is slightly larger than 1.

I did say this procedure has some precedent. The multiplication technique is not new, but truly this addition technique is a very well known process in disguise. In fact it is taught in most undergraduate physics lab courses. In these labs, the students often have no knowledge of the random uncertainties in a process and they measure them by repeating the process several times and calculating the standard deviation in the results. I have personally used the approach to measure correctly many physical constants of springs, projectiles and so on, to within or very near the calculated uncertainties. For the measurement of a single value where the known part of the uncertainty is zero, the addition algorithm I have described is almost exactly equivalent to this simple introductory lab procedure, with the only possible difference being my intentional neglect of the insignificant difference between χ^2 per datum and

χ^2_ν. The additive process is an improvement and a generalization where the known uncertainties are correctly distributed and the rest is then evenly distributed.

3.5.3 Angle Uncertainties

Some uncertainty in the final cross-section results can arise from imprecise knowledge of detector angles. Since all angles were determined to within a fraction of a degree, uncertainties of this type are relevant only for knowledge of the p-d elastic-scattering cross sections which were particularly sensitive to small changes in the angles of the detectors for which they were needed. However, it was not difficult to analyze the effects of the angle uncertainty on all of the data simultaneously. In order to do this, the entire analysis was performed using the results of the zero-crossing experiment discussed in Section 2.6. The analysis was then repeated using values for the zero-offsets which were systematically shifted by 0.10° toward 0° . The zero-offset for all detectors were thus decreased (the value was decreased, not necessarily the magnitude) by 0.10°. This change corresponds the magnitude of the upper limit on the angle uncertainties as discussed in Section 2.6. For both settings the results of the discrete parameterization were determined. The relative changes in the total cross-section values at each energy are shown in Table 3.1

The effects are smaller than may be expected by examining the slopes of the p-d cross sections. This is attributable to cancellations arising from the reverse nature of the dependence of the $d(p,p)$ and $d(p,d)$ cross sections as a function of lab angle. There are relatively large variations in the results seen in Table 3.1. Since the trends in the cross sections are monotonic in energy and angle, this may seem surprising. However, some noise may be introduced by differences in the constraints provided by the various angular distributions coupled with the different behaviors of the $d(p,p)$ and $d(p,d)$ cross sections which are measured at different center-of-mass angles.

Similar tests were performed by giving the left and right detectors shifts of opposite signs. In these tests the resulting changes in cross sections were generally at the 10^{-4} level. The values shown are truly upper limits on the magnitudes of the uncertainties

Nominal Energy (keV)	$\frac{\Delta\sigma_{d(d,p)t}}{\sigma_{d(d,p)t}}$	$\frac{\Delta\sigma_{d(d,n)^3\mathrm{He}}}{\sigma_{d(d,n)^3\mathrm{He}}}$
120	0.0022	0.0020
180	0.0022	0.0022
240	0.0022	0.0022
320	0.0022	0.0022
390	-0.0014	-0.0016
480	0.0022	0.0012
570	0.0022	0.0006
660	0.0004	0.0004

Table 3.1: Effects of angular uncertainties on cross-section results: Changes shown are for shifts forward in angle by 0.10° simultaneously for all detectors. This shift amount corresponds to the uncertainty in the angle determination for the p-d elastic-scattering detectors.

and not 1σ uncertainties. For any way in which the results are interpreted, the effects of angular uncertainties are clearly negligible.

3.5.4 Energy Uncertainties

I adopt a 1.5 keV uncertainty in the beam energy for all interactions in these experiments. This estimate includes the uncertainty in the beam energy and the in the energy loss corrections. Depending on the data set this may only be an approximately 1σ estimate for some data while it is closer to an upper limit for other data. I incorporate it into the error analysis as if it were a 1σ uncertainty.

In order to determine the effect of the energy uncertainty on the cross-section uncertainties I used the same technique employed for the analysis of the angular uncertainties. I perturbed all lab energies input into the analysis by +1.5 keV and recorded the change in the results of the discrete analysis. Such a shift assumes maximal correlation between energy uncertainties and is thus a worst case assumption. The results of this analysis are shown in Table 3.2.

Nominal Energy (keV)	$\frac{\Delta\sigma_{d(d,p)t}}{\sigma_{d(d,p)t}}$	$\frac{\Delta\sigma_{d(d,n)^3\mathrm{He}}}{\sigma_{d(d,n)^3\mathrm{He}}}$
120	0.0024	0.0025
180	0.0015	0.0015
240	0.0010	0.0010
320	0.0071	0.0072
390	0.0051	0.0051
480	0.0036	0.0037
570	0.0023	0.0026
660	0.0018	0.0020

Table 3.2: Effects of energy uncertainties on cross-section results: Changes shown are for shifts higher in lab energy by 1.5 keV for all data. This shift amount corresponds to the total uncertainty in the interaction energies.

The effects of the energy uncertainties are not negligible at the lower energies. For this reason it is desirable to find a way to incorporate these uncertainties into the main uncertainty analysis and thus into the error matrix. This can be done by introducing an energy shift parameter, s in the fit and including a single term in the χ^2 sum equal to $(\frac{s}{1.5keV})^2$ constraining s to be near 0, where near is defined by the value of 1.5 keV given to the uncertainty in the denominator. In general a separate energy shift parameter should be considered for the Mini-Tandem accelerator and for the High-Voltage Chamber(even that is an oversimplification), but we performed peak position tests which verified the consistency of the two within a fraction of a keV. Still, I did tabulate uncertainties for such combinations of shifts and the dominant uncertainties were very similar to those in Table 3.2 with the largest uncertainties at the lowest energies where only the Mini-Tandem was used.

It was impractical to directly model the complete effect the energy shift would have on the data. This is because effects such as center of mass angle conversions were handled in the initial monitor-normalization stage of the analysis and not in the fit parameterization. However, these angular effects are relatively small. I arrived at

a procedure to incorporate into the fit the full effect of the uncertainties as calculated in Table 3.2 without explicitly parameterizing all of the angular dependences. The procedure was to re-normalize the normalization data (specifically the reaction normalization data as opposed to the elastic-scattering data, but the choice was somewhat arbitrary and equally irrelevant) by an amount determined by the value of the energy shift parameter s. The trick here is determining the relationship between the energy shift parameter s and the proper renormalization factor for a particular energy. This is exactly the information contained in Table 3.2. Parameterizations of all reaction normalization data were thus renormalized by $(1 + sd(E))$ where $d(E)$ is the value of $\frac{\Delta\sigma}{\sigma}$ in Table 3.2 for the energy E. The effect was to give the result at each energy an added perturbative freedom with the perturbation being proportional to the tabulated uncertainties.

Since energy-related modifications to the shapes of the angular distributions are not parameterized, this procedure does not improve any excess in χ^2 arising from energy-related inaccuracies in center-of-mass angle conversions. However, the effect (if not completely negligible) that these energy-related angle uncertainties have on the overall normalization is accounted for. These effects were included in the values in Table 3.2 since, in generating that table, the complete analysis was recalculated including center-of-mass angle conversions performed in the monitor-normalization stage. The increase in the uncertainties calculated by this fitting procedure are in excellent agreement with quadrature addition of the tabulated energy-related uncertainties with the uncertainties generated by the fit before applying this modification. The advantage of this fitting procedure is that the information about these uncertainties and the correlations between them can now be neatly contained in the error matrix in a manner consistent with other uncertainties analyzed in the present work.

3.5.5 Counting Our Gold: Uncertainties in the fit

Some uncertainty was associated with fitting the gold monitor peak for the energy cross normalizations, especially at the lowest energy. As the beam energy was reduced,

the channel separation was reduced between the gold backscattering peak and the carbon backscattering peak. At all deuteron energies down to 180 keV this was not a serious problem and the two peaks could be sufficiently resolved by peak fitting. However at 120 keV there were minor problems. A fit with a reduced χ^2 of just over 1 could be obtained using two Gaussian functions and a linear background. Only the gold peak and a small portion of the neighboring carbon peak were fit. Considering the peaks typically had over 2 million counts at this energy, this is a seemingly impressive fit. The problem was that the fit was not unique. A fit of equal or even slightly better χ^2 could be obtained by adding an exponential background to all the other functions used in the fit. This is not surprising since with that much data more parameters will almost certainly reduce χ^2 at least slightly. The issue is that the two fits produced significantly different values for peak area. This is still not bad in general. For instance, I could put two Gaussian functions instead of one under the peak, calling the other a "background" and this would simply be a wrong parameterization which could produce very wrong answers for the one Gaussian function considered as the peak. However, the added exponential describes the side of the neighboring carbon elastic-scattering peak and describes a somewhat reasonable background function. Since we do not know exactly what the background should be then, this ambiguity is a real issue. The difference in results from the two fits was about 3%.

This needed to be addressed in two ways: the first was to find the best adopted value for the peak area; the second was to associate an error with that area and incorporate that error into the final results. Regarding the first task, to determine the best adopted background I tried to gain some understanding of the true shapes of the peaks and the backgrounds. Looking at spectra at higher energies with the same amplifier gains, it was clear that electronic noise existed below channel number 120. This electronic background, arising primarily from thermal noise, can often be fit well by an exponential function and may be the reason for the slightly improved χ^2 with the exponential background. However, as seen in Figure 3.4, when the exponential is used it essentially replaces the second Gaussian which would otherwise describe the

carbon elastic peak. This may not be entirely suitable, but it is difficult to know for sure.

I found a method of fitting which largely avoided the background issue. At both 480 keV and 320 keV I could fit just part of the peak excluding the left-most portion and obtain a similar result for the area parameter as for fitting the entire peak. At these energies, the difference was less than 0.5%. By leaving out the low-energy tail of the Au peak, the largest part of the background at 120 keV could be avoided. Interestingly enough the results using this method, either with or without an exponential term, were consistent with the complete fit using no exponential background and were inconsistent with the complete fit using an exponential background.

The actual procedure was to fit the peak once to determine its centroid c and standard deviation σ. The peak was then fit again but calculating χ^2 only for channels greater than $c - \frac{1}{3}\sigma$. At 120 keV, this lower limit was in fact above channel 120, the noise cutoff. For consistency, all gold elastic scattering peaks for energy cross normalizations at all energies were fit using this algorithm. The fit function used was the combination of two Gaussian functions and the linear background, although as mentioned, with this procedure inclusion of the exponential component made little difference. For the 480 keV data the elastic peaks were sufficiently separated that the gold peak could be fit entirely by itself. For this reason only one Gaussian was used at this energy.

Some effort was made to account for the possible error associated with this fit ambiguity. As mentioned before in this section, monitor correlations have not generally been accounted for because of their small statistical uncertainty. Now, with a 3% uncertainty this rationale is no longer valid. Gold peaks for all runs at a given energy will all be off in the same way, and the error will be the same for all peaks which are normalized to these gold yields. It is thus a somewhat systematic, or at least widely correlated, uncertainty that cannot simply be added into the statistical uncertainty of the gold peak area. Instead I have added a parameter to the fit which is multiplied by the parameter w described previously for low energy normalizations. It is only

multiplied for the low energy runs and not for the 480 keV runs. The parameter serves no purpose except to allow a small rescaling of the data. Without some restriction, the parameter would over-parameterize the fit and cause the result to be undefined. The parameter should be restricted to a variation equal to the uncertainty generated by the gold fitting. To do this I have included one extra data point in the data file with a value of 1.0 and an appropriate uncertainty. This new point is compared directly to the new parameter in the χ^2 fit by making the function f (defined in Equation 3.25) equal to the parameter value and thus restricting the parameter value to be near the data point value of 1.0. One such point and parameter is actually included for all of the low energies. The error assigned to the data point is set to 0.03 for the 120 keV parameter and to 0.01 for all others. Some small fit ambiguity was detectable at higher energies. A value of 1% is a generous upper limit.

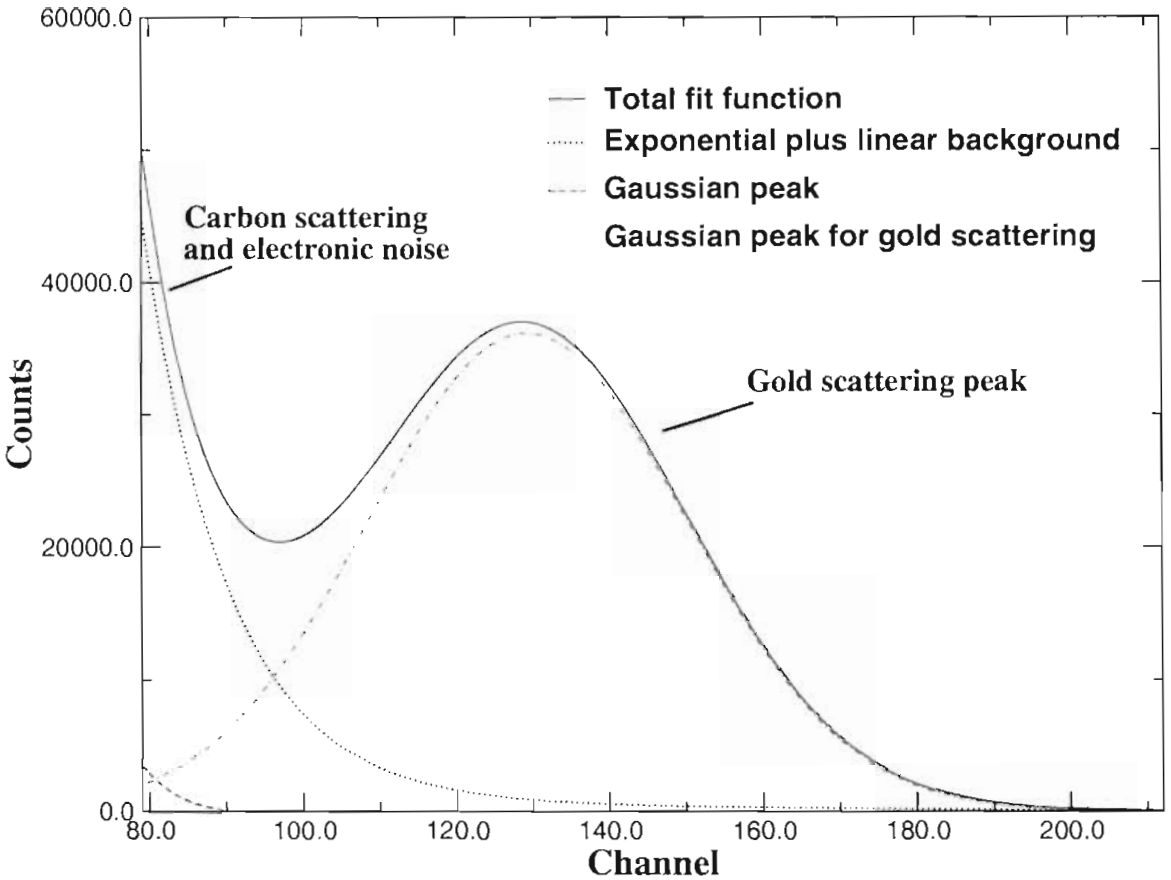

Figure 3.4: An alternate fit to a spectrum from deuteron beam backscattered from gold and carbon at $E_d = 120$ keV: The spectrum is nearly indistinguishable from the fit and is not shown. The fit includes an exponential plus linear background term and two Gaussian peaks. In this parameterization the carbon scattering and noise at low channel numbers can be almost completely described by the exponential with only a small Gaussian peak component. The fit used in the final analysis did not include the exponential term.

Chapter 4

Results

All of the experimental methods, analysis techniques, and error analyses have been discussed in detail in previous chapters. In this short but important chapter I will get to the good part and present the final numbers. The new data set will be compared to previous data and to commonly accepted compilations, especially the NACRE compilation [Ang99] which is becoming widely accepted as a standard in adopted values for cross sections of nuclear reactions of astrophysical significance. I examine the improvements in reaction uncertainties and the impact the data will have on the Big Bang Nucleosynthesis network calculations.

The cross-section results obtained from the discrete energy parameterization described in Equation 3.35 are shown in Figures 4.1 and 4.2, and Table 4.2. The errors shown are 1σ equivalents which include statistical uncertainties, fitting uncertainties from Section 3.5.3, energy uncertainties discussed in Section 3.5.4, and account for scatter in the data sets used to derive the total cross sections as explained in Section 3.5.2. The uncertainties are generally around the 2% level except at the lowest energy. At the lowest energy the uncertainty in the fit to the gold peak accounts for a 3% error which essentially adds in quadrature. The results at the lowest energies are also more sensitive to uncertainties in beam energy which contribute as much as 2.5% to the cross-section uncertainties.

Some scatter within the uncertainties is detectable, which is expected since our statistical and systematic errors are of comparable magnitudes. An overall scale error of 1% is estimated arising from uncertainties in the $p-d$ elastic-scattering cross section to which these data were normalized.

The lowest four data points are all normalized directly to the differential cross sections at 480 keV. For the discrete parameterization, they are normalized to the 480 keV data points and thus inherit all of the uncertainty of these points. This is not entirely fair as they should really be normalized to the best knowledge of the 480 keV differential cross sections which comes from a consistent fit of all the data. The representation is also mildly misleading in that uncertainty inherited from the 480 keV cross section is a systematic uncertainty that scales all four points equally. Simple error bars can never show the whole picture but these effects are in a first order approximation fully described by the error matrix.

The scatter is improved by the continuous two-dimensional parameterization of the differential cross-section defined in Equation 3.39. The results for the total cross section obtained from Equation 3.40 are given in Figures 4.1 and 4.2 along with the discrete results. The uncertainties shown are calculated from Equation 3.44. By comparing the continuous fits to the discrete fits it is visually evident that the continuous fits are correctly accounting for the known energy correlations. The continuous parameterization used in the previously mentioned figures are fifth order in the polynomial energy expansion and include up to P_6 in the angle expansion. The values of the coefficients of P_0 in Equation 3.39 are given in Table 4.3. There are five coefficients for each of the two reactions and the full 10x10 error matrix is shown for reference in Table 4.5.

I have had the question posed to me of just what exactly is one to do with all of these numbers in this error matrix, the continuous fit error matrix for example. I have already provided the first example of how to use the error matrix in Section 3.5.1. In that section I demonstrated how to calculate the uncertainties in the total cross section as a function of energy using the error matrix. The total cross section at a

given energy is a function of a subset of the parameterization, the same subset for which I have given the error matrix elements. In demonstrating how to calculate the uncertainty in the total cross section at a particular energy, I have shown how to calculate the uncertainty in any function of these parameters. Now, any function of the cross sections, even if it is a function of multiple cross sections having correlated uncertainties, can also be written as a function of the same subset of the parameters used to calculate the cross sections. Thus the uncertainty in that function, including effects of correlations between reactions and energies, can be calculated in the same way as the uncertainties in the cross sections themselves.

Dots on a page are not terribly exciting by themselves. The one thing still left to say is what all these data mean. The question really is: How do these numbers change things, specifically with regard to Big-Bang Nucleosynthesis? The answer may depend on who is presented with the question. There have been several published compilations and analyses of Big-Bang Nucleosynthesis data and network calculations and a review of them could fill a thesis on its own. Most, including references [Cuo03, Cyb03, Wal91], have focused a significant amount of attention on consistency with cosmological observables including primordial abundances and CMBR observations. Many, including some which have now acquired benchmark status, have used Monte Carlo techniques to analyze the relationship between the uncertainties in the reaction data to the uncertainties in the astrophysical constraints [Smi93, Kra90, Nol01]. The work of the latter produces sensitivity regions which inspired the present work. Finally there are even some works that have used traditional first-order error propagation to understand the effects of the data on network predictions. In particular Fiorentini *et al.* [Fio98] achieve impressively good agreement with the computationally expensive techniques used elsewhere and have the advantage of producing simple functional understandings of various uncertainty relationships via tabulated derivatives.

One data compilation in particular has gained significant popularity. This is the NACRE compilation [Ang99]. The NACRE compilation is designed to be a one-stop shop for reliable reaction-rate values for reactions with astrophysical significance.

NACRE does not address network calculations since it is intended as a broad resource for astrophysics in general. It has become the data source of choice for several BBN analyses [Cuo03, VF00, Coc01]

Since the NACRE compilation is designed as a source for reaction-rate data and not cross-section data, the adopted NACRE numbers cannot be compared directly to the data of the present work. The reaction rate is an integral of the total cross section weighted by a Maxwellian distribution and taken over all energies. For energies in MeV and cross sections in barns, the reaction rate $N_a \langle \sigma \nu \rangle$ in $cm^3 mol^{-1} s^{-1}$ is given by

$$N_a \langle \sigma \nu \rangle = 3.7313 \times 10^{10} \mu^{-1/2} T_9^{-3/2} \int_0^\infty \sigma E \, exp(-11.604 E/T_9) dE \,. \qquad (4.1)$$

For the integral to converge at temperatures relevant to BBN, $T_9 < 2$, the integral can be cut off at E_{cm} of about 2.5 MeV but not much lower. Thus to calculate reaction rates accurately I must include data at energies higher than those of the present work. However, data at these energies contribute significantly less to the integral at the relevant temperatures than the data of the present work. For this purpose and to make a fair judgment of how the new data compare to the NACRE compilation, I have used the same data at high energies as those used in NACRE compilation, the data of Schulte *et al.* [Sch72]. I have included the Schulte data up to $E_{cm} = 2.75\ MeV$ for both the $d(d,p)t$ and $d(d,n)^3$He reactions.

These data are included in the continuous parameterization by using the total cross sections to appropriately constrain the zero order Legendre coefficients at the high energies. The Schulte data have scatter which is significantly larger than their quoted statistical errors. To prevent this data set from unduly constraining the fit, I have multiplied their statistical uncertainties by 5, leaving the smallest uncertainties on these data still below one percent of the value. I have previously objected to this multiplication procedure, but it will suffice for the present purpose. The polynomial expansion of P_0 was expanded to 7th order to fit the large changes in curvature associated with the extra Schulte data. Reduced χ^2 was about the same as for the fit

to the present data alone. The results of these fits are shown in Figures 4.3 and 4.4. The $d(d,n)^3$He reaction curve does not follow the Schulte data impressively well. This is probably a limitation of the parameterization in representing changes in curvature over these large energy regions. It is not a significant problem for the purpose of constraining the tail of the reaction-rate integral, at least not for a rough comparison.

The NACRE compilation gives coefficients for a quadratic cross-section function which they used in calculating their rates for the $d(d,n)^3$He and $d(d,p)t$ reactions at "low energies". They do not specify exactly what is meant by low energies. I have used these cross-section functions for energies below the present work in order to complete the integrals. As was the case for the high energy Schulte data, this low energy data contributes only a small amount to the integral for temperatures significant to BBN.

Using these total cross-section curves I then calculated the reaction rates by computing the right hand side of Equation 4.1 with a high-energy cutoff on the integral at $E_{cm} = 2.5MeV$. The results are compared to the NACRE reactions rates in Figures 4.5 and 4.6. Judging by plots of abundances as a function of temperature for network calculations of Nollet and Burles [Nol01], all significant standard BBN nucleosynthesis occurs at temperatures near $T_9 = 1$. At this temperature the rates derived using the present work are about 8% high for $d(d,n)^3$He and about 9% high for $d(d,p)t$ as compared with the NACRE rates. These discrepancies are systematic, remaining at similar levels for a large range of temperatures.

It is important to emphasize that there is nothing inherently bad about disagreement between the present work and the NACRE compilation. The NACRE curves are derived from a limited set of data and in fact include no data between E_d = 325 keV and E_d = 2.0 MeV. Furthermore, the data of Krauss *et al.*. [Kra87] were the only data used in the NACRE compilation in the energy range of 250 to 325 keV, and although these are respectable data, they have uncertainties of about 10%. Refer back to Figure 1.2 for a plot of existing $d(d,n)^3$He data. The NACRE compilation incorporates all data in these plots with the exception of the Ganeev data. There was

indeed a limited amount of data available and our results will greatly contribute to the cross-section information available in this energy region.

Abundance	$\frac{\partial ln Y_i}{\partial ln R_{d(d,p)t}}$	$\frac{\partial ln Y_i}{\partial ln R_{d(d,n)^3He}}$
D/H	-0.46	-0.53
^{3}He/H	-0.26	0.18
^{4}He mass fraction	0.01	0.01
^{7}Li/H	0.06	0.69

Table 4.1: Logarithmic derivatives of abundances Y with respect to reaction rates R calculated from reference [Fio98].

Using the logarithmic derivatives tabulated in [Fio98], I can estimate the differences in primordial abundances calculated using our new data vs. using the NACRE compilation. These derivatives of abundances with respect to reaction rates are given in tables of coefficients of polynomial expansions in the baryon to photon ratio η. For my estimates I use a value of η of 6.14×10^{10} from reference [Cyb03] which was derived directly from an analysis of recent WMAP data performed in reference [Ben03]. The values of the logarithmic derivatives calculated for $\eta = 6.14 \times 10^{10}$ are given in Table 4.1.

Some conclusions can be drawn from Table 4.1. It is immediately evident that a roughly 8% change in the cross sections will have essentially no effect on the primordial abundance of ^{3}He. Since the uncertainties and present adjustments of the $d(d,n)^3$He and $d(d,p)t$ reaction rates are positively correlated, the relative signs of the derivatives for the two reactions in table 4.1 have important significance. Although the derivatives shown for the ^{4}He abundances are significant, the changes in the abundance induced by the changes in the two reactions nearly cancel and the net effect is small. However, because the two D/H derivatives have the same sign, multiplying the percent deviations between the present rates and NACRE rates by the logarithmic derivatives for the $d(d,n)^3$He and $d(d,p)t$ reactions and then adding the two results yields a change

in the deuterium abundance of roughly -8%. The change calculated for ^{7}Li/H is +6% which is almost entirely attributable to the changes in the $d(d,n)^3$He reaction rates.

By all accounts, the lithium abundance observations are currently in severe disagreement with the BBN results [Kir03]. This 6% increase in the predicted lithium abundance makes an unresolved problem slightly worse. Currently the ^{7}Li abundances predicted using CMBR values of η are at least a factor of 2 higher than the observed abundances [Cuo03]. This change is small compared with the uncertainties plaguing this comparison but it certainly does not improve the hopes of finding agreement between standard BBN and observed ^{7}Li abundances. We look at this not as a failure but as an opportunity to explore possibilities of non-standard Big Bang Models and thus new physics.

The current observational value of the primordial deuterium abundance, D/H = $2.78^{+0.44}_{-0.38}$ [Kir03], obtained from QSO absorption spectra, is in good agreement with predictions of BBN using η from the CMBR data, D/H = $2.56^{+0.35}_{-0.24}$ [Cuo03]. However, as more data have arrived, the statistical uncertainty estimates on the abundance observations have not held up; the uncertainty is now dominated by scatter in the data. The change which we predict in the BBN+CMBR D/H value will strain the current agreement slightly, but the results should still be well within the current mutual uncertainties. The reduced uncertainties of the $d(d,n)^3$He and $d(d,p)t$ cross-sections from the present work along with future improvements in the $d(p,\gamma)$ cross sections and more QSO observations, may soon provide significantly more stringent tests of this comparison, again yielding insight into the validity of the details of the standard BBN model.

Although other aspects of the BBN picture are still limiting the comparisons of theory and experiment to around the level of 10% or worse, our new data will pave the way for future developments in precision cosmology. As other measurements are improved, BBN predictions will become sensitive to many details of the model including inhomogeneities and neutrino properties. The new data should put to rest concerns and claims that the d-d reaction rates may be inaccurate and should ultimately result

in significant modifications to the reaction rates used for current astrophysical applications including BBN. The data verify the limited, not always trusted, and often overlooked data which previously existed in this region of energy [Gan58] and with roughly 2% uncertainties or better, they represent a significant improvement in precision which, along with improvements in other cross-sections, will translate directly into reduction in uncertainties of BBN predictions. These data will truly help to usher in the "new era" [Cyb03] of precision cosmology.

E_d	$\sigma_{d(d,p)t}$ (mb)	$\sigma_{d(d,n)^3He}$ (mb)
646.09	74.36 ± 0.97	83.99 ± 1.37
557.30	68.25 ± 0.96	80.41 ± 1.17
470.99	58.38 ± 0.76	69.49 ± 1.00
379.21	53.14 ± 0.90	62.56 ± 1.07
314.55	45.59 ± 1.10	55.90 ± 1.43
232.77	37.45 ± 0.79	42.82 ± 0.92
172.76	29.64 ± 0.87	33.34 ± 1.02
112.23	19.72 ± 0.85	20.86 ± 0.91

Table 4.2: Integrated cross-section results for discrete fit: The corresponding S-factor error matrix is given in Table 4.4. The 1σ uncertainties include statistical uncertainties from all parts of the present work as well as fitting uncertainties discussed in Section 3.5.

	$d(d,p)t$	$d(d,n)^3$He
$c_{0,0}$	5.3972 ± 0.46308E-01	6.0895 ± 0.59511E-01
$c_{0,1}$	0.11143E-01 ± 0.29677E-03	-.15568E-01 ± 0.63306E-03
$c_{0,2}$	-.44211E-04 ± 0.11380E-05	0.51142E-03 ± 0.29437E-05
$c_{0,3}$	0.37474E-06 ± 0.38516E-08	-.32612E-05 ± 0.10845E-07
$c_{0,4}$	-.63197E-09 ± 0.12201E-10	0.98326E-08 ± 0.34817E-10
$c_{0,5}$	0.24495E-12 ± 0.36702E-13	-.11078E-10 ± 0.94008E-13

Table 4.3: Coefficients for $S(E)/4\pi$ expanded in polynomials of center-of-mass energy. These are the $c_{0,j}$'s from Equation 3.40.

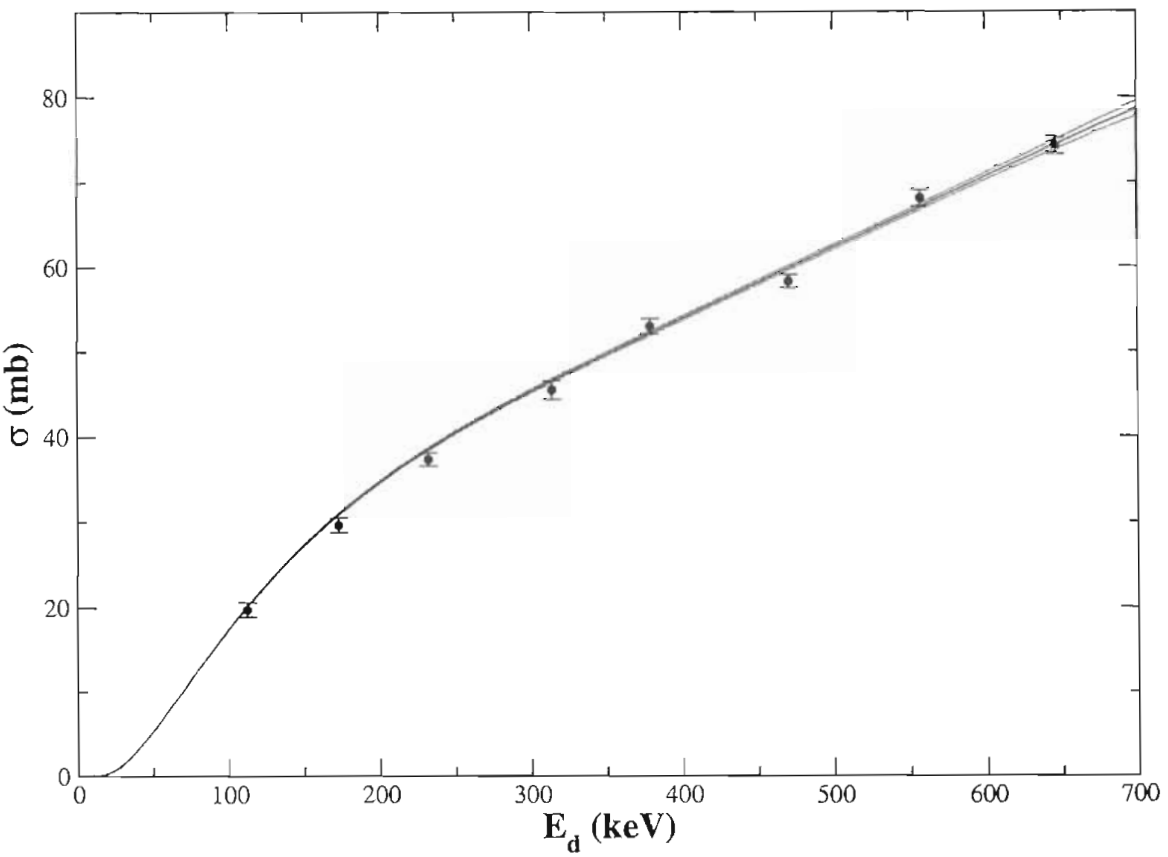

Figure 4.1: Integrated cross-section results for $d(d,p)t$: The points are the results from the discrete parameterization of Equation 3.35 and the curve is the result of the continuous parameterization of Equation 3.37. The error bars and error curves are 1σ uncertainties including statistical uncertainties, and fitting uncertainties. Details are discussed in Section 3.5.

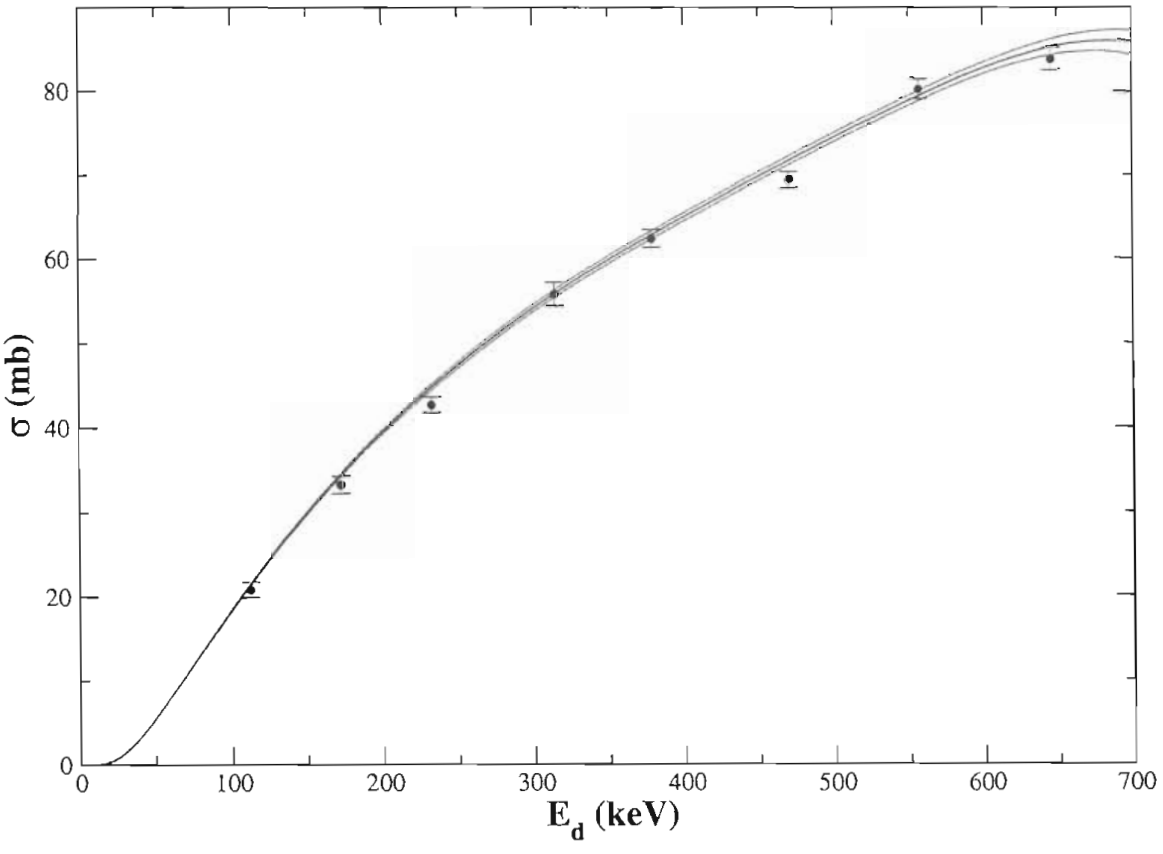

Figure 4.2: Integrated cross-section results for $d(d,n)^3$He: The points are the results from the discrete parameterization of Equation 3.35 and the curve is the result of the continuous parameterization of Equation 3.37. The error bars and error curves are 1σ uncertainties including statistical uncertainties, and fitting uncertainties. Details are discussed in Section 3.5.

	p E=646.09	p E=557.30	p E=470.99	p E=379.21	p E=314.55	p E=232.77	p E=172.76	p E112.23
p E646.09	0.23182E-01	0.62404E-04	0.39494E-08	-.29146E-11	0.32960E-08	0.40208E-08	0.45703E-08	0.82174E-08
p E557.30	0.62404E-04	0.19046E-01	0.38044E-09	0.32479E-10	0.29645E-09	0.39969E-09	0.45907E-09	0.28754E-09
p E470.99	0.39494E-08	0.38044E-09	0.11627E-01	0.25441E-05	0.96011E-02	0.87338E-02	0.80881E-02	0.78211E-02
p E379.21	-.29146E-11	0.32479E-10	0.25441E-05	0.15688E-01	-.39925E-05	-.19042E-05	0.67122E-06	0.73903E-06
p E314.55	0.32960E-08	0.29645E-09	0.96011E-02	-.39925E-05	0.25950E-01	0.73451E-02	0.67017E-02	0.64710E-02
p E232.77	0.40208E-08	0.39969E-09	0.87338E-02	-.19042E-05	0.73451E-02	0.14147E-01	0.60633E-02	0.58560E-02
p E172.76	0.45703E-08	0.45907E-09	0.80881E-02	0.67122E-06	0.67017E-02	0.60633E-02	0.22622E-01	0.55415E-02
p E112.23	0.82174E-08	0.28754E-09	0.78211E-02	0.73903E-06	0.64710E-02	0.58560E-02	0.55415E-02	0.41912E-01
n E646.09	0.25633E-01	0.10548E-03	0.55546E-08	-.40312E-11	0.46356E-08	0.56551E-08	0.64280E-08	0.11556E-07
n E557.30	0.89000E-04	0.22090E-01	0.47109E-09	0.38105E-10	0.36844E-09	0.49413E-09	0.56724E-09	0.38855E-09
n E470.99	0.44137E-08	0.44372E-09	0.12983E-01	0.27023E-05	0.10716E-01	0.97884E-02	0.89818E-02	0.86804E-02
n E379.21	-.81483E-11	0.45503E-10	-.60197E-05	0.16835E-01	-.11701E-04	0.62378E-05	-.38803E-05	-.38717E-05
n E314.55	0.40536E-08	0.38174E-09	0.11796E-01	-.64574E-05	0.30478E-01	0.90408E-02	0.82327E-02	0.79490E-02
n E232.77	0.46595E-08	0.46273E-09	0.10013E-01	0.35312E-05	0.84276E-02	0.16138E-01	0.69478E-02	0.67107E-02
n E172.76	0.52663E-08	0.51713E-09	0.90896E-02	0.74215E-06	0.75330E-02	0.68160E-02	0.25429E-01	0.62237E-02
n E112.23	0.86883E-08	0.26823E-09	0.81535E-02	0.45993E-06	0.67841E-02	0.61434E-02	0.57799E-02	0.43845E-01
	n E=646.09	n E=557.30	n E=470.99	n E=379.21	n E=314.55	n E=232.77	n E=172.76	n E112.23
p E646.09	0.25633E-01	0.89000E-04	0.44137E-08	-.81483E-11	0.40536E-08	0.46595E-08	0.52663E-08	0.86883E-08
p E557.30	0.10548E-03	0.22090E-01	0.44372E-09	0.45503E-10	0.38174E-09	0.46273E-09	0.51713E-09	0.26823E-09
p E470.99	0.55546E-08	0.47109E-09	0.12983E-01	-.60197E-05	0.11796E-01	0.10013E-01	0.90896E-02	0.81535E-02
p E379.21	-.40312E-11	0.38105E-10	0.27023E-05	0.16835E-01	-.64574E-05	0.35312E-05	0.74215E-06	0.45993E-06
p E314.55	0.46356E-08	0.36844E-09	0.10716E-01	-.11701E-04	0.30478E-01	0.84276E-02	0.75330E-02	0.67841E-02
p E232.77	0.56551E-08	0.49413E-09	0.97884E-02	0.62378E-05	0.90408E-02	0.16138E-01	0.68160E-02	0.61434E-02
p E172.76	0.64280E-08	0.56724E-09	0.89818E-02	-.38803E-05	0.82327E-02	0.69478E-02	0.25429E-01	0.57799E-02
p E112.23	0.11556E-07	0.38855E-09	0.86804E-02	-.38717E-05	0.79490E-02	0.67107E-02	0.62237E-02	0.43845E-01
n E646.09	0.44556E-01	0.17584E-03	0.62076E-08	-.11364E-10	0.57011E-08	0.65534E-08	0.74068E-08	0.12219E-07
n E557.30	0.17584E-03	0.28641E-01	0.54825E-09	0.53361E-10	0.47326E-09	0.57209E-09	0.63971E-09	0.36881E-09
n E470.99	0.62076E-08	0.54825E-09	0.20368E-01	-.49041E-05	0.13160E-01	0.11216E-01	0.10097E-01	0.90929E-02
n E379.21	-.11364E-10	0.53361E-10	-.49041E-05	0.23115E-01	-.15874E-04	-.11319E-04	-.43156E-05	-.32330E-05
n E314.55	0.57011E-08	0.47326E-09	0.13160E-01	-.15874E-04	0.43792E-01	0.10374E-01	0.92539E-02	0.83340E-02
n E232.77	0.65534E-08	0.57209E-09	0.11216E-01	-.11319E-04	0.10374E-01	0.19387E-01	0.78101E-02	0.70373E-02
n E172.76	0.74068E-08	0.63971E-09	0.10097E-01	-.43156E-05	0.92539E-02	0.78101E-02	0.31990E-01	0.65144E-02
n E112.23	0.12219E-07	0.36881E-09	0.90929E-02	-.32330E-05	0.83340E-02	0.70373E-02	0.65144E-02	0.48578E-01

Table 4.4: Error matrix for discrete fit: the elements are for the parameters representing the $S(E)/4\pi$ for the various energies where S(E) is the S-factor. The two reactions $d(d,p)t$ and $d(d,n)^3$He are labeled by p and n respectively.

	$c_{0,0p}$	$c_{0,1p}$	$c_{0,2p}$	$c_{0,3p}$	$c_{0,4p}$	$c_{0,5p}$
$c_{0,0p}$	0.20004E-02	-.53485E-05	-.36761E-08	0.14823E-11	0.81697E-14	0.28071E-17
$c_{0,1p}$	-.53485E-05	0.88324E-07	-.11170E-09	-.22047E-12	-.36911E-15	-.45971E-18
$c_{0,2p}$	-.36761E-08	-.11170E-09	0.12939E-11	-.12238E-14	-.29094E-17	-.63090E-20
$c_{0,3p}$	0.14823E-11	-.22047E-12	-.12238E-14	0.14836E-16	-.12833E-19	-.36240E-22
$c_{0,4p}$	0.81697E-14	-.36911E-15	-.29094E-17	-.12833E-19	0.14913E-21	-.15646E-24
$c_{0,5p}$	0.28071E-17	-.45971E-18	-.63090E-20	-.36240E-22	-.15646E-24	0.13490E-26
$c_{0,0n}$	0.16677E-02	-.22152E-05	-.88252E-08	-.10683E-10	0.60044E-14	0.84921E-16
$c_{0,1n}$	0.20295E-06	0.34878E-07	0.39186E-10	-.99165E-13	-.61726E-15	-.21046E-17
$c_{0,2n}$	-.13283E-07	0.73808E-10	0.25155E-12	0.24032E-15	-.11468E-17	-.86304E-20
$c_{0,3n}$	-.28226E-10	-.47487E-13	0.40164E-15	0.14968E-17	0.19677E-20	-.65027E-23
$c_{0,4n}$	-.73149E-14	-.67632E-15	-.79711E-18	0.27870E-20	0.18905E-22	0.74057E-25
$c_{0,5n}$	0.19634E-15	-.27695E-17	-.89922E-20	-.39277E-23	0.82231E-25	0.53344E-27
	$c_{0,0n}$	$c_{0,1n}$	$c_{0,2n}$	$c_{0,3n}$	$c_{0,4n}$	$c_{0,5n}$
$c_{0,0p}$	0.16677E-02	0.20295E-06	-.13283E-07	-.28226E-10	-.73149E-14	0.19634E-15
$c_{0,1p}$	-.22152E-05	0.34878E-07	0.73808E-10	-.47487E-13	-.67632E-15	-.27695E-17
$c_{0,2p}$	-.88252E-08	0.39186E-10	0.25155E-12	0.40164E-15	-.79711E-18	-.89922E-20
$c_{0,3p}$	-.10683E-10	-.99165E-13	0.24032E-15	0.14968E-17	0.27870E-20	-.39277E-23
$c_{0,4p}$	0.60044E-14	-.61726E-15	-.11468E-17	0.19677E-20	0.18905E-22	0.82231E-25
$c_{0,5p}$	0.84921E-16	-.21046E-17	-.86304E-20	-.65027E-23	0.74057E-25	0.53344E-27
$c_{0,0n}$	0.34272E-02	-.20322E-04	0.21610E-07	0.67404E-10	0.22157E-13	-.45335E-15
$c_{0,1n}$	-.20322E-04	0.40126E-06	-.10921E-08	-.12239E-11	0.83520E-15	0.10239E-16
$c_{0,2n}$	0.21610E-07	-.10921E-08	0.86900E-11	-.11854E-13	-.18094E-16	0.13668E-20
$c_{0,3n}$	0.67404E-10	-.12239E-11	-.11854E-13	0.11791E-15	-.12712E-18	-.29136E-21
$c_{0,4n}$	0.22157E-13	0.83520E-15	-.18094E-16	-.12712E-18	0.12155E-20	-.19748E-23
$c_{0,5n}$	-.45335E-15	0.10239E-16	0.13668E-20	-.29136E-21	-.19748E-23	0.88599E-26

Table 4.5: Error matrix for continuous fit: The elements are for the parameters representing the polynomial coefficients on $S(E)/4\pi$ expanded in center-of-mass energy. The subscripts p and n indicate the $d(d,p)t$ and $d(d,n)^3$He reactions respectively.

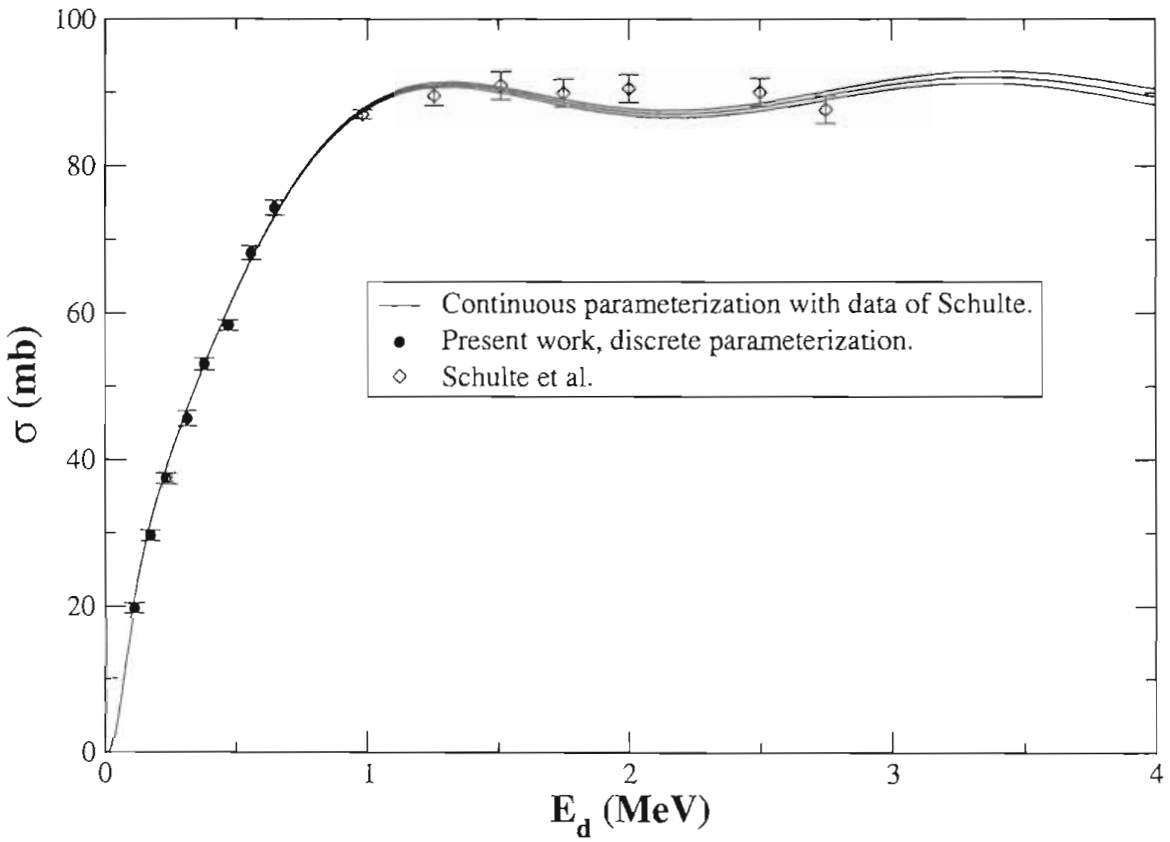

Figure 4.3: Integrated cross-section result for $d(d,p)t$ of fit of continuous parameterization including integrated cross-section data of Schulte *et al.* [Sch72] The Schulte statistical uncertainties were multiplied by 5 in the figure and the fit.

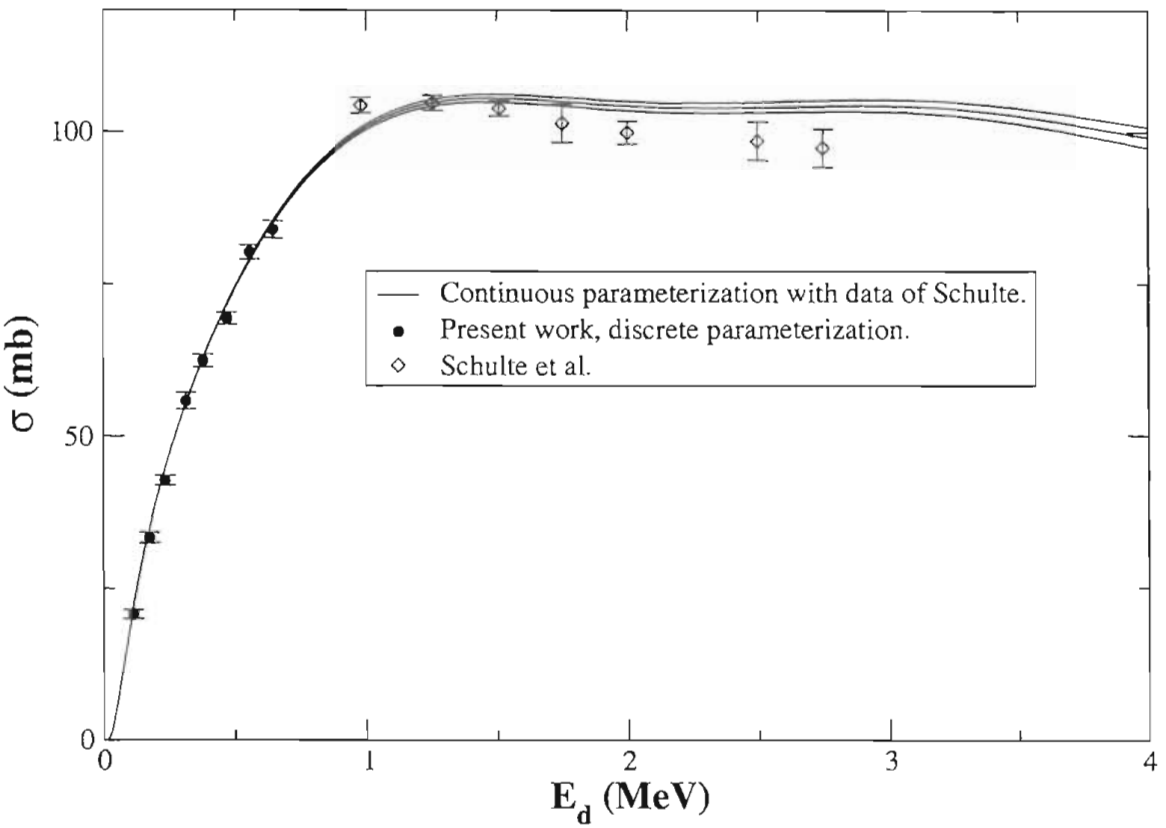

Figure 4.4: Integrated cross-section result for $d(d,n)^3$He of fit of continuous parameterization including integrated cross-section data of Schulte *et al.* [Sch72] The Schulte statistical uncertainties were multiplied by 5 in the figure and the fit.

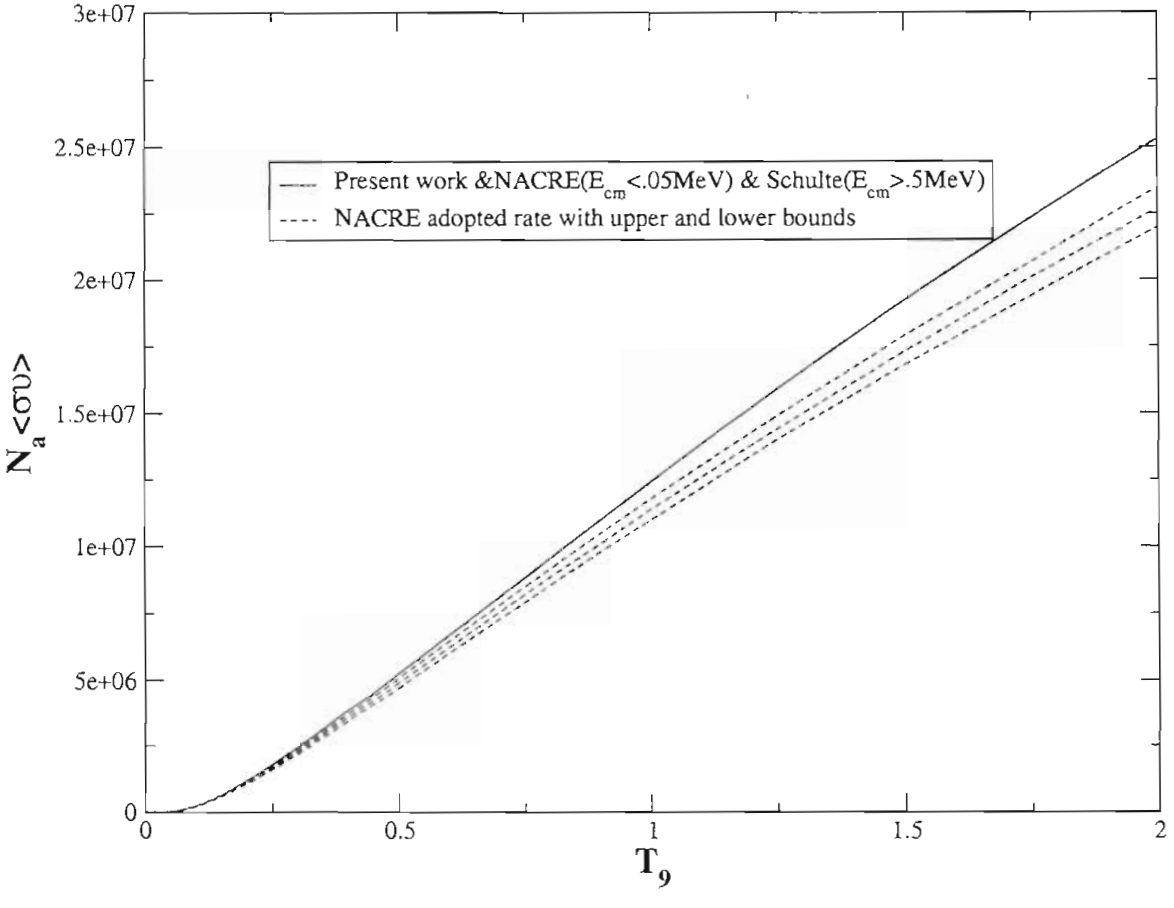

Figure 4.5: Comparison of $d(d,p)t$ reaction rates of present work with NACRE rate compilation: The results of the present work use the low energy cross-section fit of NACRE in the rate integral for $E_{cm} < 0.05\ MeV$. Data of Schulte *et al.* [Sch72] are used to constrain the cross-section fit of the present work at energies above E_{cm} = 0.5 MeV.

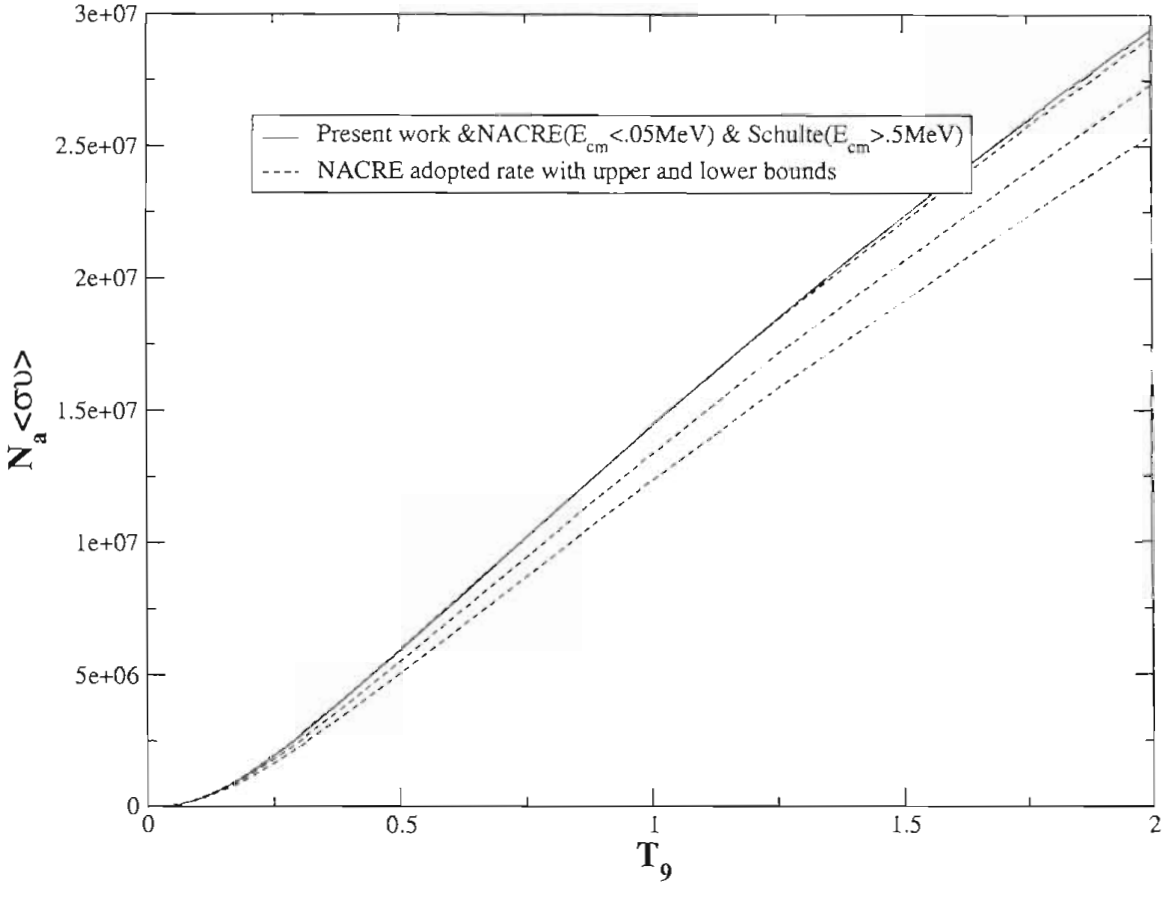

Figure 4.6: Comparison of $d(d,n)^3$He reaction rates of present work with NACRE rate compilation: The results of the present work use the low energy cross-section fit of NACRE in the rate integral for $E_{cm} < 0.05\ MeV$. Data of Schulte *et al.* [Sch72] are used to constrain the cross-section fit of the present work at energies above E_{cm} = 0.5 MeV.

Appendix A

Background Subtraction

Here I derive the expression for the statistical error in subtracting a linear background from a peak as depicted in Figure A.1. This is not complicated but is useful and comes up often. Consider a peak with a gate marking two points on either side of it. The sum of all counts in the gate is determined and will be called the total number of counts T. A background gate is marked around the peak concentric with the first gate. In Figure A.1 the background gate is wider than the peak gate. However, this is not required for this derivation so long as the peaks are concentric and the endpoints of the background gate are indeed located where there is an appropriate background to sample. The background level is sampled at S points centered around each of the endpoints of the background gate. We can consider the mean value of these samples as two single sample points taken at the gate endpoints with values h_1 and h_2. A line was then calculated to go through these two points. This line represents the background. The area under this line and inside of the peak gate is then determined to be the background area B. It is evident then that the peak area N is given by

$$N = T - B \tag{A.1}$$

and since the sample points were symmetric around the peak gate then it also follows directly that B is given simply by

$$B = hW \tag{A.2}$$

where h is the mean background height:

$$h = \frac{h_1 + h_2}{2} \tag{A.3}$$

To determine the error in N we need the error in T which is given by counting statistics and is simply $\sqrt{T}$. We also need the error in B which depends on h and thus the h_i's. The error in h_i, σ_{h_i}, is given by the percent error in the area Sh_i sampled at the i'th endpoint times the value of h_i. The error in h is then derived directly from Equation A.3.

$$\sigma_{h_i} = \frac{\sqrt{h_i S}}{h_i S} h_i = \sqrt{\frac{h_i}{S}} \tag{A.4}$$

$$\sigma_h = \frac{1}{2}\sqrt{\sigma_{h_1}^2 + \sigma_{h_2}^2} = \frac{1}{2}\sqrt{\frac{h_1}{S} + \frac{h_2}{S}} = \sqrt{\frac{h}{2S}} \tag{A.5}$$

Then it follows directly from Equation A.2 that

$$\sigma_B = W\sigma_h = W\sqrt{\frac{h}{2S}} = B\sqrt{\frac{1}{2hS}} \tag{A.6}$$

and from Equation A.1

$$\sigma_N = \sqrt{\sigma_T^2 + \sigma_B^2} = \sqrt{T + B^2\frac{1}{2hS}} \tag{A.7}$$

and thus

$$\boxed{\sigma_N = \sqrt{T + \frac{BW}{2S}}} \tag{A.8}$$

Note the strong dependence on W. W is effectively squared in the second term under the square-root since the total background area itself is just Wh. For this reason peak gates should always be set as tightly as is reasonable when subtracting backgrounds. Equation A.8 is only correct if the background gate is centered around the peak gate which is usually at least close to true. Recall that 2S is the total number of sample points on both sides of the peak. It is usually true that this is on the order of the peak width but often somewhat smaller. For this reason equation A.8 can be approximated by a rule of thumb known to many nuclear physicists,

$$\sigma_N = \sqrt{T + nB} \tag{A.9}$$

where n is usually set to 2 or sometimes 3 or 4 for a more conservative estimate. This estimate is the equation I heard from various people when I went to subtract my very first peak background. I thought it seemed a little arbitrary and wondered if n really could just be whatever I wanted. It only took a couple of minutes and a napkin to work out the exact expression. Indeed though, as anyone familiar with background subtraction knows, this statistical expression does not cover the uncertainty associated with the background shape. Even if the background shape is known, it is not always linear so equation A.8 may be inexact. These issues are reasonable justification for using the approximate expression and for using large values of n.

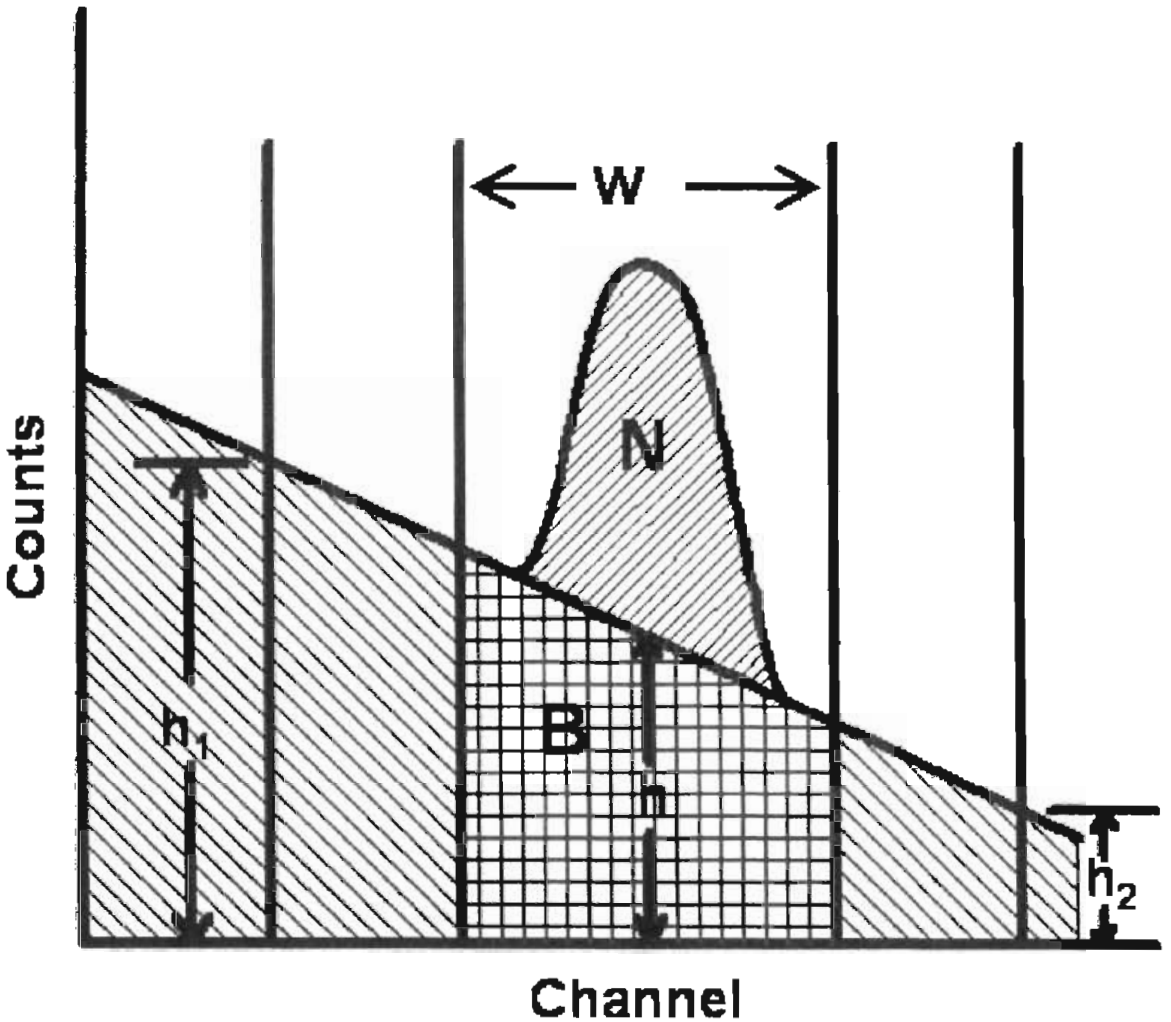

Figure A.1: Subtraction of a linear background from a peak. The background level is sampled around 2 locations set by an outer background gate. The area labeled N is the true peak area. B represents the Background area to be subtracted from the area in the peak gate.

Appendix B

Error Matrix and MINUIT

Obtaining the error matrix elements from MINUIT (at least from the Fortran version) is not as simple of a task as it should be and is not terribly well documented, so I will share my tips on the issue. The parameter indeces that are used in the error matrix are not necessarily the same as the indeces the parameters are initialized with. Any unused parameters, either "fixed" by the user or "constant" from initialization, are removed from the indexing. The next parameter is then put in its place and all numbering from there on is shifted by one. This is not terribly difficult to deal with unless you do not know it is happening. A small code segment to retrieve the error matrix elements is shown in figure B.1. The original parameter values are stored in par(i). The matrix elements with the broken indexing are retrieved into emat(l,m). I remap the parameter indeces i to newpar(i). To access the the matrix element E_{ij} one would then use emat(newpar(i),newpar(j)).

The arrays are indexed to 300 because I have compiled MINUIT to use 300 parameters. The number of parameters in a particular compilation will probably be different. I believe the default number of free parameters is 50 and the number of total parameters is 100. This should only matter for the par and dpar variables in this code segment. The emat matrix can probably be dimensioned as desired so long as it is big enough to hold all the matrix elements desired, but some experimentation may be needed. The code shown here is not intended to demonstrate the basic usage

```
      PROGRAM MAIN
      ...
      ...
      real*8 par(300),dpar(300)
      real*8 emat(300,300)
      integer newpar(300),i,j
      common /cpar/par,dpar
c  Get current status of all parameters.. values placed in par and dpar
c   via the common block.
      call getpars
c  Re-index the free parameters for compatibility with mangled MINUIT
c   error matrix output.
      j=1
      do i=1,300
c This conditional should be sufficient to determine if a parameter
c   is free.
       if (dpar(i).ne.0) then
         newpar(i)=j
         j=j+1
       else
         newpar(i)=0
       endif
      enddo
      call mnemat(emat,300)
      ...
      ...
      end


      SUBROUTINE GETPARS
      real*8 par(300),dpar(300),null1,null2
      integer inull,i
      character*3 cnull
      common /cpar/par,dpar
        do i=1,300
          call mnpout(i,cnull,par(i),dpar(i),null1
     &       ,null2,inull)
        enddo
      end
```

Figure B.1: Fortran segment for retrieving error matrix elements from MINUIT

and initialization of MINUIT in Fortran callable mode. For a complete description of how to do this see the MINUIT manual [Jam94].

REFERENCES

[Ang99] C. Angulo et al., Nucl. Phys. **A656** (1999), **NACRE** web site `http://pntpm.ulb.ac.be/nacre.htm`.

[Ben03] C. L. Bennet et al., Ap. J. Suppl. **148**, 175 (2003).

[Bev92] P. R. Bevington and D. K. Robinson, *Data Reduction and Error Analysis for the Physical Sciences*, 1992.

[Bla93] T. C. Black, B. E. Hendrix, E. R. Crosson, K. A. Fletcher, H. J. Karwowski, and E. J. Ludwig, Nucl. Instr. and Meth. **A 333**, 239 (1993).

[Bro89] R. E. Brown and N. Jarmie, Phys. Rev. C **41**, 1391 (1989).

[Bru98] C. R. Brune, 1998, private communication.

[Bru01] C. R. Brune, W. H. Geist., H. J. Karwowski, E. J. Ludwig, K. D. Veal, and M. H. Wood, Phys. Rev. C **63**, 044013 (2001).

[Bur98a] S. Burles and D. Tytler, Astrophys. J. **499**, 699 (1998).

[Bur98b] S. Burles and D. Tytler, Astrophys. J. **507**, 732 (1998).

[Bur99a] S. Burles, K. M. Nollett, J. W. Truran, and M. S. Turner, Phys. Rev. Lett. **82**, 4176 (1999).

[Bur99b] S. Burles, K. M. Nollett, J. W. Truran1, and M. S. Turner, Phys. Rev. Lett. **82**, 4176 (1999).

[Bur03] S. Burles, 2003, private communication.

[Cle95] T. B. Clegg, H. J. Karwowski, S. K. Lemieux, R. W. Sayer, E. R. Crosson, W. M. Hooke, C. R. Howell, H. W. Lewis, A. W. Lovette, H. J. Pfutzner, K. A. Sweeton, and W. S. Wilburn, Nucl. Instr. Meth. **A 357**, 200 (1995).

[Coc01] A. Coc, E. Vangioni-Flam, and M. Cassé, arXiv:astro-ph/0101286, 2001.

[Cuo03] A. Cuoco, F. Iocco, G. Mangano, G. Miele, O.Pisanti, and P.D.Serpico, arXiv:astro-ph/0307213, 2003.

[Cyb03] R. H. Cyburt, B. D. Fields, and K. A. Olive, Phys. Lett **B567**, 227 (2003).

[Fio98] G. Fiorentini, E. Lisi, S. Sarkar, and F. L. Villante, Phys. Rev. D. **58**, 063506 (1998).

[Fis03] B. M. Fisher, Ph.D. thesis, University of North Carolina at Chapel Hill, 2003, Available from University Microfilms, Ann Arbor, Michigan.

[Gan58] A. S. Ganeev. A. M. Govorov, G. M. Osetinskii, A. N. Rakivenko, I. V. Sizov, and V. S. Siksin, Atomic Energy Suppl. **5**, 21 (1958).

[Gei98] W. H. Geist, Ph.D. thesis, University of North Carolina at Chapel Hill, 1998, Available from University Microfilms, Ann Arbor, Michigan. Document #9902466.

[Gre95] U. Greife, F. Gorris, M. Junker, C. Rolfs, and D. Zahnow, Z. Phys A **351**, 107 (1995).

[Hut83] E. Huttel, W. Arnold, H. Berg, H. Krause, J. Ulbricht, and G. Clausnitzer, Nucl. Phys. **A406**, 435 (1983).

[Iri] Y. Irie, H. Yamamoto, H. Hasuyama, and Y. Wakuta, Genshikaku Kenkyu **17**, 567, Translated by O. Yasuda.

[Jam94] F. James, MINUIT: *Function Minimization and Error Analysis Reference Manual*, 1994, CERN, `wwwinfo.cern.ch/asdoc/minuit/minmain.html`.

[Kap01] M. Kaplinghat and M. Turner, Phys. Rev. Lett. **86**, 385 (2001).

[Kie95] A. Kievsky, M. Viviani, and S. Rosati, Phys. Rev. C **52**, R15 (1995).

[Kie01] A. Kievsky, 2001, private communication.

[Kir03] D. Kirkman, D. Tytler, N. Suzuki, J. M. O'Mera, and D. Lubin, arXiv:astro-ph/0302006, 2003.

[Kra87] A. Krauss, H. W. Becker, H. P. Trautvetter, C. Rolfs, and K. Brand, Nucl. Phys. **A465**, 150 (1987).

[Kra90] L. M. Krauss and P. Romanelli, Ap. J. **358**, 47 (1990).

[Lud97] E. J. Ludwig, T. C. Black, C. R. Brune, W. H. Geist, and H. J. Karwowski, Nucl. Instr. and Meth. **A 388**, 37 (1997).

[Mck01] C. J. Mckinney and H. J. Karwowski, Rev. Sci. Inst. **72**, 3687 (2001).

[Mey76] H. O. Meyer, G. R. Plattner, and I. Sick, Z. Physik A **279**, 41 (1976).

[Nol01] K. M. Nollett and S. Burles, Phys. Rev D. **61**, 123505 (2001).

[Ren97] M. C. M. Rentmeester and J. J. de Swart, 1997, preliminary Nijmegen proton-proton PWA97 (private communiation).

[Sch72] R. L. Schulte, M. Cosack, A. W. Obst, and J. L. Weil, Nucl. Phys. **A192**, 609 (1972).

[Sch98] D. Schramm and M. Turner, Rev. Mod. Phys. **70**, 303 (1998).

[Sil59] E. A. Silverstein, Nucl. Instr. and Meth. **4**, 53 (1959).

[Smi93] M. S. Smith, L. H. Kawano, and R. A. Malaney, Ap. J. Suppl. Ser. **85**, 219 (1993).

[Tay97] J. R. Taylor, *Introduction to Error Analysis: The Study of Uncertainties in Physical Measurements, Second Edition*, 1997.

[Teg00] M. Tegmark, Phys. Rev. Lett. **85** (2000).

[Tyt00] D. Tytler, J. M. O'Meara, N. Suzuki, and D. Lubin, arXiv:astro-ph/0001318, 2000.

[VF00] E. Vangioni-Flam, A. Coc, and M. Cassé, arXiv:astro-ph/0002248, 2000.

[Wal91] T. P. Walker, G. Steigman, D. N. Schramm, K. A. Olive, and H. Kang, Ap. J. **376**, 51 (1991).

[Woo00] M. H. Wood, Ph.D. thesis, University of North Carolina at Chapel Hill, 2000, Available from University Microfilms, Ann Arbor, Michigan. Document #9979498.

[Zie03] J. F. Ziegler, "**SRIM** - THE STOPPING AND RANGE OF IONS IN MATTER", 2003, SRIM web site `http://www.srim.org/`.